Pulsed Laser Deposited Iron Garnet Thin Films for Spintronics

By

Bharat Khurana

B. Tech. and M. Tech. in Metallurgical and Materials Engineering
Indian Institute of Technology Kharagpur (2018)

Submitted to the Department of Materials Science and Engineering
in partial fulfillment of the requirements for the degree of

Doctor of Philosophy in Materials Science and Engineering

at the

Massachusetts Institute of Technology

May 2024

Signature of
author_____
Department of Materials Science and Engineering
April 10th, 2024

Certified
by_____
Caroline A. Ross
Ford Professor of Materials Science and Engineering
Thesis Supervisor

Accepted
by_____
Robert J. Macfarlane
Associate Professor Materials Science and Engineering
Chair, Departmental Committee on Graduate Studies

This thesis is dedicated to the five most important people in my life:

Mr. Arvind Kejriwal, Prof. Caroline Ross, Mrs. Pushpa Gaind (my grandmother), Mrs. Rampyari Khurana (my grandmother), for inspiring me to be a better version of myself every day

& Mrs. Meenakshi Khurana (my mother), the person behind all my small and big achievements.

Pulsed Laser Deposited Iron Garnet Thin Films for Spintronics

by
Bharat Khurana
Submitted to the Department of Materials Science and Engineering
on April 3rd, 2024, in Partial Fulfillment of the
Requirements for the Degree of Doctor of Philosophy
in Materials Science and Engineering

Abstract

This thesis aims to develop materials for spintronic memories and demonstrate growth of iron garnet superlattices with layering at a sub unit cell scale. Iron garnet films are suitable for next generation spintronic memories because of their low Gilbert damping and their growth with perpendicular magnetic anisotropy (PMA) which promote fast domain wall dynamics. Additionally, selection of rare earth ion and substitution of cations in various sublattices of iron garnets enables tuning of their saturation magnetization, magnetocrystalline anisotropy, Gilbert damping and magnetostriction. Superlattices of garnets provide an opportunity to explore interfacial phenomena.

We first study spin transport in platinum/scandium-substituted terbium iron garnet heterostructures. Epitaxial scandium-substituted terbium iron garnet (TbScIG) thin films were deposited on gadolinium gallium garnet [GGG, (111) orientation] substrates using pulsed laser deposition (PLD). Sc, a nonmagnetic cation, occupies up to 40% of the octahedral Fe sites. Anomalous Hall effect-like spin Hall magnetoresistance measurements were performed to determine the effect of scandium content on spin mixing conductance of the TbScIG|Pt interface. The spin mixing conductance increased significantly with an increase in Sc content. We then study bilayer films of bismuth-substituted yttrium iron garnet (BiYIG)/ thulium iron garnet (TmIG) grown on garnet substrates that combine the non-zero interfacial Dzyaloshinskii–Moriya interaction (DMI) of TmIG with moderate damping between that of BiYIG and TmIG, making them useful for the development of high speed spin orbit torque driven magnetic devices. Lastly, we describe superlattices made from rare earth (RE = Tm, Tb, Lu) and bismuth iron garnets (IGs) grown by pulsed laser deposition. Superlattices of TmIG/TbIG show a composition modulation for layers as thin as 0.45 nm, less than one unit cell, and exhibit perpendicular magnetic anisotropy that is qualitatively different from the in-plane anisotropy of the solid solution (Tm,Tb)IG. BiIG/LuIG

superlattices exhibit magnetic damping characteristic of the end members rather than the solid solution. Garnet superlattices may provide a playground for exploring interface physics within a vast parameter space of cation coordination and substitution.

Thesis Supervisor: Caroline A. Ross
Title: Ford Professor of Materials Science and Engineering

Acknowledgements

The 5.5 years I spent at MIT was one of the most valuable experiences of my life. During my graduate studies at MIT, I got an opportunity to work with some of the most talented people in the world. The research presented in this work is the outcome of the efforts of many people who were either involved in my research or my journey at MIT.

Firstly, I would thank my advisor Professor Caroline A. Ross whose support enabled all the work presented in this thesis. She very kindly took me in her group, introduced me to magnetism and spintronics and taught me most of what I know about experimental research. She helped me understand the process of formulating and solving a scientific problem. I am particularly thankful to her for her patience and support during periods of time when I was not able to be fruitful due to various reasons. I cannot imagine being able to complete my thesis without her guidance and support.

I am also deeply grateful to my thesis committee members Professor Geoffrey Beach and Professor James LeBeau for their feedback and collaboration that enabled me to understand all the details of the research problems I was trying to solve. I must also sincerely thank Professor Luqiao Liu for allowing me to work in his labs and collaborate with his students.

I am grateful to my friend from undergrad Jagannadh Sripada for visiting me in Cambridge and accompanying me to cool places around Boston. I would like to thank my best friends at MIT: Parth Khandelwal, Michael Forsuelo and Rohit Sanatani for making my time at MIT so enjoyable. I will miss conversations about Krishna consciousness that I used to have with Parth and I am especially grateful to him for the spiritual wisdom and food that he used to bring for me. I wish I never had to stop my weekly visits to Indian restaurants with Michael (India Pavilion/Desi Dhaba). I am grateful to Rohit for inviting me for conversations, food and walks around MIT. I will also miss walks around Cambridge with Debojyoti Panda from Harvard. All of you are so amazing!

Several current and former members of Prof. Ross's group were helpful during my period at MIT. I sincerely thank Tomas Grossmark, Takian Fakhrul, Kensuke Hayashi, Tingyu Su, Yabin Fan, Jackson Bauer, Katharina Lasinger and Allison Kaczmarek for training me on several equipment, helping me understand spintronics and collaborating with me during my projects at MIT. I also thank Byung Hun Lee and Siying Huang from Prof. Beach's group for collaborating with me at MIT. I thank several current and

former members of Prof. Liu's group for collaborating with me on my projects: Pengxiang Zhang, Taqiyyah Safi, Chung-Tao Chou and Justin Hou. I also thank scientists from NIST for helping with my projects: Hans Nembach, Justin Shaw and Grant Riley. I am also grateful to Charles Settens, Jordan Cox and Libby Shaw from MRL at MIT for helping me with my experiments. I am grateful to David Bono for teaching me how to repair several pieces of equipment several times and Alan Schwartzman for helping me with atomic force microscopy.

I thank India Heritage Foundation (IHF) and MIT Origins for teaching me about Krishna consciousness, inviting me to numerous spiritual, music and food festivals and giving me their company. I am especially grateful to Sadananda Dasa, Panduranga Gopal Dasa, Hari Gopal Dasa and Badri Narayan Dasa from IHF. I thank ISKCON Boston and Vedic Vision Forum (VVF) at MIT for giving me their company and sharing teachings of Shri Prabhupada with me. I thank MIT GSU for being a strong voice of international students and raising issues related to oppressed/underrepresented communities in the system.

I am grateful for the contributions of my flat mate Josh McCarthy, whose multifaceted talents and assistance have enhanced my academic journey at MIT. His culinary expertise has provided sustenance during countless late-night work sessions, while his proficiency in playing guitar has offered moments of relaxation. Moreover, his attention to detail has proven invaluable in refining the formatting, references, and figures of this thesis. His commitment to environmental stewardship, exemplified through his dedication to recycling and passion for animal welfare, serves as a poignant reminder of the importance of sustainability in scientific pursuits. Additionally, his willingness to assist in preparations for my upcoming PhD defense, including plans to prepare food for attendees, highlights his selflessness and generosity of spirit.

Finally, I thank my parents Mrs. Meenakshi Khurana and Mr. Satish Khurana and my professors from undergrad Prof. Gour Gopal Roy, Prof. Sudipto Ghosh and Prof. Sumantra Mandal for encouraging me to apply to PhD program at MIT and helping me with my applications.

This work would not have been possible without the support of SMART, an nCORE Center of the Semiconductor Research Corporation and NIST, by NSF DMR 1808190 and NSF DMR 2028199 and by DARPA DSO TEE program. Shared experimental facilities of CMSE, an NSF MRSEC award DMR 1419807 were used.

Table of Contents

List of figures

FIG. 4.2 Tb 4d, Sc 2p and Fe 2p XPS spectra of representative TbScIG thin films with varying Sc content. Oxidation states of Tb are marked in Tb 4d spectra.

FIG. 4.3 Room temperature out-of-plane VSM hysteresis loops of representative GGG|TbScIG thin films with varying Sc content.

FIG. 4.4 (a) and (b) AHE-like SMR hysteresis loops for TbScIG(60 nm)|Pt(4 nm) heterostructures. (c) Optical micrograph of a representative Hall cross used for measurement. (d) Lower bound of imaginary component of spin mixing conductance versus number of Sc^{3+} ions per formula unit.

FIG. 4.5 Magnetic moment versus temperature for GGG|TbScIG thin films with varying Sc content. A typical error bar is attached.

FIG. 4.6 (a) Magnetic moment per formula unit versus temperature for TbScIG obtained from molecular field coefficient (MFC) model (b) Compensation temperature versus number of Fe^{2+} and Tb^{4+} ions per formula unit in MFC model.

FIG 5.1 a) HRXRD $\omega-2\Theta$ scans around the BiYIG (444) and GSGG, NGG, GYSGG, SGGG, and YSGG (444) peaks. b) Cubic unit cell of BiYIG showing octahedrally, tetrahedrally, and dodecahedrally coordinated cation sites. The cation sites are surrounded by O^{2-} (indicated by black spheres) at the vertices of the polyhedra. c) Schematic of a strained BiYIG cubic unit cell on GSGG with the corner angle β marked. d,e) HRXRD reciprocal-space map of 28 nm BiYIG/GSGG (d) and 70 nm BiYIG/GSGG (e). f) AFM scan on 7 nm thick BiYIG film on GSGG.

FIG 5.2: Hysteresis loops with field applied a) out-of-plane (OP) and b) in-plane (IP) for 25 nm BiYIG on SGGG, NGG, and GSGG. c) IP and OP loops for 70 nm BiYIG on GSGG. d) OP loops for 38 and 28 nm BiYIG on GSGG. e,f) IP and OP loops for 22 nm BiYIG on YSGG and GYSGG.

FIG 5.3: MOKE images showing equilibrium domain structure after a.c. demagnetization of a) 25 nm BiYIG/GSGG, b) 28 nm BiYIG/GSGG, c) 33 nm BiYIG/GSGG, d) 27 nm BiYIG/NGG, and e) 25 nm BiYIG/NGG.

FIG 5.4: MOKE images showing domain structure during reversal of a) 70 nm BiYIG/GSGG, b) 25 nm BiYIG/NGG, and c) 28 nm BiYIG/GSGG. The films were saturated at +60 mT for (a) and −60 mT for (b,c). The red scale bar represents 100 μm.

FIG 5.5: Representative FMR spectra taken at 10 GHz showing a) the imaginary and b) the real part of S_{21} for a 70 nm BiYIG/GSGG. c) Representative fit of the resonant field, H_{res}, versus frequency for 70 nm BiYIG/GSGG. FMR linewidth as a function of frequency for d) 70 nm BiYIG/GSGG, e) 25 nm BiYIG/SGGG, and f) 23 nm BiYIG/NGG.

FIG 5.6. a) Anomalous Hall effect (AHE)-like spin Hall magnetoresistance (SMR) hysteresis loops for NGG(111)|BiYIG(4.3 nm)/Pt(4 nm) heterostructure. b) Optical micrograph of Hall cross used for measurement.

FIG 6.1 (a-c): High-resolution x-ray diffraction (HRXRD) scans of BiYIG, BiYTmIG and BiYIG|TmIG thin films deposited on GSGG and NGG substrates. (d-f): x-ray reflectivity (XRR) scans of BiYIG, BiYTmIG and BiYIG|TmIG thin films deposited on GSGG substrate. A BiYIG:TmIG shot ratio of 25:5 was used for making the 2.5 nm thick BiYTmIG film and 25:2 was used for the 6.7 nm and 8.4 nm thick BiYTmIG films. Inset of (f) shows topographic image from an atomic force microscopy (AFM) scan on BiYIG (3.5 nm)/TmIG (3.1 nm)/GSGG film.

FIG 6.2 Room-temperature out-of-plane vibrating sample magnetometry hysteresis loops of (a) BiYIG (4 nm)|TmIG (3.5 nm) and (b) BiYTmIG (6.7 nm) thin films deposited on GSGG and NGG substrates. A BiYIG:TmIG shot ratio of 25:2 was used for BiYTmIG films.

FIG 6.3 (a) A representative FMR spectrum taken at 16.5 GHz showing the real part of S_{21} for BiYIG (15.5 nm)/TmIG (5.6 nm)/NGG. Fits of linewidth, ΔH, as a function of frequency for (b) BiYIG (70 nm)/GSGG, (c) BiYIG (15.5 nm)/TmIG (5.6 nm)/NGG (d) BiYIG (18 nm)/TmIG (2 nm)/GSGG (e) BiYIG (18 nm)/TmIG (2 nm)/NGG (f) BiYTmIG (8.4 nm)/NGG with BiYIG:TmIG shot ratio of 25:2.

FIG 6.4 BLS frequency change Δf versus wavenumber k for (a) BiYIG (4.3 nm)/GSGG (b) BiYIG (4.3 nm)/NGG, Pt (1 nm)/ BiYIG (4.3 nm)/NGG, Pt (2 nm)/ BiYIG (4.3 nm)/NGG (c) BiYIG (4 nm)/TmIG (3.3 nm)/GSGG (d) BiYIG (4.4 nm)/TmIG (1.9 nm)/NGG, Pt (1 nm)/BiYIG (4.4 nm)/TmIG (1.9 nm)/NGG, Pt (2 nm)/BiYIG (4.4 nm)/TmIG (1.9 nm)/NGG.

FIG 6.5 Domain structure of Pt(4 nm) /BiYIG(4 nm)/TmIG(3.5 nm)/GSGG for various values of in-plane field and out-of-plane field for a 100 μm × 100 μm area observed using MOKE microscope.

FIG. 7.1 Superlattice garnet films. (a) HAADF image for a cross-section of a 16 layered (TbIG/TmIG)/(111)GGG superlattice with overall thickness of 44 nm along a $[11\bar{2}0]$ zone axis. (b) TEM EDS map for the sample in (a). (c) Projected 2D image for APT data for a (TbIG/TmIG)/(111)GGG multilayered film with different layer thicknesses of TbIG and TmIG. In the inset image, each dot represents the position of the ion detected by mass spectrometry. (d,e) Elemental maps of a superlattice of EuIG-TmIG grown on a (110) substrate imaged along the $[1\bar{1}1]$ in-plane zone axis. Fe is shown in green in (d), Eu in magneta and Tm in purple. (f) Crystal structure of REIG along the [111] zone axis showing the Fe (green) and RE (red) sites, matching the arrangement seen in (d,e).

FIG. 7.2 X-ray diffraction of garnet films. (a) HRXRD scans of TmIG, TbIG and TbTmIG films deposited on GGG substrates with (111) orientation (vertically offset for clarity with film and substrate peaks labeled F and S, respectively). (b) HRXRD scans of bilayered, 4 layered, 8 layered, 16 layered and 56 layered films of (TbIG/TmIG)/(111)GGG (vertically offset for clarity). (c) Simulation of XRD scans for bilayered, 4 layered, 8 layered and 16 layered films of (TbIG/TmIG)/(111)GGG with total thickness of 44 nm.

FIG. 7.3 (a) VSM hysteresis loops of TmIG, TbIG and TbTmIG films deposited on GGG substrates with (111) orientation. (b) VSM hysteresis loops of bilayered, 8 layered and 56 layered films (TbIG/TmIG)/(111)GGG with overall thickness of 44 nm or 25 nm. (c) VSM hysteresis loops of 20 layered (TbIG/TmIG) deposited on GGG substrate with (100) orientation and 34 layered (TbIG/TmIG) deposited on GSGG substrate with (111) orientation with thicknesses of 24 nm and 41 nm respectively. (d) In-plane SMR loops for 4 layered, 8 layered and 16 layered (TbIG/TmIG)/(111)GGG with and overall thicknesses of 18 nm, 22 nm and 15 nm respectively deposited on GGG substrates with (111) orientation.

FIG. 7.4 (a) HRXRD scans of LuIG, BiIG, BiLuIG and BiIG/LuIG 12 layered films with thicknesses of 35 nm, 39 nm, 21 nm and 35 nm respectively deposited on GGG substrates with (111) orientation (vertically offset for clarity, with film and substrate peaks labeled F and S, respectively). (b) In-plane VSM hysteresis loops for the the films in (a). (c) Lande g-factor, FMR linewidth at 8 GHz frequency of ac magnetic field and net anisotropy of the films in (a).

FIG. S1. HAADF images for a cross-section of a 16 layered film of (TbIG/TmIG)/(111)GGG with total thickness of 44 nm at different magnifications. In c) the interface is indicated with a white arrow.

FIG. S2. Transmission electron microscopy (TEM) images and atom probe tomography (APT) images showing development of roughness in a TbIG/TmIG multilayer grown at 150 mTorr. (a) HAADF image for a cross-section of a 16 layered film of (TbIG/TmIG)/(111)GGG with total thickness of 44 nm. (b) Corresponding EDS map. The layers are still present in the upper region of the film, but exhibit waviness when the thickness exceeds ~25 nm.

(c) Projected 2D image for APT data for a (TbIG/TmIG)/(111)GGG with different layer thicknesses. Each dot represents the position of an ion detected by mass spectrometry. The shaded region on the right represents the cylindrical volume of the data used to determine the composition profiles in the main text, Figure 1(c).

FIG. S3. Composition measurements. HAADF image and EDS maps for a cross-section of a 16 layered film of (TbIG/TmIG)/(111)GGG with total thickness of 44 nm.

FIG. S4. Atomic force microscopy (AFM) images of TmIG/TbIG multilayers deposited on (111) GGG substrates. AFM scans for (a) 4 layered film with overall thickness of 44 nm and RMS surface roughness of 1.5 nm and (b) 16 layered film with overall thickness of 15 nm and RMS surface roughness of 0.2 nm. (a) and (b) were deposited at oxygen pressure of 150 mTorr. (c) 10 layered film with overall thickness of 33 nm and RMS surface roughness of 0.1 nm deposited at oxygen pressure of 50 mTorr. Note the different height scales for the three samples.

FIG. S5. Atom probe tomography. Left: The APT sample prepared by focused ion beam from a multilayered iron garnet film deposited on a GGG substrate with (111) orientation, which included EuIG, TbIG and TmIG layers of various thickness. Center: composition map (rare-earth ion is specified by color). Development of roughness can be observed with increasing film thickness.

FIG. S6. Symmetric HRXRD scans around the substrate (444) peaks. Substrate peaks are indicated by S and film peaks are indicated by F. All samples were deposited at oxygen pressure of 150 mTorr. (a) GGG|TbIG (44 nm) (b) GGG|TmIG (44 nm) (c) GGG|Bilayer TbIG/TmIG, thickness 44 nm (d) GGG|4 layered TbIG/TmIG film with overall thickness 44 nm (e) GGG|8 layered TbIG/TmIG film with overall thickness 44 nm (f) GGG|16 layered TbIG/TmIG film with overall thickness 44 nm (g) GGG|20 layered TbIG/TmIG film with overall thickness 38 nm (h) GGG|26 layered TbIG/TmIG film with overall thickness 39 nm (i) GGG|56 layered TbIG/TmIG film with overall thickness 25 nm (j) GGG|Solid solution TbTmIG film (44 nm) (k) GGG|8 layered TbIG/TmIG film with overall thickness 22 nm (l) GSGG|34 layered TbIG/TmIG film with overall thickness 41 nm (m) GGG|BiIG (39 nm) (n) GGG|LuIG (35 nm) (o) GGG|12 layered BiIG/LuIG film with overall thickness 35 nm (p) GGG| Solid solution BiLuIG (21 nm).

FIG. S7. Symmetric HRXRD scans around substrate (444) peaks for GGG|10 layered TbIG/TmIG film with thickness 23 nm deposited at oxygen pressure of 150 mTorr, GGG|10 layered TbIG/TmIG film with thickness 20 nm deposited at oxygen pressure of 100 mTorr, GGG|10 layered TbIG/TmIG film with thickness 33 nm deposited at oxygen pressure of 50 mTorr and GGG|40 layered TbIG/TmIG film with thickness 20 nm deposited at oxygen pressure of 50 mTorr.

FIG. S8. Out of plane hysteresis loops of TmIG/TbIG multilayers on (111) GGG. (a) 8 layered film of (TbIG/TmIG)/(111)GGG with overall thickness 22 nm (b) 4 layered film with overall thickness 44 nm (c) 16 layered film with overall thickness 44 nm.

FIG. S9. Ferromagnetic resonance (FMR) data. (Frequency)2 versus resonance field for (a) BiIG (39 nm) (b) LuIG (35 nm) (c) Solid solution BiLuIG (21 nm) (d) 12 layered (BiIG/LuIG)/(111)GGG (35 nm). All these films were deposited on GGG substrates with (111) orientation. (e) Real part of complex transmission parameter for the film in (d) at frequency of 14.2 GHz vs. in-plane field.

List of tables

Chapter 1: Introduction

1.1 Motivation

1.1.1 Increase in demand for computational power

The demand for computation has been increasing rapidly over the past few years with progress in fields of communication, internet of things and artificial intelligence technologies along with increase in internet access [1]. Increase in computational power has contributed significantly to progress in areas of science and medicine as high throughput models can explore a variety of materials and treatments in much less time. However, the increased demand for computation has also led to an increase in energy consumption. Most of the internet traffic passes through some data centers and the energy demand of these data centers accounted for 2 % of the total energy demand of USA in 2014 and 1 % of the total energy demand globally in 2019 [1,2]. Additionally, there is energy demand for billions of local devices like personal computers or workstations. Thus, the increased demand for computational power has contributed to increase in demand for energy and has a significant carbon footprint associated with it. Most efforts to address this challenge have focused on making improvements in existing technologies. Improvement in server efficiency through reduction in standby power consumption and architectural innovations has helped reduce the power consumption for a task by a factor of 4 since 2010 [3]. This has helped to mitigate the problem of energy demand associated with increased computing power demand to some extent. However, the conventional complementary metal oxide semiconductor technologies used for integrated circuits are closer to the limit than ever before.

1.1.2 New materials and technologies for more energy efficient computing

Development of new materials and technologies is crucial to address the challenge of increase in energy demand associated with increase in computation. Dynamic random-access memory (DRAM) is used as a short term storage for central processing units (CPUs) in modern computers. DRAM is used to store data that is either too large for processor cache or may not be immediately needed. Bits that are used to store

information in DRAM are composed of a transistor and a capacitor. However, DRAM's information storage is volatile as voltage constantly needs to be applied to the capacitor – in absence of voltage, the signal decays resulting in loss of information. Thus, DRAM is constantly using energy even when it is just storing information and is not being actively used. Hard disk drive (HDD) on the other hand is used for long term storage. Tiny magnetic bits made up of grains of a magnetic material are used to store information in HDD – they can be magnetized in or out of plane and the direction of magnetization can be used to store information in the form of zeroes and ones. Information storage in HDD is non-volatile as the direction of magnetization of bits remains unchanged even after the agent that was used to manipulate them (like write current) has been removed. However, information storage in HDD is much slower than CPU making it important to use DRAM as intermediate. Magnetic random-access memory combines best of both these technologies. Bits that are used to store information in MRAM are made up of 1 transistor + 1 magnetic tunnel junction (MTJ) [4]. Information stored in an MRAM bit is retained even after the write current is removed making it more energy efficient than DRAM.

MRAM is a part of the large and exciting discipline of spintronics. Spintronics relies on intrinsic spin of electron. The ability to use and manipulate spin potentially allows conveying twice the amount of information compared to unpolarized electric current [5]. It also allows higher processing speed and energy efficiency for working of integrated circuits. Apart from MRAM, work has also been done on spin based information storage and logic devices [6,7].

1.1.3 Rare earth iron garnets as material for spintronic devices

Most of the work on spintronics has focused on metallic magnets. However, recent developments in the field have allowed development of spintronics devices based on insulating magnetic oxides [8]. Information can be transmitted through an insulating magnetic oxide by making use of spin waves without any electronic current flowing through them. This helps to get rid of energy dissipation in form of ohmic

losses and energy required for cooling. Insulating magnetic oxides also allow fast magnetization dynamics because of their low Gilbert damping compared to metallic magnets.

Rare earth iron garnets (REIGs) are an important class of insulating magnetic oxides for spintronics applications. They consist of cations in three different sublattices – dodecahedral sublattice occupied by rare earth ions and octahedral and tetrahedral sublattices occupied by iron ions. Selection of rare earth ion on dodecahedral sublattice and nonmagnetic cation substitution on octahedral/tetrahedral sublattices can tune a variety of properties including saturation magnetization, compensation temperature, magnetostriction, Gilbert damping and Dzyaloshinskii-Moriya interaction (DMI). Thus, the composition of REIGs can be optimized to meet the requirements of a specific application. REIGs can be grown in form of thin films using various types of physical vapor deposition techniques. Metal overlayers can be deposited on REIG thin films using sputtering to form heterostructures [eg. heavy metal (HM) overlayer deposition on REIG thin films]. These heterostructures can be patterned to form devices like Hall bars or domain wall motion based devices. Tunability, stability and compatibility with other materials make REIGs promising material for spintronics research and applications.

1.2 Organization of Thesis

In this thesis we first study properties of substituted REIG thin films with nonmagnetic cation substitution on octahedral sublattice. These films showed perpendicular magnetic anisotropy (PMA). Spin transport properties of substituted REIG|HM interface has been investigated and the role of iron sublattice in determining spin mixing conductance of REIG|HM interface is studied. We then study bilayer films of iron garnets that achieve moderate damping and significant DMI along with PMA which make them promising material for high-speed spin orbit torque driven devices. Lastly, we study superlattices of iron garnets deposited by pulsed laser deposition and compare their properties with those of end members and codeposited films. We show evidence for layering at a sub unit cell scale for iron garnets. As iron garnets allow tuning in properties by choice of rare earth ion and nonmagnetic substitution on

octahedral/tetrahedral sublattices, iron garnet superlattices with rich parameter space offer opportunity to explore physics related to interfaces. We finally present a summary of our findings and some directions for possible future research.

Chapter 2: Background on magnetism, properties of iron garnets, advancements in spintronics and oxide superlattices.

Chapter 3: Techniques used for deposition of iron garnet thin films and platinum overlayers and techniques used for structural, magnetic and spintronic characterization of these films.

Chapter 4: Magnetism and spin transport in platinum/scandium substituted terbium iron garnet (TbScIG) heterostructures has been reported. Iron sublattice has been found to play the dominant role in determining spin mixing conductance across REIG|HM interface.

Chapter 5: Anisotropy and Gilbert damping of bismuth substituted yttrium iron garnet (BiYIG) epitaxial thin films has been reported for various garnet substrates. Domain structure of BiYIG films have been observed under equilibrium conditions and during magnetization reversal. Efficient spin transport across BiYIG|Pt interface has also been reported.

Chapter 6: Damping and interfacial DMI in thulium iron garnet (TmIG)/ BiYIG bilayers have been reported. Bilayers deposited on neodymium gallium garnet (NGG) were shown to have PMA, moderate damping and significant DMI (sufficient to stabilize Neel domain walls). These properties make these bilayers a promising material for high-speed spin orbit torque driven devices.

Chapter 7: Pulsed laser deposited multilayered epitaxial thin films of iron garnets have been reported. Properties of multilayers were found to be similar to those of end members and not codeposited films with same overall composition. Evidence for layering has been shown at a sub unit cell scale for iron garnets.

Chapter 8: Important results presented in this thesis have been summarized along with some possible directions for future research.

Chapter 2: Background

2.1 Magnetism

2.1.1 General

Magnetism has been known for a very long period of time. However, to develop a thorough understanding of the origin of magnetism one needs to look at quantum mechanics. An accurate understanding of the origin of magnetism was developed in 20th century by making use of quantum mechanics [9]. Only 4 elements are magnetic at room temperature – iron, cobalt, nickel and gadolinium and ruthenium has been found to be ferromagnetic at room temperature under some conditions [10].

We begin by looking at magnetic moments in isolated atoms. Lande g-factor is related to the amounts of spin and orbital angular momentum present in an atom and is given by:

$$g = 1 + \frac{J(J+1) + S(S+1) - L(L+1)}{2\,J\,(J+1)} \qquad (2.1)$$

Here S is the spin angular momentum, L is the orbital angular momentum and J is the total angular momentum present in an atom [11]. Spin angular momentum only depends on the intrinsic spin of an electron which can take on values of ± ½ and S is the sum of spin angular momentum of all electrons in an atom. Orbital angular momentum depends on the orbital that an electron occupies. For example, for 3d orbitals in transition metals there are 5 possible values of orbital angular momentum: -2, -1, 0, 1, 2. For rare earth elements there are 7 4f orbitals and possible values of orbital angular momentum are -3, -2, -1, 0, 1, 2, 3. L is the sum of orbital angular momentum of all electrons in an atom. Electrons in an atom are filled according to Pauli's exclusion principle and Hund's rule [9].

1. A degenerate set of orbitals are filled such that the total spin is maximized. This causes electrons to occupy separate orbitals and minimizes Coulombic repulsion between electrons.
2. Orbitals are filled such that the total orbital angular momentum is maximized. This causes electrons to occupy orbitals which orbit nucleus in the same sense. This also minimizes Coulombic repulsion.

3. For a set of degenerate orbitals that are less than half-filled J is given by absolute value of difference between L and S and for more than half-filled J is given by absolute value of sum of L and S.

$$J = |L - S|, for\ less\ than\ half - filled \qquad (2.2)$$

$$J = |L + S|, for\ more\ than\ half - filled \qquad (2.3)$$

For a set of degenerate orbitals that are exactly half-filled, L = 0 and both the above equations give the same result. The above equations are valid for isolated atoms but may not be applicable for solids. For example, for transition metals for which 3d orbitals are being filled, energy for electrons being filled in 3d subshell is close to fermi level. As a result, the orbital angular momentum is quenched because of the crystal field in the solid. For rare earth elements the 4f electrons are deep inside the atom. Thus, the effect of crystal field is relatively less important, and the above equations are a good approximation [12].

Slater-Pauling curve shows variation of saturation magnetization of transition metals as their 3d orbital is getting filled [9]. Rigid band model has been used to give an explanation for the Slater-Pauling curve. According to the rigid band model there is splitting in the band structure of 3d orbital for minimization of free energy. This results in one polarization being fuller than the other polarization and a net magnetic moment. This description may not be an accurate representation of complex band structure of transition metals but correctly explains the trends observed in Slater-Pauling curve.

We now look at interaction between a pair of spins (eg. spins of a pair of electrons). Heisenberg first developed the formalism to explain the origin of ferromagnetism which came to be known as the Heisenberg Hamiltonian equation given by:

$$\hat{\mathrm{H}} = -\sum_{i\,j} J_{ij}\, S_i\, S_j \qquad (2.4)$$

Here J_{ij} is the exchange constant between i^{th} spin S_i and j^{th} spin S_j [12,13]. According to Pauli exclusion principle no two electrons can have the same set of all four quantum numbers. Thus, for the electron wave

function either the spatial part of wavefunction has to be symmetric and the spin part of wavefunction antisymmetric or vice versa [14]. J_{ij} is defined as the difference in energy between wavefunction with symmetric spatial part of wavefunction and antisymmetric singlet spin state and wavefunction with antisymmetric spatial part of wavefunction and symmetric triplet spin state. $J_{ij} > 0$ favors parallel alignment of spins and $J_{ij} < 0$ favors antiparallel alignment of spins. The type of exchange may differ from material to material but the simple equation mentioned above can be used to explain the origins of magnetism.

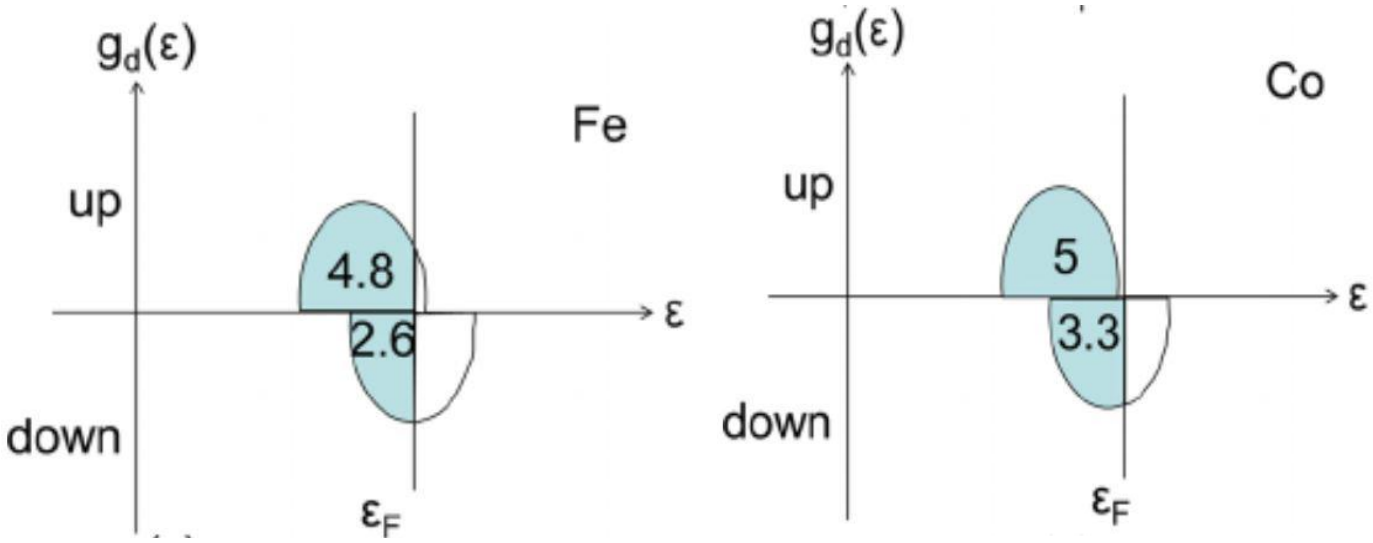

FIG. 2.1 Rigid band model for Fe and Co showing density of states as a function of energy for up and down spins [15].

In rare earth elements, the 4f electrons that are responsible for magnetism are deep in the atom while the 6s and 5p valence shell electrons are conduction electrons. Ruderman–Kittel–Kasuya–Yosida (RKKY) interactions explain how the 4f electrons polarize the conduction electrons and the sign and magnitude of polarization oscillates as a function of distance from nucleus of atom [16–18]. RKKY interactions are relatively weak but the dominant exchange interaction in rare earth elements.

To explain the behavior of magnetic oxides (which are the subject of most of this thesis) we need one more type of exchange interaction. Superexchange interactions are symmetric exchange interactions

between transition metal ions mediated by intervening oxygen anions. Consider bonds formed between $3d_{x^2-y^2}$ orbital of a transition metal and p orbital of oxygen [9]. Due to Pauli's exclusion principle two electrons in p orbital of oxygen atom should have opposite spins. Also, due to Hund's rule which requires electrons occupying degenerate orbitals on a given transition metal ion to have spin orientation that maximizes net spin for the ion and due to Pauli's exclusion principle which requires a pair of electrons forming bond between oxygen and transition metal to have opposite spins, there is antiferromagnetic coupling between adjacent transition metal ions as shown in FIG. 2. In a magnetic oxide with many different bond angles, types of ions and coordination the magnetic structure is determined by Goodenough – Kanamori rules [19].

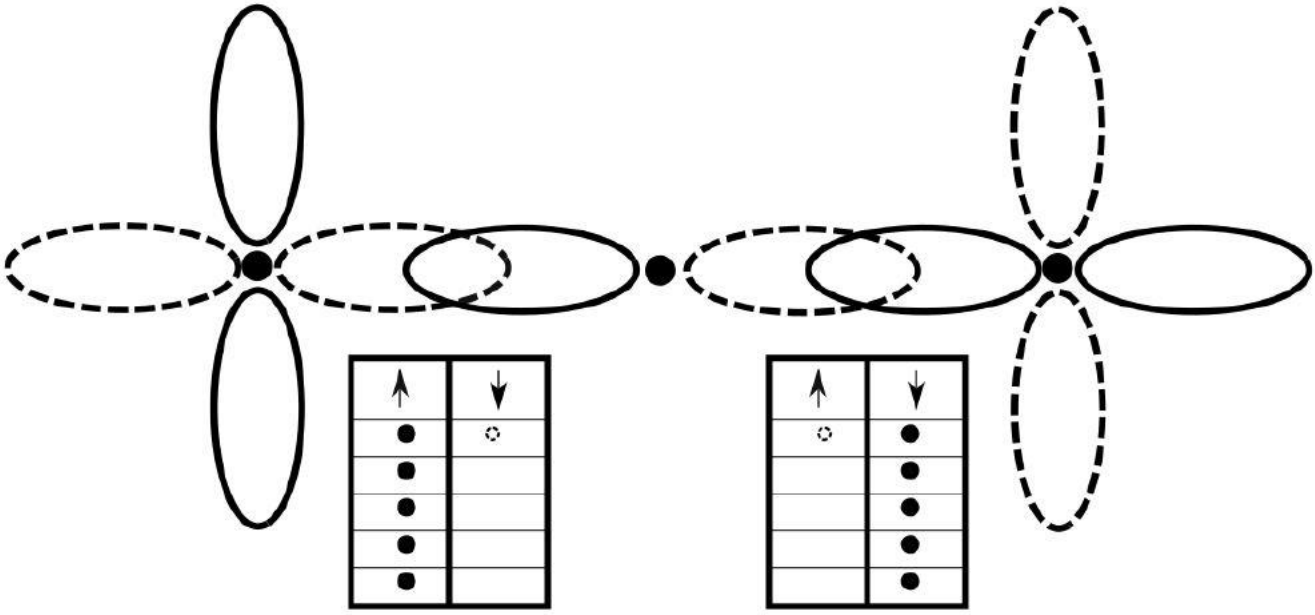

FIG. 2.2 Superexchange interaction between two transition metal ions mediated by an oxygen anion [20].

Having discussed the origin of magnetism, we now should look at different kinds of magnetic materials. There are three types of materials which have a permanent magnetic state in absence of an applied magnetic field – ferromagnets, antiferromagnets and ferrimagnets. Ferromagnets are made up of only one magnetic sublattice with all magnetic moments being parallel to each other. Examples of ferromagnets include iron, nickel and cobalt at room temperature. Antiferromagnets are materials which have zero or

very small magnetic moments based on the nature of ordering. In most cases antiferromagnetic materials are made up of two identical sublattices with their magnetic moments aligned antiparallel to each other. Very small or zero net magnetic moment of antiferromagnetic materials makes their experimental characterization difficult. Louis Neel was the person who discovered and explained antiferromagnetism for the first time [21]. Antiferromagnetic materials are used in hard disk drives (HDDs) where the exchange bias from these materials is used to keep the direction of magnetization of a magnetic layer fixed (as long as we do not apply very strong magnetic field, greater than $H_{\text{exchange bias}}$ in opposite direction). This fixed magnetic layer is then used in the read head in HDD, the technology that is used for data storage with very high density in computers. There have been some developments to be able to use antiferromagnetic materials in next generation memory technologies including demonstration of switching of an antiferromagnetic thin film using electrical current [22]. Antiferromagnetic materials also offer the advantage of very fast magnetization dynamics, in the THz regime [23]. However, a lot more research is required to be able to use antiferromagnetic materials for next generation memory technologies.

Ferrimagnetic materials are another important class of magnetic materials. These materials consist of two or more magnetic sublattices that are coupled to each other antiferromagnetically. However, the different sublattices do not completely nullify each other and there is a net magnetic moment. Examples of ferrimagnetic materials include rare earth iron garnets (like thulium iron garnet), magnetite (Fe_3O_4) and transition metal – rare earth metal alloys (like Co-Gd alloys) [11,24–26]. To be able to identify the nature of magnetic ordering in a material (ferromagnetic versus ferrimagnetic) we need to understand its stoichiometry and positions of atoms of different elements in its unit cell. The magnetic moment of magnetite could not be explained prior to discovery of ferrimagnetism as it was much lower than expected. Later it was found that the moments of two Fe^{3+} ions nullify each other, and the result is moment of one Fe^{2+} ion per formula unit. Iron garnets are an important class of ferrimagnetic materials and they are discussed in greater detail later in this chapter. Ferrimagnetic materials have some advantages over

ferromagnetic materials. Antiferromagnetic coupling between sublattices in ferrimagnetic materials is stronger than exchange coupling in ferromagnetic materials leading to faster spin dynamics in ferrimagnetic materials [27].

We should also mention one more kind of magnetic behavior – paramagnetism. Paramagnetism refers to development of a weak magnetic polarization in a material parallel to the applied magnetic field and proportional to the magnitude of this field. This happens only if the material has unpaired electrons. Spins of these unpaired electrons align themselves parallel to the applied field to reduce the energy of the system. The explanation for the origin of paramagnetism was modified a bit by quantum mechanics as the energy levels of electrons are quantized. Paramagnetism is strongly dependent on temperature and becomes weak at higher temperatures.

Another important property relevant for this thesis is magnetic damping in solids. Damping refers to dissipation of energy through internal mechanisms of a material that transfers energy to crystal lattice [11]. This is similar to viscosity or friction like behavior. Damping of a magnetic solid effects its dynamic behavior like propagation length of spin waves or switching speed. Damping of magnetic insulators is generally lower than that of metallic magnets as conduction electrons contribute to dissipation of energy. Garnets, especially yttrium iron garnet (YIG) [28], are materials among those with lowest known damping. Bismuth substituted yttrium iron garnet (BiYIG) [29] has a damping that is an order of magnitude higher than that of YIG but much smaller than that of rare earth iron garnets (REIGs) like thulium iron garnet (TmIG) [30]. In chapter 6 we study damping of BiYIG|TmIG bilayered films. Landau-Lifshitz-Gilbert (LLG) equation governs the dynamic magnetic behavior of a system:

$$\frac{d\vec{M}}{dt} = \gamma\left(\vec{M} \times \vec{H}\right) - \frac{\alpha}{M}\left(\vec{M} \times \frac{d\vec{M}}{dt}\right) + \gamma\,\alpha^2\left(\vec{M} \times \vec{H}\right) \qquad (2.5)$$

$$\gamma = \frac{g\,e}{2\,m\,c} \qquad (2.6)$$

Here $\vec{M}$ is magnetization vector, $\vec{H}$ is magnetic field vector, α is Gilbert damping, γ is a constant, M is magnitude of magnetization, g is Lande g-factor, e is charge of electron, m is mass of electron and c is speed of light [11].

2.1.2 Spin-Orbit Coupling

As we have mentioned before, an atom has spin and orbital components of angular momentum. These two components are coupled to each other due to a phenomenon known as spin-orbit coupling (SOC). SOC has consequences for several important properties like magnetostriction, Gilbert damping, anisotropy and fields of magneto-optics and spintronics [9].

Spin-orbit coupling refers to the effect of orbital motion of an electron on its spin orientation. From the frame of reference of the electron, nucleus is undergoing orbital motion around it and this orbital motion of positive charge results in a magnetic field that effects the orientation of spin of an electron [9,11]. This explains the origin of SOC. SOC is proportional to the fourth power of atomic number and is significant for heavy metals like platinum and tantalum [31].

2.1.3 Magnetostriction

Magnetostriction is defined as the fractional change in length of a material on being magnetized [9,11]. On application of a magnetic field, the spins in a material undergo a change in direction to align with the field. Due to SOC this also leads to a reorientation of orbitals leading to change in dimension which is quantified by magnetostriction in terms of strain. For a cubic crystal, magnetostriction can be completely described by λ_{100} and λ_{111} which are magnetostriction constants along <100> and <111> crystallographic directions respectively. Magnetostriction constants are small in magnitude, on the order of 10^{-5}. Magnetostriction constants decrease monotonically with increase in temperature. Magnetostriction has important consequences for both bulk solids and thin films. However, for this thesis we will primarily be

concerned with effects of magnetostriction on thin film samples. Magnetoelastic anisotropy induced in a material on application of stress is quantified by magnetostriction.

For epitaxial thin films of materials deposited on substrates with (111) or (100) orientation magnetostriction is specified by the relevant constant. However, for a polycrystalline material with randomly oriented grains we need to take an average of the two magnetostriction constants. Based on the assumption of uniform volumetric stress caused by magnetostriction the following equation has been derived [32]:

$$\lambda = \frac{2}{5}\lambda_{100} + \frac{3}{5}\lambda_{111} \qquad (2.7)$$

Here λ is the magnetostriction of the polycrystalline material. Later, elastic properties of the material were incorporated to obtain the following result [33,34]:

$$\lambda = \lambda_{111} + \left(\frac{2}{5} - \frac{\ln(c)}{8}\right)(\lambda_{100} - \lambda_{111}) \qquad (2.8)$$

Here c is given by:

$$c = \frac{2\,c_{44}}{c_{11} - c_{12}} \qquad (2.9)$$

Here c_{ij}'s are the elastic constants of the material. Incorporating the elastic constants changes the final result by only a few percent for garnets. Although incorporating the elastic constants makes the result slightly more accurate, knowledge of shape of grains is required to make the result more accurate.

2.1.4 Anisotropy

Anisotropy refers to dependence of properties of a material on direction. Energy of a magnetic system may depend on the direction of magnetization. This is of great importance for magnetic materials as the system wants to minimize its energy resulting in certain easy-axis and hard-axis of magnetization. Sources of anisotropy in a material can be intrinsic like the crystal structure of the material and extrinsic like the

stress applied to the material. In the following paragraphs we discuss several different sources of anisotropy – magnetocrystalline anisotropy, magnetoelastic anisotropy and shape anisotropy.

Magnetocrystalline anisotropy arises from interaction between electric field associated with a crystal lattice and anisotropic ($l \neq 0$) orbitals occupied by electrons [9,35]. For a cubic crystal magnetocrystalline anisotropy is given by the following equation:

$$E_{mc} = K_0 + K_1(\alpha_1^2\alpha_2^2 + \alpha_2^2\alpha_3^2 + \alpha_3^2\alpha_1^2) + K_2\alpha_1^2\alpha_2^2\alpha_3^2 + \cdots \qquad (2.10)$$

Here K_i's are cubic magnetocrystalline anisotropy constants and α_i's are cosines of angles made by magnetization direction with <100> crystallographic directions. K_1 and K_2 are sufficient to describe magnetocrystalline anisotropy of most materials. However, for a polycrystalline material with randomly oriented grains there is no magnetocrystalline anisotropy.

Magnetoelastic anisotropy refers to anisotropy that arises on application of mechanical stress on a material. Since the lattice has effect on the anisotropy of a material, distortion of the lattice on application of stress causes magnetoelastic anisotropy in material. Magnetostriction is the quantity that relates the applied mechanical stress and the resulting magnetoelastic anisotropy. For a cubic material, magnetoelastic anisotropy is a function of both directional cosines of stress application direction and directional cosines of magnetization vector [11]. It is given by the following equation:

$$E_{me,cubic} = -\frac{3}{2}\lambda_{100}\sigma\,(\alpha_1^2\gamma_1^2 + \alpha_2^2\gamma_2^2 + \alpha_3^2\gamma_3^2) - 3\,\lambda_{111}\sigma\,(\alpha_1\alpha_2\gamma_1\gamma_2 + \alpha_2\alpha_3\gamma_2\gamma_3 + \alpha_3\alpha_1\gamma_3\gamma_1) \qquad (2.11)$$

Here γ_i's are directional cosines of stress application directions. Magnetoelastic anisotropy for iron garnet films deposited with (111) and (100) orientation have been described in greater detail in chapters 4-7.

Shape anisotropy refers to anisotropy in a material due to its three-dimensional shape. Demagnetizing field in a body with arbitrary shape is lowest along its longest axis [11]. This is because orienting the demagnetizing field along the longest axis of a body keeps the opposite magnetic poles furthest apart. Thus, a sphere is the only shape with zero shape anisotropy. Other important shapes to consider for

demagnetizing factor are ellipse, cylinder and thin films. Shape anisotropy between two different directions is given by:

$$E_{shape} = \frac{1}{2} \Delta N \, M_s^2 \qquad (2.12)$$

Here ΔN is the difference between demagnetizing factors for two directions and M_s is saturation magnetization. The sum of demagnetizing factors along three mutually orthogonal directions is 1 [9].

$$N_x + N_y + N_z = 1 \qquad (2.13)$$

For a spherical body as the three directions are equivalent to each other $N_x = N_y = N_z = 1/3$. For a thin film sample, out-of-plane direction can be defined as the z axis. $N_x = N_y = 0$ for a thin film sample, as the opposite magnetic poles are practically very far apart for a thin film sample for in-plane demagnetizing field direction. Thus, $N_z = 1$ for a thin film sample.

All the different types of anisotropies discussed so far are not dependent on the kinetics of growth process of thin films. Magnetocrystalline anisotropy only depends on the crystal structure of the material, magnetoelastic anisotropy only depends on the nature of stress and magnetostriction of the material and shape anisotropy only depends on the 3D shape of the body being considered. However, growth induced anisotropy in thin films depends on the kinetics of the growth process. Growth induced anisotropy for films deposited by liquid phase epitaxy and pulsed laser deposition has been studied in detail. Growth induced anisotropy in iron garnet films has been discussed in greater detail in the next section.

It is also possible to calculate uniaxial anisotropy constant for a material. Some crystal systems are naturally well described by uniaxial anisotropy, like the hexagonal close packed (HCP) crystal system. In such a crystal generally there is an anisotropy axis and an anisotropy plane, with small anisotropy in the anisotropy plane. Uniaxial anisotropy constant can also be calculated for magnetic thin films to account for the net anisotropy. This can be done by combining contributions of magnetocrystalline, shape, magnetoelastic, growth-induced and any other anisotropy. Calculations of uniaxial anisotropy constant for magnetic thin films has been discussed in greater detail in the following chapters of this thesis. Uniaxial

anisotropy constant, K_u of a material can be used to calculate its anisotropy field along its hard axis (H_k) using the following equation:

$$H_k = \frac{2\,K_u}{\mu_0 M_s} \qquad (2.14)$$

Comparison with the experimental value of anisotropy field can help us understand how accurate our uniaxial anisotropy constant calculation is. On the other hand, if the value of anisotropy field is available with high reliability it can be used to calculate uniaxial anisotropy constant.

2.2 Garnet structure and magnetic properties

Although the rise in interest in PMA REIG thin films is relatively recent, magnetism in garnets is being studied since 1950s. Structure, stoichiometry and magnetic properties of iron garnets have been studied in great detail by Pauthenet, Gilleo, Geller, and Kittel. Garnets have been used for development of magneto-optical magnetic bubble memories [36].

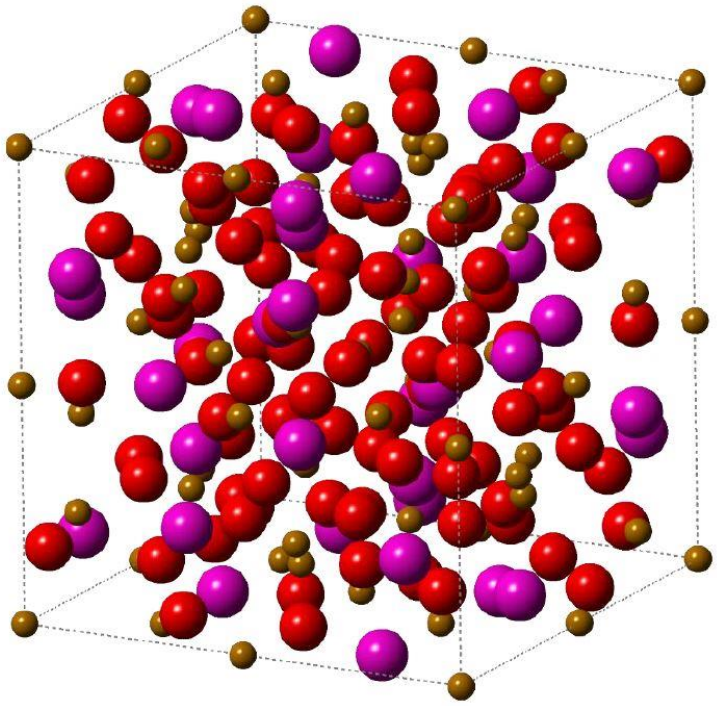

FIG. 2.3 Garnet unit cell. Purple atoms (largest) are dodecahedrally coordinated, yellow atoms (smallest) are Fe and occupy sites that are octahedrally or tetrahedrally coordinated, and red atoms are O [37].

Iron garnets get their name from garnet minerals like $Ca_3Al_2Si_3O_{12}$ which have the same crystal structure as iron garnets [38]. For iron garnets we substitute (Al, Si) with Fe. For the work in this thesis, we have RE (like Tb or Tm), Bi or Y in place of Ca. Additionally, in chapter 4 we describe our work on Sc substitution for Fe. A unit cell of iron garnet consists of eight formula units and a total of 120 ions and has a lattice parameter close to 1.2 nm (see FIG. 3). A unit cell of iron garnet consists of cation sites which are dodecahedrally coordinated by oxygen anions, octahedrally coordinated by oxygen anions and tetrahedrally coordinated by oxygen anions. For each formula unit, 2 Fe^{3+} ions occupy sites which are octahedrally coordinated and 3 Fe^{3+} ions occupy sites which are tetrahedrally coordinated. In REIGs, YIG and bismuth substituted YIG (BiYIG), RE^{3+}, Y^{3+} and Bi^{3+} ions occupy dodecahedrally coordinated sites. Iron garnets films deposited for experiments reported in this thesis did not always have exactly the same stoichiometry as mentioned above.

Iron garnets are ferrimagnetic because of the superexchange interactions [39]. For rare earth iron garnets, iron ions on octahedral and tetrahedral sublattices are antiferromagnetically coupled to each other. Also, rare earth ions on dodecahedral sublattice are ferromagnetically coupled to octahedral sublattice.

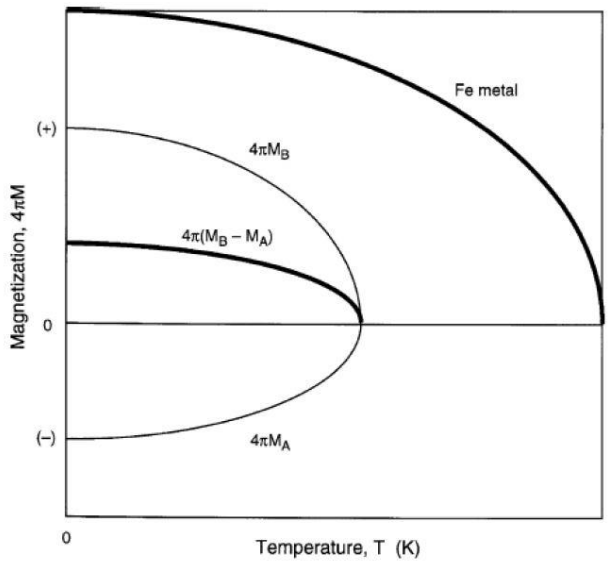

FIG. 2.4 Saturation magnetization versus temperature curve for a two sublattice material and for a single sublattice material [40].

Neel's molecular field theory is used for analysis of magnetic materials [40,41]. This theory assumes that cations are sitting in a mean "molecular" field due to ions in their neighborhood. For YIG the equations based on this theory are [42]:

$$M = M_d - M_a \qquad (2.15)$$

$$M_a = 75.7 B_{\frac{5}{2}} \left(3.359 \times 10^{-4} \times \frac{1}{T}\right) H_a \qquad (2.16)$$

$$M_d = 113.55\, B_{\frac{5}{2}} \left(3.359 \times 10^{-4} \times \frac{1}{T}\right) H_d \qquad (2.17)$$

$$H_a = \lambda_{aa} M_a - \lambda_{ad} M_d \qquad (2.18)$$

$$H_d = -\lambda_{ad} M_a + \lambda_{dd} M_d \qquad (2.19)$$

Here λ_{ij} are the molecular field coefficients, M is the net magnetization, M_i is the magnetization of the sublattice i and $B_{5/2}$ is the Brillouin function for a particle with J = 5/2. This produces the curve for magnetization versus temperature as shown in Fig. 2.4.

In rare earth iron garnets (REIGs) there is an additional magnetic sublattice – dodecahedral sublattice (denoted by c and occupied by the RE^{3+} ions, the largest ions in the system) compared to YIG. Thus, the thermomagnetic behavior of REIGs is more complicated than YIG. The equation for net magnetization above needs to be modified for REIGs:

$$M = |M_a + M_c - M_d| \qquad (2.20)$$

Also, additional molecular field coefficients corresponding to exchange interactions with dodecahedral sublattice need to be introduced [40]. Shielding of rare earth 4f electrons causes RE-RE exchange interactions to be weaker than Fe-Fe and RE-Fe exchange interactions [43]. Moreover, there can be rare earth canting which refers to reduced rare earth magnetization compared to free ion value. Reduction in orbital angular momentum due to crystal field (small but not negligible for rare earth ions) is the reason behind rare earth canting [40].

The presence of RE^{3+} ion in REIGs can also lead to the interesting phenomenon of magnetic compensation temperature. This is of technological relevance as it can enable ultrasmall and ultrafast spin textures [44] and efficient spin orbit torque switching [45]. The exact position of magnetic compensation temperature depends on the distribution of ions in different sublattices and substitution of cations on different sublattices. Compensation temperatures of rare earth iron garnets with small rare earth deficiency and nonmagnetic substitution on octahedral sublattice of varying extents have been discussed in chapter 4 of this thesis. Thermomagnetic behavior of various REIGs have been shown in FIG. 5. The presence of compensation temperature for terbium iron garnet (TbIG) and gadolinium iron garnet (GdIG) can be seen.

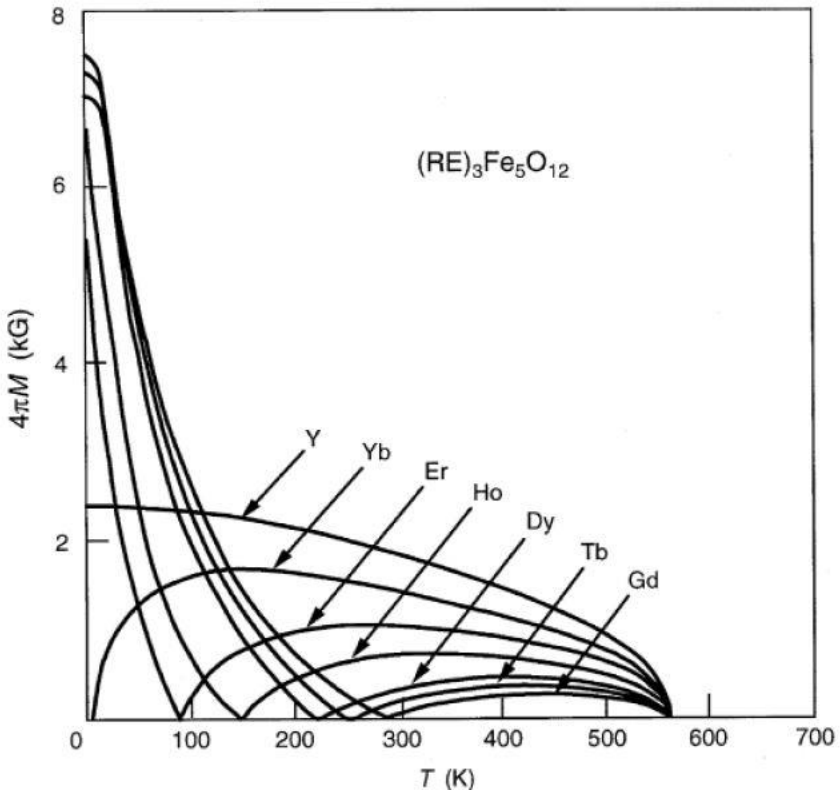

FIG. 2.5 Saturation magnetization versus temperature for various rare earth iron garnets (REIGs). Presence of compensation temperature can be observed for several REIGs and compensation temperatures of TbIG and GdIG are close to room temperature [40].

Let us consider growth induced anisotropy in rare earth iron garnet thin films. It consists of three different sublattices – dodecahedral sublattice (c sites), tetrahedral sublattice (d sites) and octahedral sublattice (a sites). c sites can be of three different types (non-equivalent to each other) based on the closest d sites – c

sites with d sites on left and right (X), c sites with d sites on back and front (Y) and c sites with d sites above and below them (Z) [46]. Further, these c sites can be classified based on their closest a sites into X_i, Y_i and Z_i where i = 1, 2, 3 or 4 [46]. During the deposition of a rare earth iron garnet film with mixed rare earth ions on a substrate with (111) orientation [36], incoming rare earth ions would see two classes of dodecahedral sites with different areas. The larger rare earth ion would have a smaller energy barrier for incorporation into the dodecahedral site with larger area. This causes preferential occupancy of non-equivalent dodecahedral sites by rare earth ions of different sizes, breaking symmetry of crystal and giving rise to a growth-induced anisotropy contribution.

2.2.1 Nonmagnetic substitution in iron garnets

Complexity of garnet crystal structure consisting of various sublattices allows substitution of nonmagnetic cations on different types of sites. Different ions have preference to occupy specific sublattices based on their size. In this thesis we only deal with cations which exclusively occupy a particular sublattice. Geller and his coworkers did a significant amount of work on nonmagnetic cation substitution in YIG in 1960's. Table I gives a summary of site preferences of various cations in iron garnet systems. For substitution by cations which have charge different from +3, it is necessary to compensate for the difference in charge. This is generally achieved by Ca^{2+} substitution on the c sublattice for the cases of Sb^{5+}, Si^{4+}, V^{5+} and Zr^{4+} substitution [47,48].

Substitution of different cations on various sublattices of iron garnets allow control over magnetic properties of material. Exclusive substitution of diamagnetic cations in tetrahedral sublattice should reduce the net magnetic moment and exclusive substitution of diamagnetic cations in octahedral sublattice should increase the net magnetic moment. However, this holds true only up to a certain level of substitution beyond which the magnetization begins to decrease. The reason for this is the decrease in the average antiferromagnetic superexchange interactions experienced by an ion. Magnetometry and neutron diffraction experiments have shown that substitution on a particular sublattice (octahedral/tetrahedral)

causes canting of magnetic moments on the opposite sublattice [49,50]. Efforts to model this using molecular field coefficients have been difficult as the magnetic behavior depends on the choice of the diamagnetic ion [51–53]. The amount of substitution beyond which intra-sublattice interactions and canting begin to dominate over inter-sublattice interactions has been found experimentally for several species. On a per formula unit basis the transition happens at $X_{octa} = 0.7$ and $X_{tetra} = 1.92$ [47].

Table 2.1 – Site preference for several ions which exclusively occupy a particular sublattice

Ion	Crystallographic Site	Reference
Bi^{3+}	Dodecahedral	[54]
Ca^{2+}	Dodecahedral	[48]
Hf^{4+}	Octahedral	[55]
In^{3+}	Octahedral	[56]
Sb^{5+}	Octahedral	[57]
Sc^{3+}	Octahedral	[48]
Zr^{4+}	Octahedral	[48]
Si^{4+}	Tetrahedral	[48]
V^{5+}	Tetrahedral	[48]

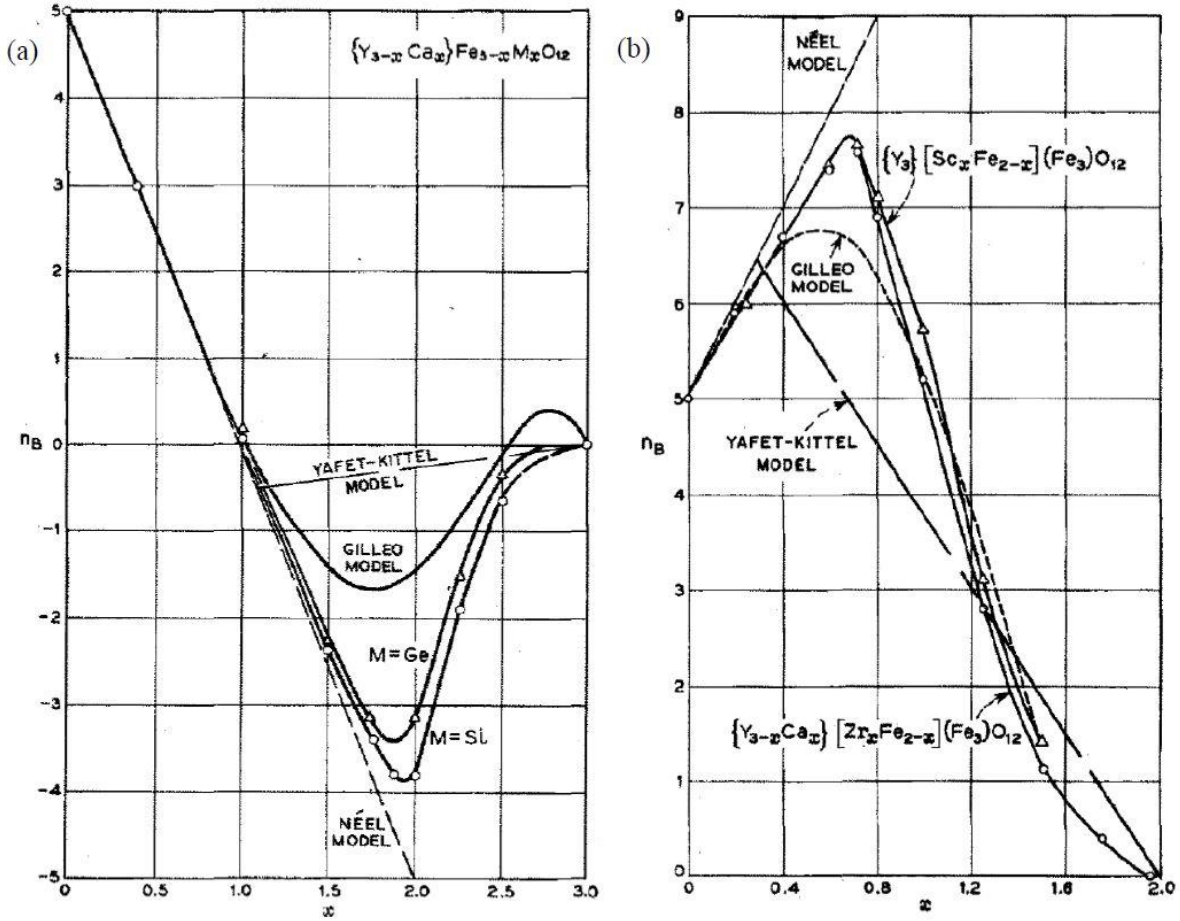

FIG. 2.6 Magnetic moment per formula unit (in μ_B) versus amount of site-specific substitution in YIG. (a) Plots for Si^{4+} and Ge^{4+} substitution in tetrahedral sites (Ge^{4+} does not exclusively occupy tetrahedral sites, a fraction of it goes to octahedral sites as well). (b) Plots for Sc^{3+} and Zr^{4+} substitution in octahedral sites. Charge compensation for Si^{4+}, Ge^{4+} and Zr^{4+} substitution is achieved by substitution of Ca^{2+} ions in dodecahedral sublattice. Reduction in magnetic moment can be observed beginning from about X_{tetra} = 1.9 and X_{octa} = 0.7 [47].

2.3 Spintronic phenomena in iron garnets

So far we have discussed structural and magnetic properties of iron garnets. In this section we will discuss dynamic properties of iron garnets. The motion of a magnetic moment is governed by the Landau-Lifshitz-Gilbert (LLG) equation. It can be written as [58]:

$$\frac{\partial m}{\partial t} = \gamma_{LL}\left(\frac{1}{1+\alpha^2}\right)\left(m \times B_{eff} + \alpha\, m \times \left(m \times B_{eff}\right)\right) \qquad (2.21)$$

Here γ_{LL} is the gyromagnetic ratio (ratio of magnetic moment and angular momentum), α is the Gilbert damping and is related to energy dissipation in a magnetic material (spin-orbit coupling contributes to this energy dissipation) and B_{eff} is the effective magnetic field in a material and consists of contributions from

exchange, anisotropy and applied field. Spintronics enters into the picture when we look at additional sources of effective magnetic field which may act in a device. One such source that we will consider in this section is spin-orbit torque (SOT). To understand SOT one needs to understand spin current in a solid.

2.3.1 Drift-Diffusion Model for Spin Current

In addition to charge an electron possesses spin angular momentum. Thus, a moving electron can carry both charge current and spin current. An understanding of these two types of currents is required to understand phenomena related to SOT. We will describe the formalism developed by Valet and Fert using drift-diffusion equations to understand charge current and spin current [59]. Under this formalism charge current and spin current are coupled to each other and are governed by chemical potentials of both charge accumulation and spin accumulation. Charge and spin accumulations obey the following equations:

$$\nabla^2 \mu_{S,i} = \frac{\mu_{S,i}}{\lambda^2} \qquad (2.22)$$

$$\nabla^2 \mu_c = 0 \qquad (2.23)$$

Here $\mu_{S,i}$ is the i^{th} component of the spin chemical potential vector and λ is the spin diffusion length $\sqrt{D\,\tau_{sf}}$, the characteristic length over which spin accumulation decays to zero in a nonmagnetic metal [60]. D is the spin diffusion coefficient and τ_{sf} is the spin flip scattering time, the time taken by a spin in a spin state to scatter to another spin state [60]. Charge and spin currents in a material with conductivity σ are given by [61]:

$$j_c = \frac{-\sigma}{e} \nabla \mu_c \qquad (2.24)$$

$$j_{S,i} = \frac{-\sigma}{2e} \nabla \mu_{S,i} \qquad (2.25)$$

Charge current and spin current in some materials are coupled to each other by spin-Hall effect [61]. Charge current in a material can originate from a combination of charge accumulation and spin accumulation (inverse spin-Hall effect (ISHE)) and spin current in a material can originate from a

combination of spin accumulation and charge accumulation (SHE). This is important to understand one of the possible origins of SOT [62,63] as well as a measurement technique, spin-Hall magnetoresistance [61].

In bilayers made up of ferrimagnetic insulators (FMI) and nonmagnetic metals (NM) charge current can only flow through the nonmagnetic metals, parallel to the interface. However, spin current can flow through the structure in transverse direction. To understand this spin current flow, one needs to consider what happens at the interface. For this purpose, we describe below the magnetoelectronic circuit theory.

Magnetoelectronic circuit theory of Brataas can be used to describe spin transfer across an NM|FMI interface [64]. According to this theory spin current across an FMI|NM interface is made up of two components as described by the following equation [61]:

$$ej_S^{(NM|FMI)}(\hat{m}) = -G_r\,\hat{m} \times (\hat{m} \times \mu_S) - G_i\,(\hat{m} \times \mu_S) \qquad (2.26)$$

Here G_r and G_i are real and imaginary components of magnetoelectronic circuit theory parameter spin mixing conductance. In chapter 4 we look at the role of iron sublattice in spin mixing conductance of REIG|Pt interface.

2.3.2 Spin-Orbit Torque

A transverse spin current in REIG|Pt heterostructure can give rise to effective field (and thus torque) on the magnetization of magnetic layer. Spin-orbit torque has two components with different symmetries corresponding to G_r and G_i respectively. The two components are given by the following equations:

$$\tau_{DL} \propto m \times (\sigma \times m) \qquad (2.27)$$

$$\tau_{FL} \propto \sigma \times m \qquad (2.28)$$

Here τ_{DL} refers to damping-like torque (related to G_r) and τ_{FL} refers to field-like torque (related to G_i) [8]. SOT can cause switching of the magnetization of the magnetic layer if its magnitude is large enough and if an in-plane magnetic field is applied parallel to the current. The in-plane magnetic

field parallel to current is required to break the symmetry of clockwise versus anticlockwise rotation of magnetization vector [63]. Based on macrospin assumption, critical current required for SOT induced magnetization reversal is given by [65]:

$$J_{critical} = \frac{2\,e}{\hbar}\frac{M_S\,t_F}{\Theta_{SH}}\left(\frac{H_{K,eff}}{2} - \frac{H_x}{\sqrt{2}}\right) \qquad (2.29)$$

Here M_S and t_F are saturation magnetization and thickness of ferrimagnetic insulator film (like a REIG) and Θ_{SH} is the spin-Hall angle of nonmagnetic metal overlayer (like Pt). $H_{K,eff}$ is the anisotropy field including shape anisotropy and H_x is the applied in-plane field.

SOT has been extensively studied in REIG|Pt heterostructures over the past few years. SOT was demonstrated to induce coherent auto-oscillations in YIG in 2016 [66]. SOT assisted switching of Pt|$BaFe_{12}O_{19}$ was also demonstrated in 2016 [67]. In the same year all electrical SOT switching of Pt|TmIG was demonstrated by our group [8]. There have been improvements in SOT switching efficiency due to advances in PLD growth [68] and SOT switching has been demonstrated for TmIG films with thickness up to 15 nm [69]. Efficient SOT-driven domain wall motion has been demonstrated for Pt|TmIG heterostructure [6,70]. Ultrafast SOT-driven domain wall motion has been demonstrated in BiYIG with velocity up to 4.3 km/s [71].

2.3.3 Dzyaloshinskii-Moriya interaction (DMI)

Dzyaloshinskii-Moriya interaction (DMI) [72,73] may exist in bulk materials with broken inversion symmetry or thin films where interfaces break inversion symmetry. Two important ingredients for DMI are broken inversion symmetry and strong spin-orbit coupling. The Hamiltonian for DMI interaction is given by:

$$\widehat{H} = -\sum_{i\,j} D_{ij} S_i \times S_j \qquad (2.30)$$

Here D_{ij} is the Dzyaloshinskii-Moriya tensor and S_i and S_j are adjacent spins. Unlike Heisenberg exchange interactions which favor collinear ferromagnetic/antiferromagnetic alignment of adjacent spins, DMI favors directional non-collinear magnetic order of a specific chirality, left-handed or right-handed based on the sign of D_{ij}. In a material with significant Heisenberg exchange interaction and DMI, the two compete with each other resulting in formation of chiral domain walls and skyrmions as shown in FIG. 7.

DMI has been found to exist in non-centrosymmetric bulk materials like MnW [74], MnSi [75] and FeGe [76] as well as bilayers of ferromagnetic materials and heavy metals like Pt, Ta or W with strong spin orbit coupling where presence of interface results in broken inversion symmetry (shown in FIG. 8) . For centrosymmetric bulk materials $D_{ij} = 0$ and thus there is no DMI. Interfacial DMI stabilized homochiral Neel domain walls were observed in Pt|Co(Fe)|oxide films by Emori [77] and Ryu [78] separately. In chapter 6 of this thesis we study interfacial DMI for BiYIG, thulium substituted BiYIG (TmBiYIG) and BiYIG|TmIG bilayers deposited on various garnet substrates.

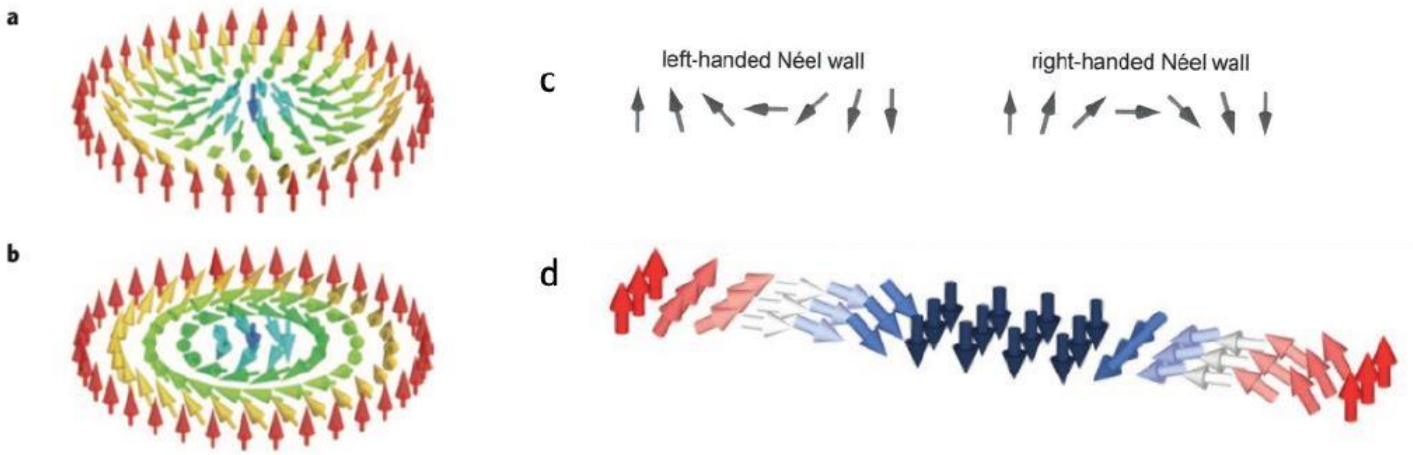

FIG. 2.7 (a) Bloch and (b) Neel skyrmions (c) Left-handed and right-handed Neel domain walls (d) A pair of right-handed Neel domain walls [79]

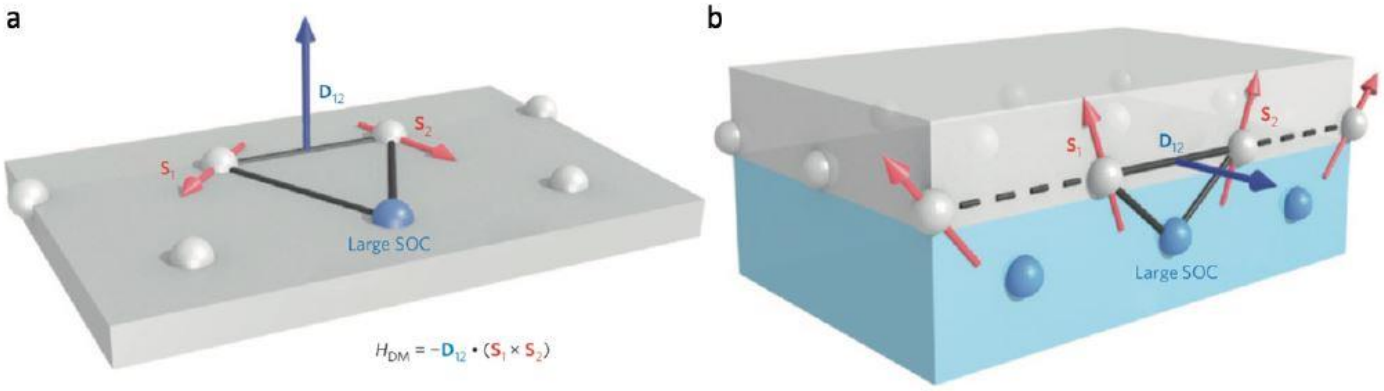

FIG. 2.8 Sketch of (a) bulk DMI in non-centrosymmetric crystal (b) interfacial DMI in ferromagnet|heavy metal bilayer [80].

Chapter 3: Experimental methods

This chapter discusses the experimental methods used throughout this thesis. Thin films were deposited using pulsed laser deposition and platinum overlayers on these thin films were deposited using sputtering system in Prof. Luqiao Liu's laboratory. X-ray reflectivity (XRR) was used for determination of thickness of films. X-ray diffraction (XRD) was used to characterize structure of these thin films and surface roughness information was obtained using atomic force microscopy (AFM). Room temperature hysteresis loops and temperature dependent magnetic properties of these thin films were obtained using vibrating sample magnetometry (VSM). TEM images for cross-sections of thin films were obtained to get information about their structural quality and composition profile. The TEM lamella sample was prepared by VELION FIB-SEM system, with Au^+ ion beam working at 35 keV, followed by ion polishing by Ar+. The high-angle annular dark-field (HAADF) and energy dispersive spectroscopy (EDS) images were acquired on a Themis Z STEM working at 200 keV with chromatic corrector. Hall crosses for spin-Hall magnetoresistance (SMR) measurements were patterned using photolithography with maskless aligner (MLA).

Wavelength dispersive spectroscopy (WDS) measurements were performed on garnet films with thickness greater than 200 nm using a JEOL JXA-8200 electron probe microanalyzer with an accelerating voltage of 15 kV and a beam current of 10 nA, and the data were reduced with the GMRFILM software package for thin film analysis which considers the contribution of substrate to WDS spectrum and effect of substrate/film interface [81]. X-ray photoelectron spectroscopy (XPS) was used to obtain qualitative information about composition of scandium substituted TbIG (TbScIG) thin films. High-resolution XPS spectra were taken using a Physical Electronics VersaProbe II for TbScIG films with thickness less than 90 nm. Adventitious carbon on the sample surface was removed by a cleaning procedure using an argon ion beam before acquiring data. A pass energy of 23.5 eV was used to acquire data. Atom probe tomography (APT) was used to characterize composition modulation in TbIG-TmIG multilayered thin

films. Specimen tips for the 3D APT were prepared using an FEI Helios 660 Nanolab Dual-Beam FIB/SEM. Standard APT sample preparation procedures were followed for the lift out; sharpening of the tips was performed first with an ion beam accelerating voltage of 30 kV, and then (for final shaping and cleanup) at 2 kV. APT was performed using a Cameca LEAP 4000X HR instrument in laser pulsing mode, with the following operating conditions: laser pulse energy of 20 pJ and repetition rate of 100 kHz; base temperature of 40 K; detection rate of 1%. Reconstruction and analysis of the data was performed using Cameca IVAS 3.6.14 software. A 1D concentration profile along a cylindrical sub-volume parallel to the long axis of the specimen tip was extracted; the ion counts were converted into cation ratios. The accurate oxygen content cannot be determined via APT because oxygen field evaporates as both O+ and O2++, which have the same mass-to-charge-ratio.

3.1 Pulsed Laser Deposition (PLD)

Pulsed laser deposition (PLD) is a physical vapor deposition technique which allows non-equilibrium deposition of thin films with complex stoichiometry. It combines characteristics of evaporation and sputtering and has several advantages over other physical vapor deposition techniques. Demonstration of deposition of high quality $YBa_2Cu_3O_7$ thin films by PLD attracted attention for deposition of many oxide thin films by the same technique [82]. In PLD laser pulses hit the target resulting in formation of plume with atomic species of target material which get deposited on the substrate. A schematic of the PLD equipment used in this thesis has been shown in FIG. 1. The key components of this PLD system are deposition chamber, optics, laser (a Coherent COMPexPro 205 KrF with wavelength 248 nm excimer laser), mechanical pump, turbomolecular pump, substrate and target. Duration of laser pulses is in ns range. As most materials are absorptive for this wavelength, energy of the laser pulse gets absorbed by the target resulting in formation of plume with atomic species of target material. Laser pulses are guided and focused by optical components made up of high-quality quartz and energy of about 2-3 J/cm^2 is incident on target surface. The spot on target where the laser pulse is incident vaporizes on absorbing some energy

from laser pulse and the vapor absorbs more energy from laser pulse to form a dense plasma. This plasma absorbs more energy from laser pulse and expands to form a plume perpendicular to the surface of target, resulting in deposition of atomic species of target material on substrate which is placed directly above the target. Base pressure in 10^{-6} Torr range results in high purity of deposited thin film. Chamber is either at vacuum or oxygen atmosphere at room temperature or high temperature. Substrate is continuously rotated during film deposition to achieve greater uniformity in composition and thickness of film. Target is continuously rotated and rastered while being ablated by laser to achieve uniform ablation of target.

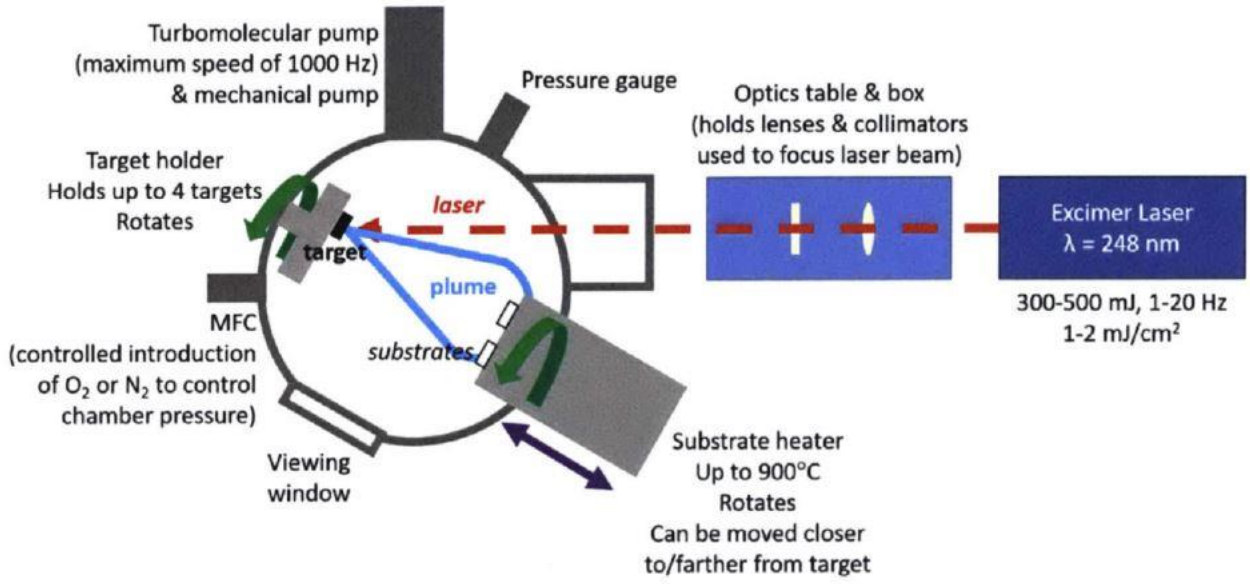

FIG. 3.1 Schematic of PLD equipment used for deposition of thin films in this thesis [83].

Some of the advantages of thin film deposition using PLD are:

1. PLD allows deposition of multilayered films. Rotation of carousel holding the targets allows use of multiple targets in the same deposition which can be used for deposition of multilayered epitaxial and polycrystalline films.
2. PLD allows combinatorial growth. Two targets with different compositions can be used for combinatorial growth by offsetting the substrates and targets. This allows deposition of thin films with compositions that vary linearly between two compounds.

3. PLD system is modular in nature allowing decoupling of growth chamber from laser. This allows use of lasers with different powers, wavelengths and pulse widths. This enables PLD growth of different classes of materials.

   One limitation of PLD is due to its forward-directed plume nature which causes nonuniform film thickness or composition. This problem is usually resolved by rotation of substrate holder and raster scanning of laser on target surface.

3.2 Fabrication of garnet targets for PLD

Targets of TbIG ($Tb_3Fe_5O_{12}$) and TbScIG ($Tb_3Sc_{1.5}Fe_{3.5}O_{12}$) were prepared by conventional mixed oxide sintering method. Furnace in Prof. Harry Tuller's lab was used for this purpose. Targets with right stoichiometry were prepared by mixing powders of Tb_4O_7, Fe_2O_3, Sc_2O_3 and Tb_2O_3 (purity of all above 99.9%) in correct ratio based on the reaction equations for calcination and sintering. After mixing and grinding of powders using mortar and pestle, they were ball milled using alumina grinding media and ethanol for 24 hours. This was followed by calcination at 1400 °C for 12 hours in a tube furnace. Processes of mixing, grinding and ball milling were repeated after this. This was followed by cold isostatic pressing to form cylindrical disks of diameter 1 inch using a pressure of 40,000 psi for 2 minutes. Finally these cylindrical disks were sintered at 1400 °C for 18 hours in a tube furnace.

3.3 X-ray Diffraction (XRD) and X-ray Reflectometry (XRR)

X-rays were used in this thesis for phase identification and determination of lattice mismatch, out-of-plane lattice parameter and thickness measurement. X-ray techniques used in this paper include high resolution x-ray diffraction (HRXRD) using 1DXRD (ω-2θ scan), x-ray reflectometry (XRR) and reciprocal space mapping (RSM). Bruker D8 Discover diffractometer was used for HRXRD measurements on epitaxial iron garnet thin films.

ω-2θ coupled scan collected using x-ray detectors as shown in FIG. 2 can be used for phase identification. Incident angle ω is defined as the angle between x-ray source and sample and diffracted angle 2θ is defined

as the angle between incident beam and detector angle. Coupled scan is a plot of scattered intensity versus 2θ, but ω changes as well (linked to 2θ).

The same equipment that is optimized for HRXRD measurements can be used for thickness determination using XRR measurements. XRR measurements involve grazing but varying incident angle and matching detector angle that collects x-rays scattered from sample surface. A fit to Kiessig fringes in XRR scan is used for thickness determination. An XRR model is constructed based on electron densities in different layers using Bruker Leptos software. The parameters that this model fits are thickness of different layers, their densities and their surface roughness values. Fitting this model to experimental XRR data allows determination of thickness and surface roughness up to an accuracy of 0.1 nm.

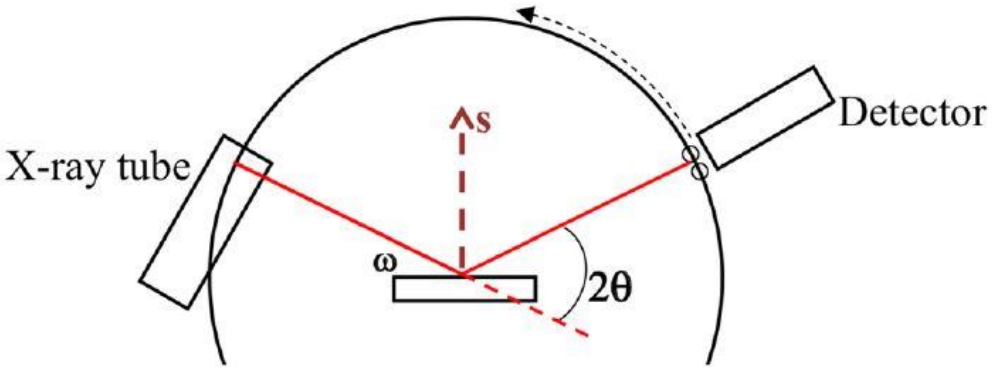

FIG. 3.2 Coupled ω-2θ configuration for XRD measurements [84].

RSM can be used to determine in-plane lattice parameter, out-of-plane lattice parameter and strain state of the film. RSM measurement is performed by collecting 2θ-ω scans for several different values of tilt Δω. Data obtained from a single coupled asymmetric scan is enough to extract in-plane lattice parameter and out-of-plane lattice parameter of both film and substrate. Reciprocal space units used to present RSM are proportional to inverse of lattice constants. In chapter 4 of this thesis we present RSM scan for TbScIG film deposited on GGG substrate and in chapter 5 of this thesis we present RSM scans for BiYIG films deposited on GSGG substrates.

3.4 Vibrating Sample Magnetometry (VSM)

VSM is the most common method for measurement of a sample's magnetization as a function of the applied magnetic field. A schematic of the VSM used for performing measurements in this thesis has been shown in FIG. 3. VSM works on the principle of Faraday's law of electromagnetic induction which states that electromotive force (emf) generated in a pickup coil is directly proportional to the rate of change of magnetic flux through the turns of the pickup coil. Sample is attached to a diamagnetic sample holder made up of Pyrex glass and placed between the pickup coils. The sample holder is vibrated along the z axis. Oscillation of the magnetic sample along with change in its magnetization with change in the applied magnetic field causes change in magnetic flux passing through pickup coil which generates voltage which is then converted to magnetic moment in emu. The magnetization of sample is recorded as the applied magnetic field changes to give hysteresis loop for the sample. We measure hysteresis loops for both out-of-plane orientation (perpendicular to film plane) and in-plane orientation (parallel to film plane) for many different materials throughout this thesis. A Ni standard was used as reference and calibration was performed before each set of measurements to ensure that the ratio between voltage generated in pickup coils and magnetic moment is same for all the measurements.

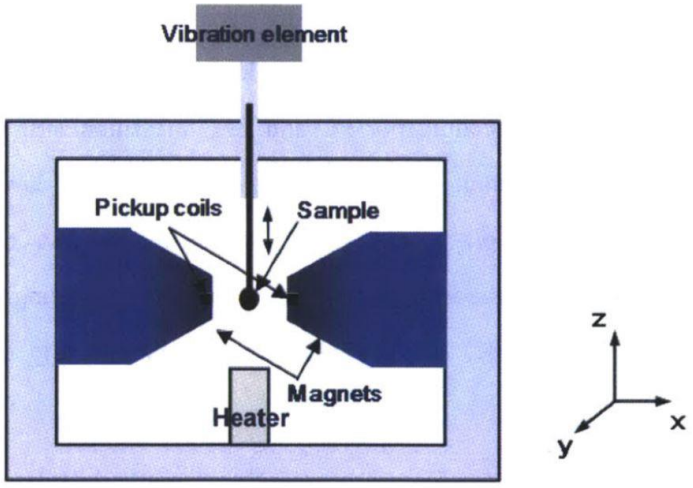

FIG. 3.3 Schematic of VSM setup [84]

3.5 Ferromagnetic resonance (FMR) characterization

Landau-Lifshitz-Gilbert equations (LLGE) is used to model magnetization dynamics in a material. It tells us about the time rate of change of normalized magnetization, **m** = M/M_s:

$$\frac{\delta m}{\delta t} = -|\gamma|\, m \times H_{eff} + \alpha\, m \times \frac{\delta m}{\delta t} \qquad (3.1)$$

Here α is Gilbert damping parameter, γ is Gyromagnetic ratio and H_{eff} is the "effective magnetic field" exerting torque on magnetic moment and causing it to precess around it. The first term on right hand side of the above equation is the precession term and second term on right hand side is the damping term that aligns magnetic moment towards H_{eff}. Damping is a measure of how fast the precession decays and aligns towards H_{eff} as shown in FIG. 4.

In chapter 6 of this thesis we report dynamic properties of BiYIG, TmBiYIG and BiYIG|TmIG bilayers on different substrates. The damping was measured using broadband perpendicular ferromagnetic resonance (FMR) spectroscopy with a vector network analyzer (VNA) in the frequency range 10-40 GHz [85–87]. The complex transmission parameter S_{21} was measured at a particular frequency as the magnetic field was swept [85]. Damping α of the films was obtained by fitting FWHM linewidth ΔH to the following equation [85]:

$$\Delta H = \frac{4\pi\alpha f}{|\gamma|\,\mu_0} + \Delta H_0 \qquad (3.2)$$

ΔH is obtained by fitting the S_{21} data to the complex susceptibility. *f* is the excitation frequency, ΔH_0 is the inhomogeneous linewidth broadening and γ is the gyromagnetic ratio given by $(g\mu_B)/\hbar$ where μ_B is the Bohr magneton, $\hbar$ is the reduced Planck's constant and g is the Lande´ g-factor. The resonance field was fitted to the Kittel equation for perpendicular geometry [85]:

$$H_{res} = \frac{2\pi f}{|\gamma|\,\mu_0} + M_{eff} \qquad (3.3)$$

Here H_{res} is the resonance field, and M_{eff} is the effective magnetization. M_{eff} obtained from the fit was used to calculate the net anisotropy of these films K_u using the following equation:

$$K_u = \frac{-\mu_0 M_s M_{eff}}{2} \qquad (3.4)$$

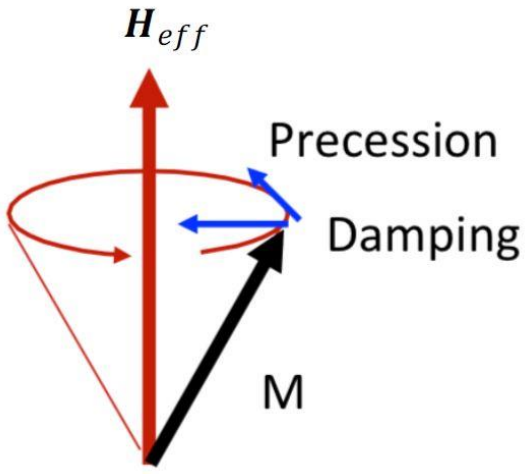

FIG. 3.4 Magnetization dynamics of a moment [79].

In chapter 7 of this thesis, we present net anisotropy and resonance linewidth at different frequencies for BiIG, LuIG, codeposited BiLuIG and multilayered BiIG-LuIG system. A custom assembled broadband FMR system with a coplanar waveguide was used to perform the measurements. An ac magnetic field was applied perpendicular to the film while an in-plane dc magnetic field H was swept from 0 Oe to 6000 Oe. The experiment was repeated for different frequencies of the ac field ranging from 5 GHz to 17 GHz. The resonance field H_{res} and linewidth ΔH were determined for each frequency by fitting the detected voltage with the derivative of sum of a symmetric and antisymmetric Lorentzian [88]:

$$P = \frac{d}{dH}\left[\frac{S\,\Delta H^2 + A_s(H - H_{res})}{4(H - H_{res})^2 + \Delta H^2}\right] \qquad (3.5)$$

Here S and A_s are arbitrary fitting constants. Lande g-factor and M_{eff} were obtained for all films by fitting frequency of ac magnetic field f and H_{res} to the following equation [89]:

$$f = \frac{g\,\mu_0\mu_B}{2\pi\hbar}\sqrt{H_{res}(H_{res}+M_{eff})} \qquad (3.6)$$

Net anisotropy of films was calculated from M_{eff} using the equation mentioned on previous page.

3.6 Brillouin light scattering (BLS)

DMI in a material manifests itself as nonreciprocal propagation of spin-waves. This implies that for a given wavelength, two counter propagating spin-waves do not have the same frequency for a film with in-plane magnetization and wave-vector perpendicular to magnetization. BLS can be used to measure this asymmetric dispersion. Laser is incident on sample surface and photons are inelastically scattered by spin-waves. According to momentum conservation, magnons with wavevector $|k| = 4\pi \sin(\theta)/\lambda$ (here λ is wavelength of incident laser and θ is angle between incident laser and normal to film surface) that are propagating towards incoming laser beam are absorbed (anti-Stokes process) and those propagating in the opposite direction are created (Stokes process) as shown in FIG. 5. Frequency shift in reflected light alters the dispersion relation. In a symmetric material with no DMI, clockwise spin-waves propagating in +x direction and counterclockwise spin-waves propagating in -x direction are present in equal amounts. However, in a material with DMI with in-plane magnetization and spin-waves propagating perpendicular to magnetization, DMI causes a change in spin-wave frequency according to the following equation [90]:

$$f = f_o + \Delta f_{DMI} \qquad (3.7)$$

Here f_o is the spin-wave frequency in absence of DMI and

$$\Delta f_{DMI} = \frac{2\gamma}{\pi M_s} Dk \qquad (3.8)$$

Here γ is the Gyromagnetic ratio, D is the DMI constant and M_s is the saturation magnetization of the film [91].

In chapter 6 of this thesis, we present DMI measurements for BiYIG and BiYIG|TmIG bilayers on various substrates. The BLS measurements were performed in backscattering geometry using a (3+3) tandem Fabry-Pérot interferometer [92] and 532 nm continuous-wave laser of 532 nm wavelength. The thermally generated Damon-Eshbach [93] mode was measured with in-plane applied field of 0.5 T. The wavevector of the DE mode was then determined by the angle θ between the film normal and incident laser, given by $k = \frac{4\pi}{\lambda} sin\Theta$. Each Stokes and anti-Stokes frequency was obtained from the Voigt fitting of the BLS spectra. Voigt fit and Lorentzian fits for the experimental data yielded similar values for frequency, but the Voigt fit resulted in a lower error bar.

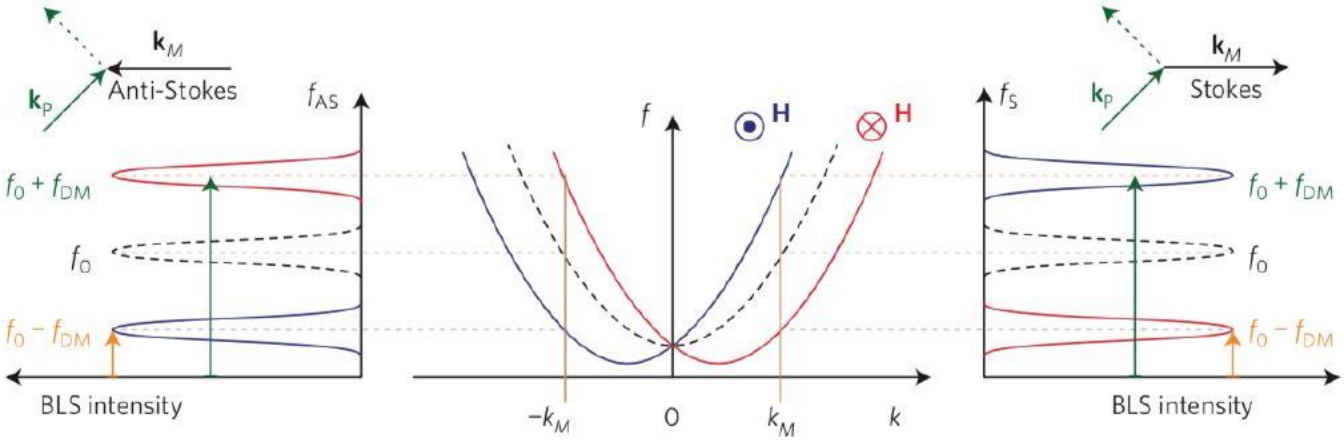

FIG. 3.5 Left panel shows BLS spectra for anti-stokes process and the right panel shows BLS spectra for stokes process. Spin wave dispersion in presence and absence of DMI are shown by solid and dashed curves respectively in central panel [90].

3.7 Measurement of spin-Hall magnetoresistance (SMR)

Heavy metals (HMs) such as Pt and Ta exhibit a strong spin-orbit interaction which enables efficient conversion of charge current to spin current and vice versa [94]. Flow of charge current through the HM layer produces a spin current perpendicular to the HM layer due to the spin Hall effect (SHE) as shown in FIG. 6a. Reflection/absorption of this spin current at the ferrimagnetic insulator (FMI)|HM interface depends on the relative orientation of polarization of the spin current and the magnetization of the FMI (m). The reflected spin current can produce a charge current by the inverse SHE (ISHE) (as shown in FIG.

6b) which modulates the longitudinal resistance of the HM layer. The resultant magnetoresistance for the FMI|HM bilayer is the SMR [95].

Spin mixing conductance parameterizes the transparency of the FMI|HM interface to the flow of spin current through it [95], and it is crucial for a variety of spintronics phenomenon including spin pumping [96], SOT [97], and SMR. SMR measurements have been extensively used to obtain spin mixing conductance of REIG|HM interfaces [98–100]. The additional contribution to longitudinal resistance due to SMR has the symmetry $\Delta R^{SMR} \propto m_y^2$, assuming current flow in the HM layer along the x direction and normal to the film plane along the z direction. There is also a transverse component of SMR with symmetry $R_H^{SMR} \propto m_x m_y$. In addition to this, the imaginary component of spin mixing conductance gives rise to an AHE-like SMR contribution (much smaller than R_H^{SMR}), with symmetry $R_H^{AHE,SMR} \propto m_z$. Combining the above contributions with the ordinary Hall effect (OHE) of the HM layer, we can write the transverse Hall resistance R_H as:

$$R_H = R_H^{SMR} sin^2\theta \sin(2\phi) + R_H^{AHE,SMR} \cos\theta + R_H^{OHE} H_z \qquad (3.9)$$

Here, θ and ϕ are the polar and azimuthal angles of m, respectively, and R_H^{OHE} is the OHE of the HM layer due to magnetic field H_z. In chapter 4 of this thesis, we present SMR measurements for Pt|TbScIG thin films and obtain spin mixing conductance as a function of Sc content. In chapter 5 of this thesis, we report similar measurements for Pt|BiYIG. In chapter 7 of this thesis, SMR measurements are reported on TbIG-TmIG multilayered films to obtain their anisotropy field values.

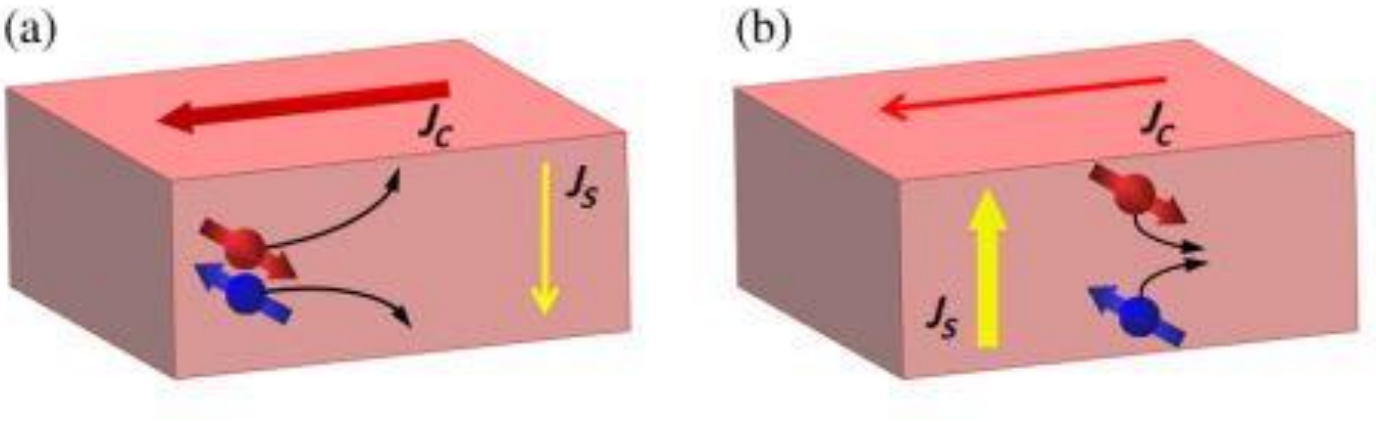

FIG. 3.6 (a) Spin-Hall effect and (b) inverse span-Hall effect in a nonmagnetic metal. Flow of a charge current causes generation of a spin current perpendicular to it as shown in (a) and flow of a spin current causes generation of a charge current perpendicular to it as shown in (b). Polarization of spin current is perpendicular to both charge current and spin current in both cases [101].

3.7.1 Fabrication of spintronic devices using lithography

Pt overlayer was deposited on thin film of iron garnet. This was followed by fabrication of Hall crosses using photolithography. Heidelberg DirectWrite-MLA-150-OptAF was used to perform maskless lithography. MLA is a direct-write laser system which exposes UV sensitive photoresist to 375 nm or 405 nm laser diode. It does not require any mask fabrication. Flow chart for the photolithography process using MLA is shown in FIG. 7. First AZ3312 photoresist was spin coated on garnet|Pt heterostructure at 4500 rpm. This was followed by prebaking at 102 °C for 1 minute. It was then exposed to 375 nm diode laser using MLA with dose of 100 mJ/cm^2. This was followed by post baking at 112 °C for 1 minute. After this it was developed in AZ300 for 75 seconds. This was followed by ion milling using Ar plasma which leaves behind region protected by resist. The resist is then removed by using acetone or N-Methylpyrrolidone (NMP).

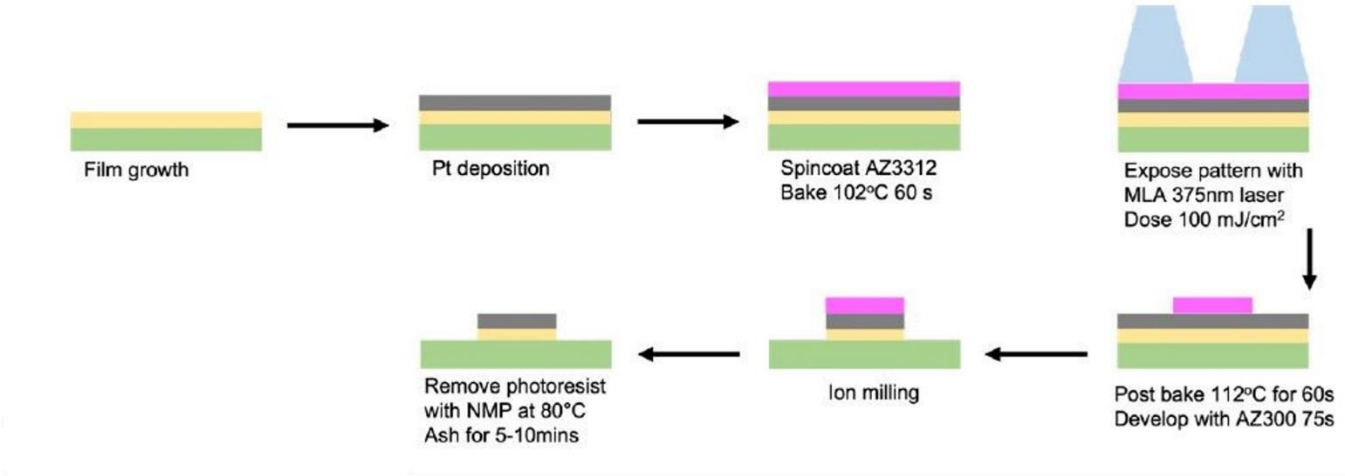

FIG. 3.7 Photolithography using MLA for fabrication of Hall crosses [79].

3.8 Magneto-optic Kerr effect (MOKE) microscopy

An Olympus microscope equipped with a polarizer and an analyzer was used to carry out the MOKE microscopy imaging. The original MOKE images were recorded by one AmScope camera, and the final images were obtained by subtracting the initial image from images obtained at different fields to enhance the contrast. A small electromagnet was installed under the microscope to apply perpendicular magnetic field to the films. In chapter 4 of this thesis, we present MOKE images for domain structure of a TbScIG thin film undergoing magnetization reversal. In chapter 5 of this thesis, we present MOKE images for domain structure of BiYIG films under equilibrium conditions (with zero net magnetization) and during magnetization reversal. We also use MOKE microscopy to observe bubble domain structure in a BiYIG|TmIG bilayer in chapter 6.

Chapter 4: Magnetism and Spin Transport in Platinum/Scandium-Substituted Terbium Iron Garnet Heterostructures

This work is adapted from a publication which the author wrote and published in Physical Review Materials [102]. *It is presented mostly in unaltered form.*

4.1 Introduction

Ferrimagnetic insulators (FMI) with perpendicular magnetic anisotropy (PMA) have attracted attention for spintronic applications such as racetrack memories [6] and magnetic random-access memories and for studies of spin orbit torque (SOT) [8] and chiral magnetic textures [103]. Electrical switching of magnetization of PMA FMI thin films via the damping-like component of SOT from a Pt overlayer has been demonstrated [8,67]. FMIs offer a number of advantages over ferromagnets (FMs) for memory applications including reduced ohmic losses due to elimination of parasitic current shunting, fast magnetization dynamics due to their low damping, and a more favorable scaling behavior because the PMA originates from the bulk and not the interface [23,67,104,105]. Transmission of electrical signals through Pt|FMI|Pt by spin-wave interconversion has been demonstrated [106] and a spin current from an FMI has been detected by the inverse spin-Hall effect (ISHE) in a Pt overlayer [107]. These developments indicate efficient transport of spin angular momentum across the FMI|Pt interface.

Yttrium iron garnet ($Y_3Fe_5O_{12}$, YIG) is among the most well studied FMIs [108–110]. It shows ultralow Gilbert damping and an extremely large magnon propagation length (several tens of mm) making it a suitable candidate for spin wave logic devices and signal transmitters [106,111]. There have been some reports of epitaxial [112–114] and polycrystalline YIG [115] thin films grown with PMA at low thickness by exploiting magnetoelastic anisotropy due to lattice mismatch and thermal mismatch with the substrate respectively. However, growth of high quality YIG thin films with high out-of-plane remanence remains a challenge. A variety of other FMI thin films have been grown with PMA including $CoFe_2O_4$ on $SrTiO_3$ and MgO substrates [116,117], barium hexaferrite ($BaFe_{12}O_{19}$) on sapphire substrates [67], Bi garnet

($Bi_3Fe_5O_{12}$) on $Gd_3Ga_5O_{12}$ (GGG) [118], BiYIG on substituted GGG [119] and rare earth iron garnets (REIG) on GGG or other garnet substrates. PMA may be obtained for appropriate combinations of magnetostriction and elastic strain, e.g. negative magnetostriction and in-plane tensile strain. Epitaxial REIG thin films grown with PMA by exploiting the lattice mismatch between the film and the substrate include $Dy_3Fe_5O_{12}$ (DyIG) [98], $Eu_3Fe_5O_{12}$ (EuIG) [120], $Sm_3Fe_5O_{12}$ (SmIG) [121], $Tb_3Fe_5O_{12}$ (TbIG) [120] and $Tm_3Fe_5O_{12}$ (TmIG) [8,100,122]. PMA has also been demonstrated in polycrystalline DyIG thin films grown on Si [98], EuIG thin films grown on quartz (0001) [99] and YIG thin films grown on amorphous quartz [123] by exploiting thermal mismatch between the film and the substrate.

Integration of REIG|heavy metal (HM) heterostructures into spin-based memory and logic devices requires efficient transport of spin angular momentum through the REIG|HM interface. Spin mixing conductance is the parameter that characterizes the transparency of an interface to the flow of spin angular momentum [8,100,120]. A number of studies have been performed to study the parameters that affect the spin mixing conductance of an interface. In general, a sharp and clean interface with good crystal perfection has been found to yield a high spin mixing conductance. For YIG|Pt the procedure used to clean the YIG surface prior to Pt deposition has a significant influence on spin mixing conductance of the interface [124]. In-situ Pt deposition results in higher spin mixing conductance for the $CoFe_2O_4$|Pt interface [116]. Substantial improvement in the spin mixing conductance of the YIG|Pt interface has been reported on insertion of a thin $Ni_{80}Fe_{20}$ layer and was attributed to enhanced magnetic moment density at the interface [125]. Spin mixing conductance for the $CoFe_2O_4$|Pt interface depends on the crystallographic orientation of $CoFe_2O_4$, in contrast to the EuIG|Pt interface for which spin mixing conductance was independent of EuIG orientation [116,120]. Introduction of a nano-scale amorphous layer prevents efficient spin transport through the YIG|Pt interface [126,127] and high temperature annealing caused a deterioration of the spin mixing conductance of the TmIG|Pt interface [128]. The anomalous Hall effect (AHE)-like spin-Hall magnetoresistance (SMR) in $Co_{1-x}Tb_x$ and TbIG undergoes a sign change on going

through the compensation temperature instead of going to zero [120,129]. This suggests that the spin mixing conductance in these materials scales with one of the magnetic sublattices and not the net magnetization. In REIG|Pt, the spin mixing conductance is similar for Y and various REs, suggesting that the Fe^{3+} plays the major role [120]. However, there has been no study so far to separate the contributions of the octahedral and tetrahedral Fe^{3+} ions to the spin mixing conductance of the REIG|Pt interface.

In this paper we report the structural, magnetic and spintronic properties of Sc substituted TbIG (TbScIG) thin films grown epitaxially on GGG substrates. Sc occupies exclusively octahedral sites in iron garnets [49,130–132] which are coupled antiparallel to the majority tetrahedral iron sites, and thus this study enables us to relate the net Fe^{3+} moment to the spin mixing conductance of the TbIG|Pt interface. We grew TbScIG thin films with varying Sc content up to $Tb_{2.8}Sc_{0.8}Fe_{4.4}O_{12}$ on (111) GGG substrates by pulsed laser deposition (PLD). Temperature-dependent vibrating sample magnetometry (VSM) measurements characterized the effect of Sc content on the magnetization and compensation temperature of TbScIG thin films, and AHE-like SMR measurements were performed on TbScIG|Pt heterostructures to determine the effect of Sc content on the spin mixing conductance of the interface. The key result is our finding of a significant increase in spin mixing conductance of the TbScIG|Pt interface with increasing Sc content. This is attributed to Sc diluting the octahedral Fe^{3+} thereby raising the density of uncompensated Fe^{3+}.

4.2 Structural and Magnetic Characterization

Targets with compositions of $Tb_3Fe_5O_{12}$ (T1) and $Tb_3Sc_{1.5}Fe_{3.5}O_{12}$ (T2) were prepared by solid state sintering. Thin film samples with composition S1 were deposited on (111) GGG substrate using only T1, and a series of TbScIG thin film samples were deposited on (111) GGG substrates by codeposition with the ratio of number of shots T1:T2 of 5:1 (S2), 2:1 (S3) and 1:1 (S4). Films prepared with higher Sc content than S4 were paramagnetic at room temperature. All the films were deposited at an oxygen partial pressure of 150 mTorr and a backside substrate temperature of 900 ºC. In this deposition chamber the

frontside substrate temperature is approximately 250 ºC lower than the backside substrate temperature according to an independent calibration. Further details of the deposition procedure are mentioned in the experimental section.

Rare earth iron garnets (REIGs, $RE_3Fe_5O_{12}$) belong to the Ia3d space group [133]. They have lattice parameters close to 1.2 nm which is similar to the lattice parameter of GGG, enabling epitaxial growth of REIG thin films on GGG substrates. Fig. 1(a) shows symmetric high resolution x-ray diffraction (HRXRD) scans around the GGG (444) peak for GGG (111)|TbScIG thin films with varying Sc content. Well defined Laue fringes in the HRXRD scans indicate high crystalline quality and thickness uniformity. Table I shows the d_{444} interplanar spacings calculated using the positions of the film peaks obtained from the HRXRD scans. The d_{444} spacing increased progressively from S1 to S4 which is consistent with the larger ionic radius of Sc^{3+} compared to that of Fe^{3+}, and with past studies performed on Sc-substituted bulk YIG and REIGs [130,131]. The spacing between the Laue fringes is inversely related to the epitaxial film thickness (Table I) [134].

Reciprocal space mapping (RSM) for the (642) reflection was performed on an S4 film with thickness of 94 nm as shown in Fig. 1(b). The film peak is vertically aligned with the substrate peak indicating that the film is fully strained in-plane to match the substrate lattice parameter, given by $d_{2\bar{2}0}^{S4} = d_{2\bar{2}0}^{GGG} = q_x^{-1} = 0.4375$ nm. This gives the cubic lattice parameter of GGG, $a_{GGG} = 2\sqrt{2}\, d_{2\bar{2}0}^{GGG} = 1.2376$ nm which agrees very well with its literature value [100]. Rosenberg et al. performed similar RSM measurements on GGG(111)|TbIG and found the films to be lattice matched to the substrate up to thickness of 90 nm [120]. Since the films used here for magnetometry and spintronics characterization have thickness lower than 90 nm we assume that they are lattice matched to the substrate over the entire range of composition (S1 to S4).

Atomic force microscopy (AFM) was performed on film S2 to characterize surface topography (Fig. 1(c)). The RMS surface roughness was less than 0.3 nm. We tried to observe the domain structure of an ac demagnetized film S2 using magnetic force microscopy (MFM). However, the low coercivity and low magnetization of S2 at room temperature yielded little magnetic contrast. In-situ observations were made on magnetization switching in S2 using a magneto-optical Kerr effect (MOKE) microscope. Fig. 1(d) shows domain wall motion and expansion of reversed domains during magnetization switching in S2.

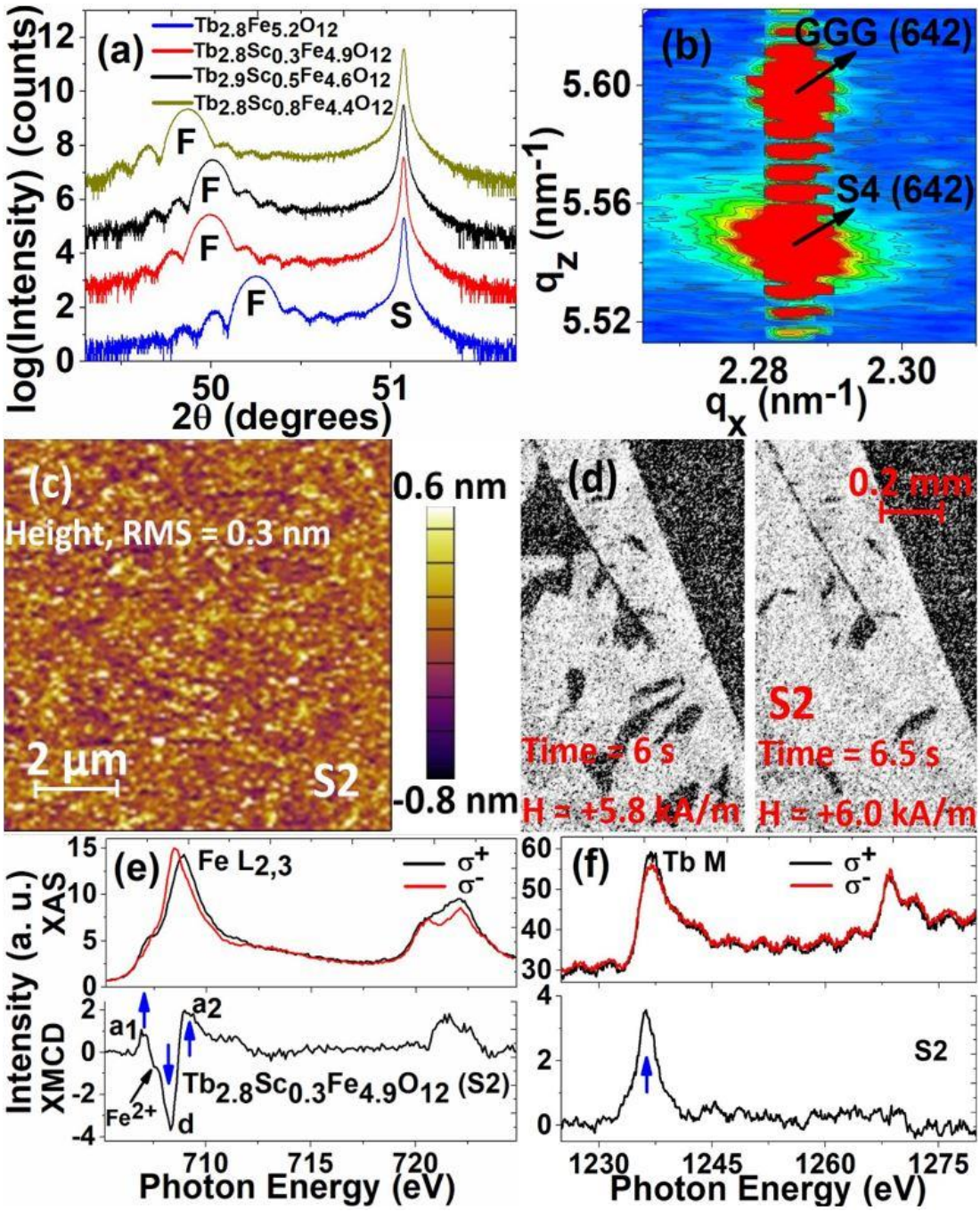

FIG. 4.1 (a) High-resolution XRD scans of GGG|TbScIG thin films with varying Sc content (vertically offset for clarity with film and substrate peaks labeled F and S respectively) (b) High-resolution XRD reciprocal space map of GGG|$Tb_{2.8}Sc_{0.8}Fe_{4.4}O_{12}$ film with thickness 94 nm (c) Topographic image from an AFM scan on 67 nm thick $Tb_{2.8}Sc_{0.3}Fe_{4.9}O_{12}$ film (S2). The RMS surface roughness is less than 0.3 nm (d) MOKE images showing domain wall motion during magnetization switching in S2 (e), (f) XAS and XMCD intensity signals for Fe L edge and Tb M edge for S2. Arrows in lower panel show magnetization directions at respective energy peaks pointing up (down) for positive (negative) XMCD signal.

X-ray absorption spectra (XAS) were measured on S2 at room temperature and the resulting magnetic circular dichroism (XMCD) revealed the magnetization of the different sublattices (Fig. 1(e) and 1(f)) [135]. XAS for the two helicities of X-rays were obtained by normalizing the respective total fluorescence yields (TFY) by the intensities of the incident X-rays for the Fe L-edge, Tb M-edge and O K-edge. The XMCD signal was obtained as the difference between XAS intensities for two helicities. Clearly the XAS signal for the Fe L-edge and Tb M-edge is dichroic at room temperature. The alternating positive and negative peaks in the Fe L_3 edge of XMCD correspond to contributions of octahedral Fe^{3+} and tetrahedral Fe^{3+} respectively, indicating antiferromagnetic alignment of the octahedral (a) sublattice and tetrahedral (d) sublattices as is typical in iron garnets [100]. Further, the Tb M-edge of XMCD indicates antiferromagnetic alignment of the dodecahedral (c) sublattice and d sublattice as expected [100]. The presence of a shoulder peak close to the d site peak in the Fe L_3 edge of XMCD indicates the presence of Fe^{2+} similar to observations of Vasili et al. for Ce-YIG [136].

To facilitate accurate determination of composition for our samples, TbIG and TbScIG films with much higher thickness (>200 nm) but the same ratio of shots from the two targets (T1:T2) were analysed by wavelength dispersive spectroscopy (WDS). The raw intensity ratio data was processed using the GMRFILM program [81] yielding compositions of $Tb_{2.8}Fe_{5.2}O_{12}$ (S1), $Tb_{2.8}Sc_{0.3}Fe_{4.9}O_{12}$ (S2), $Tb_{2.9}Sc_{0.5}Fe_{4.6}O_{12}$ (S3) and $Tb_{2.8}Sc_{0.8}Fe_{4.4}O_{12}$ (S4). X-ray photoelectron spectroscopy (XPS) measurements were performed on thinner S1, S2, S3 and S4 films (< 90 nm thickness) to obtain qualitative information about their compositions. High-resolution XPS spectra of the Tb 4d, Sc 2p and Fe 2p peaks shown in Fig. 4.2 indicate that the Sc peaks become progressively more prominent while Fe peaks become weaker as we move from S1 to S4, which agrees with the WDS results. All the films were Tb-deficient (Tb:(Fe+Sc) = 0.54-0.57), in contrast to previous studies on TbIG and EuIG films which were rare earth rich [120]. The difference is attributed to changes in the laser optics and fluence compared to the earlier work.

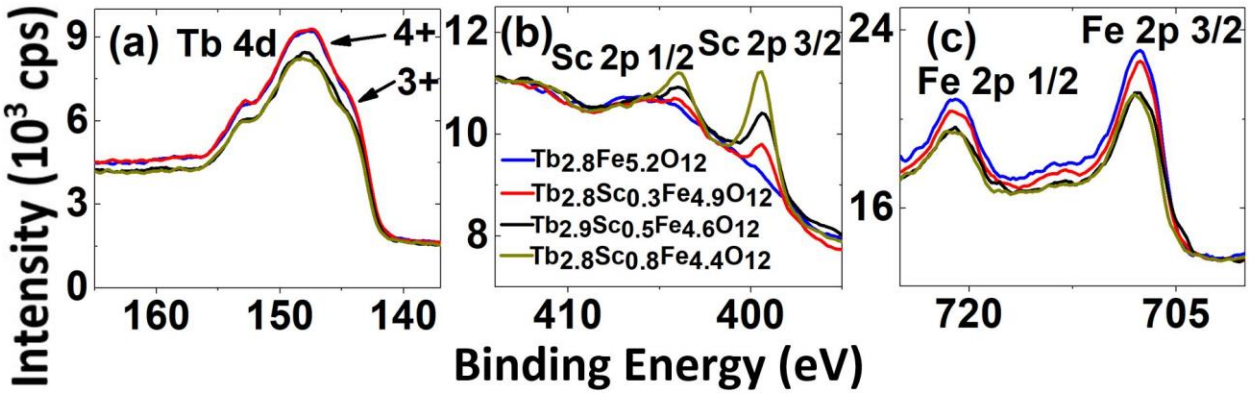

FIG. 4.2 Tb 4d, Sc 2p and Fe 2p XPS spectra of representative TbScIG thin films with varying Sc content. Oxidation states of Tb are marked in Tb 4d spectra.

Despite the Tb deficiency in our films, XRD did not indicate the presence of any non-garnet phase. XPS scans for Tb 4d indicate the presence of Tb^{4+} (a more stable $4f^7$ ion compared to Tb^{3+}, $4f^8$) in addition to Tb^{3+}, similar to observations of Fakhrul et al. for TbIG [137]. Charge neutrality is maintained by the presence of Fe^{2+} and likely cation vacancies, discussed below. XPS was unable to resolve oxidation states of Fe.

The magnetic anisotropy of the films includes several contributions of different origin – shape anisotropy, magnetocrystalline anisotropy, magnetoelastic anisotropy and growth-induced anisotropy. The anisotropy constant K_u is defined as the difference between magnetic energy for magnetization oriented in-plane and out-of-plane. For epitaxial films lattice-matched to the GGG (111) substrate, K_u is given by [98]:

$$K_u = E_{IP} - E_{OOP} = \frac{-K_1}{12} - \frac{\mu_0}{2} M_s^2 + \frac{9}{4} c_{44} \lambda_{111} \left(\frac{\pi}{2} - \beta\right) + K_G \qquad (4.1)$$

A positive (negative) K_u corresponds to an out-of-plane (in-plane) easy axis. The first term on the right side of equation (1) represents the magnetocrystalline anisotropy. K_1 is the first order cubic magnetocrystalline anisotropy constant and has small negative values for REIGs thus favoring PMA [138]. However, its contribution is small compared to other terms and will be neglected here. The second term represents the shape anisotropy and favors in-plane magnetization. The third term represents

the magnetoelastic anisotropy K_{me} and is proportional to both magnetostriction λ_{111} and shear strain which is half the difference between $\pi/2$ and the corner angle of the rhombohedrally distorted unit cell β. c_{44} is the shear modulus of the film and lies between 74 and 90 GPa for REIGs [138]. For films with positive (negative) λ_{111} and compressive (tensile) strain magnetoelastic anisotropy favors PMA. K_G represents a uniaxial growth-induced anisotropy, as has been reported in Fe-deficient YIG [139,140] or in garnets with mixed dodecahedral cations such as $(Tm,Y)_3Fe_5O_{12}$ [141]. K_G originates from preferential occupancy of cations or vacancies in nonequivalent sites. Both magnetoelastic and growth-induced anisotropies are uniaxial and may be combined into a uniaxial term $K_{me} + K_G$.

Symmetric HRXRD scans (Fig. 1(a)) show that all the films grow with in-plane compressive strain due to lattice mismatch with GGG. The bulk magnetostriction value λ_{111} of TbIG is 12×10^{-6} [138] favoring PMA for epitaxial films with sufficiently large in-plane compressive strain. The out-of-plane VSM hysteresis loops in Fig. 3 indeed show PMA and high remanence at room temperature with the exception of S1, which has a sheared loop without a clear saturation. This is a result of a near room temperature compensation temperature [120], to be discussed below. The out-of-plane hysteresis loops for S1 at temperatures away from the compensation temperature ($\leq$ -40 ºC and $\geq$ 50 ºC) indicate PMA. The S4 films retain PMA up to a thickness of 94 nm. None of the films (S1-S4) showed a clear in-plane saturation for magnetic field up to 120 kA/m, and the large non-linear signal from the paramagnetic GGG substrate prevented determination of the anisotropy fields of these films. The value 120 kA/m was taken as a lower bound for the anisotropy field H_K.

Room temperature saturation magnetization (M_s) obtained from out-of-plane hysteresis loops are displayed in Table I, and increase with increasing Sc content. The magnetic moment of REIGs above the compensation temperature is given by the magnetic moment of the tetrahedral sublattice minus the sum of the magnetic moments of octahedral and dodecahedral sublattices [131]. Sc^{3+} has a larger ionic radius than Fe^{3+} and is known to occupy exclusively the octahedral sites thus weakening the octahedral sublattice

moment [49,130–132]. Sc substitution lowers the compensation temperature and Curie temperature, as reported for Sc-substituted GdIG and (Gd,Y)IG [131], and raises the room temperature magnetization as the compensation temperature decreases below room temperature.

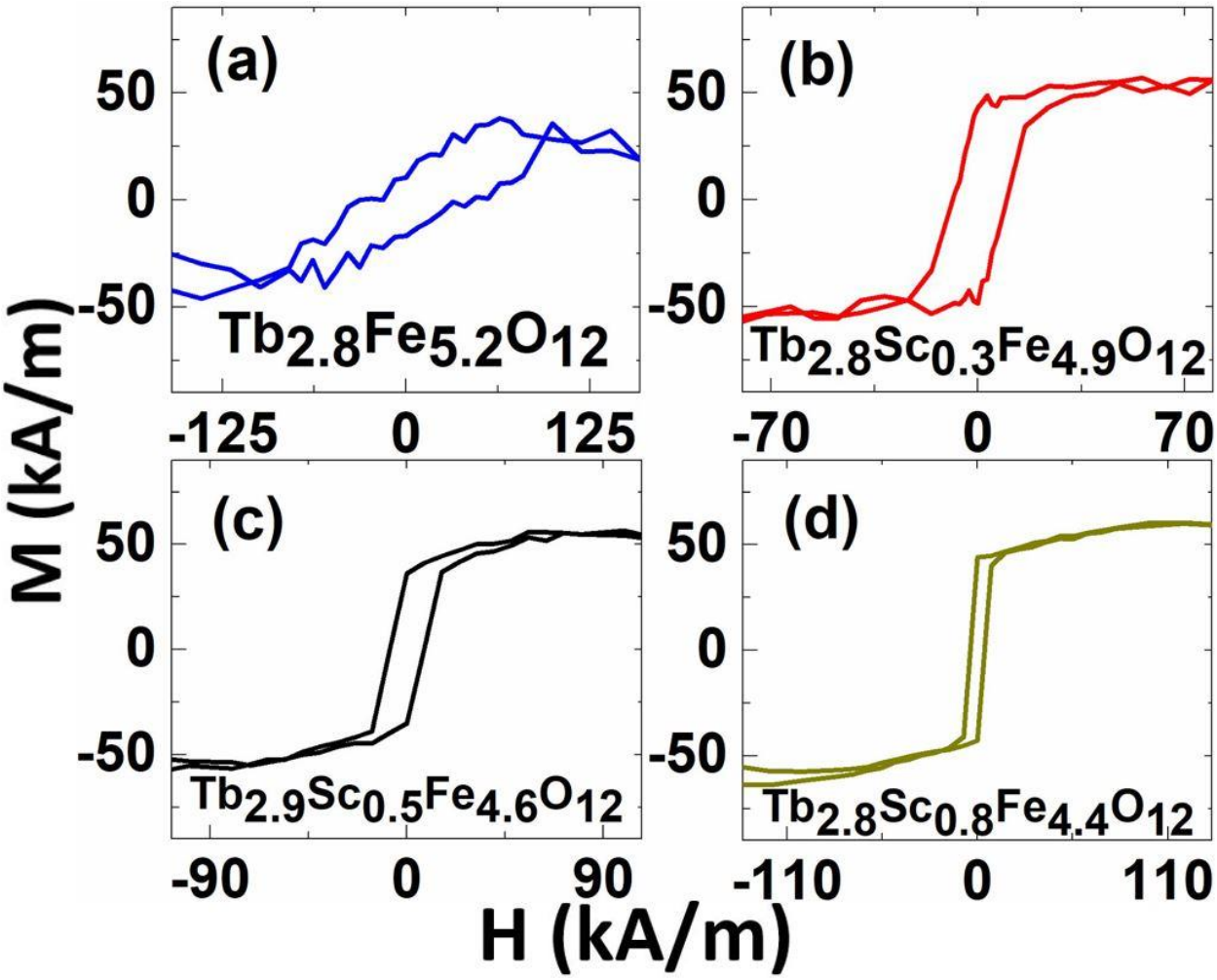

FIG. 4.3 Room temperature out-of-plane VSM hysteresis loops of representative GGG|TbScIG thin films with varying Sc content.

We can use lower bounds for the anisotropy fields of films along with strain calculated from HRXRD scans to obtain lower bounds for magnetostriction values λ_{111} using equation (1). Due to lattice mismatch with the substrate, the unit cell of the film is distorted from cubic to rhombohedral. We have used a rhombohedral to hexagonal transformation to simplify the calculation of strain [142]. The transformation from rhombohedral (hkl) to hexagonal (HKL) miller indices is given by:

$$H = h - k, \qquad K = k - l, \qquad L = h + k + l \qquad (4.2)$$

The in-plane lattice parameter a_H and the lattice parameter c of the hexagonal unit cell are given by:

$$a_H = \sqrt{12 d_{11\bar{2}}^2}, \qquad c = 12\, d_{444} \qquad (4.3)$$

Here $d_{11\bar{2}}$ is the $(11\bar{2})$ interplanar spacing of the rhombohedrally distorted unit cell of the film which is assumed to be equal to the $(11\bar{2})$ interplanar spacing of the GGG substrate and d_{444} is the (444) interplanar spacing of the film extracted from HRXRD scans (Fig. 1(a)). Finally the lattice parameter a_R and corner angle β of rhombohedrally distorted unit cell are given by:

$$a_R = \frac{1}{3}\sqrt{3\, a_H^2 + c^2} \qquad \sin\left(\frac{\beta}{2}\right) = \frac{3}{2\sqrt{3 + \left(\frac{c}{a_H}\right)^2}} \qquad (4.4)$$

Calculated β values for all the films (S1-S4) are displayed in Table I. Bulk TbIG has a K_1 value close to -820 J/m^3 [138]. Thus, the contribution of magnetocrystalline anisotropy in equation (1) is much smaller than other terms and can be ignored for our calculations. Inserting the shear modulus for TbIG [138] and β, M_s and the lower bounds for overall anisotropy K_u in equation (1) we have obtained lower bounds for the magnetostriction λ_{111} displayed in Table I, on the basis of $K_G = 0$. A nonzero K_G, favoring PMA, would have the result of reducing the lower bound of λ_{111} even further. The lower bound values are well below the bulk magnetostriction [120].

The volume of the rhombohedral unit cell V_R is calculated as [142]:

$$V_R = a_R^3 \sqrt{1 - 3\cos^2\beta + 2\cos^3\beta} \qquad (4.5)$$

Calculated values of V_R displayed in Table I are close to the literature value of the unit cell volume for bulk TbIG [120]. The unit cell volume in our films increases with increasing Sc content which is consistent with the larger ionic radius of Sc^{3+} compared to Fe^{3+} [130].

4.3 Spintronic Properties

We performed electrical measurements on Hall crosses patterned from Pt/TbScIG/GGG to determine the effect of Sc content on the spin mixing conductance of the TbScIG|Pt interface and investigate the role of the iron sublattice in interfacial spin mixing of REIG|HM interfaces. Heavy metals such as Pt and Ta exhibit a strong spin-orbit interaction which enables efficient conversion of charge current to spin current and vice versa [94]. Flow of charge current through the HM layer produces a spin current perpendicular to the HM layer due to the spin-Hall effect (SHE). Reflection/absorption of this spin current at the FMI|HM interface depends on the relative orientation of polarization of the spin current and the magnetization of the FMI (m). The reflected spin current can produce a charge current by the inverse spin-Hall effect (ISHE) which modulates the longitudinal resistance of the HM layer. The resultant magnetoresistance for the FMI|HM bilayer is the spin-Hall magnetoresistance (SMR) [95].

Spin mixing conductance parameterizes the transparency of the FMI|HM interface to the flow of spin current through it [95], and it is crucial for a variety of spintronics phenomenon including spin pumping [96], spin-orbit torque (SOT) [97] and SMR. SMR measurements have been extensively used to obtain spin mixing conductance of REIG|HM interfaces [98–100]. The additional contribution to longitudinal resistance due to SMR has the symmetry $\Delta R^{SMR} \propto m_y^2$ assuming current flow in the HM layer along the x direction and normal to the film plane along the z direction. There is also a transverse component of SMR with symmetry $R_H^{SMR} \propto m_x m_y$. In addition to this the imaginary component of spin mixing conductance gives rise to an anomalous Hall effect (AHE)-like SMR contribution (much smaller than R_H^{SMR}) with symmetry $R_H^{AHE,SMR} \propto m_z$. Combining the above contributions with the ordinary Hall effect (OHE) of the HM layer we can write the transverse Hall resistance R_H as:

$$R_H = R_H^{SMR} sin^2\theta \; sin(2\phi) + R_H^{AHE,SMR} cos\;\theta + R_H^{OHE} H_z \qquad (4.6)$$

Here θ and φ are the polar and azimuthal angles of m respectively and R_H^{OHE} is the ordinary Hall effect of the HM layer due to magnetic field H_z.

TbScIG films (S1, S3 and S4) with thickness 60 nm were coated with 4 nm thick Pt overlayers by sputtering. The TbScIG|Pt heterostructures were patterned into Hall cross devices (optical micrograph is shown in Fig. 4(c)) by photolithography followed by ion milling. A standard lock-in technique was used to obtain AHE-like SMR hysteresis loops. These loops are shown in Fig. 4(a) and 4(b) after subtraction of sample dependent offsets and a linear contribution from OHE of Pt. The coercivities obtained from

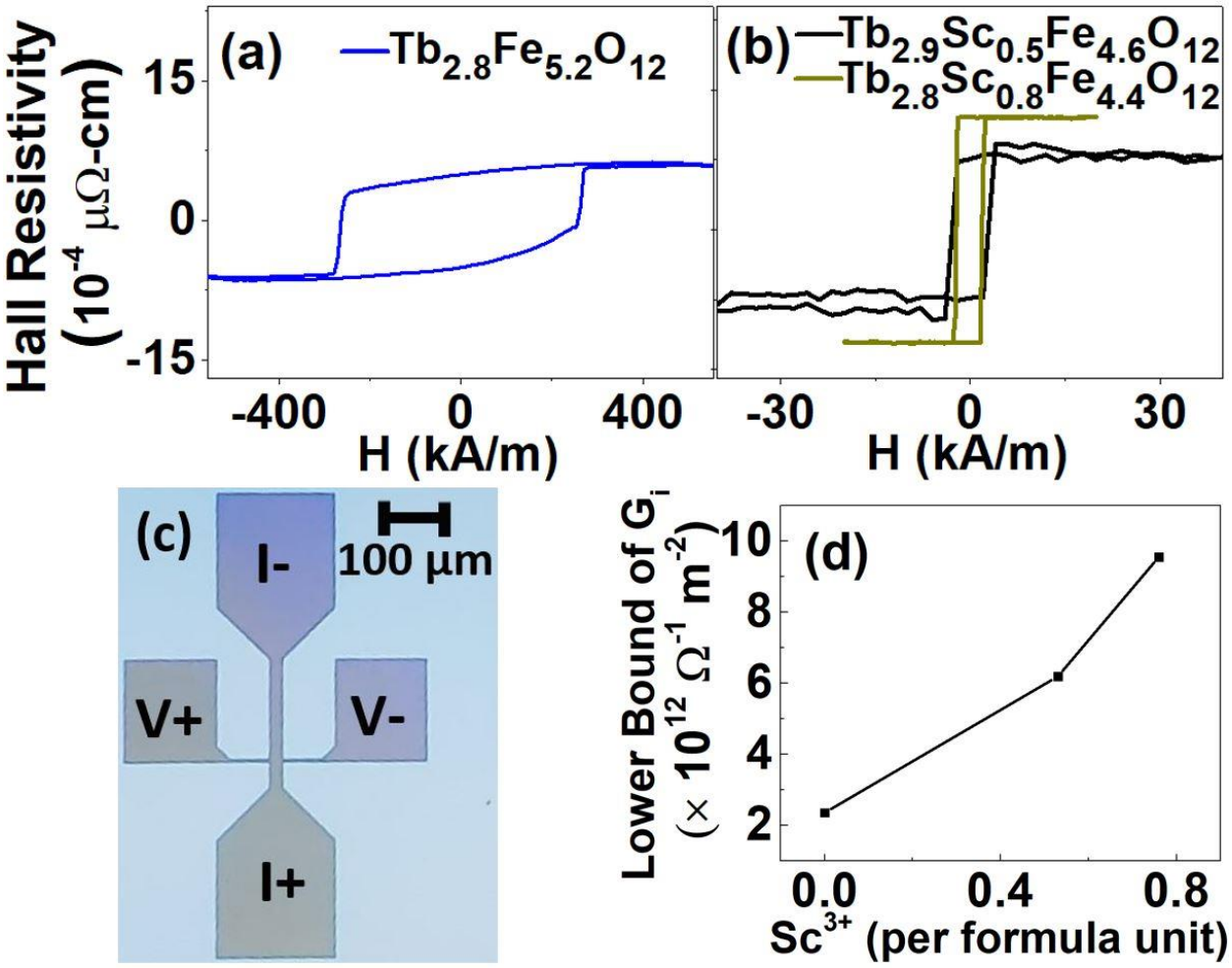

FIG. 4.4 (a) and (b) AHE-like SMR hysteresis loops for TbScIG(60 nm)|Pt(4 nm) heterostructures. (c) Optical micrograph of a representative Hall cross used for measurement. (d) Lower bound of imaginary component of spin mixing conductance versus number of Sc^{3+} ions per formula unit.

these loops are shown in Table II. Differences in coercivities obtained from AHE-like SMR hysteresis loops and VSM hysteresis loops may be attributed to geometrical effects associated with patterning and differences in the thickness of the films [8,120]. The AHE-like SMR hysteresis loop for S1 is sheared similar to its room temperature VSM hysteresis loop, which is attributed to the near-room temperature compensation temperature (discussed later). AHE-like SMR hysteresis loops for S3 and S4 show 100% remanence and sharp switching. We were not able to saturate the films in-plane up to a magnetic field of 600 kA/m.

The model of Chen et al. [95] for spin mixing conductance gives the following relations:

$$\frac{\rho_{xy}^{SMR}}{\rho_{xx}^{Pt}} = \frac{\theta_{SH}^2 \lambda_{Pt}}{d_N} \frac{2\lambda_{Pt} G_r \tanh^2 \frac{d_N}{2\lambda_{Pt}}}{\sigma_{xx}^{Pt} + 2\lambda_{Pt} G_r \coth \frac{d_N}{2\lambda_{Pt}}} \qquad (4.7)$$

$$\frac{\rho_{xy}^{AHE,SMR}}{\rho_{xx}^{Pt}} = \frac{2\theta_{SH}^2 \lambda_{Pt}^2}{d_N} \frac{\sigma_{xx}^{Pt} G_i \tanh^2 \frac{d_N}{2\lambda_{Pt}}}{(\sigma_{xx}^{Pt} + 2\lambda_{Pt} G_r \coth \frac{d_N}{\lambda_{Pt}})^2} \qquad (4.8)$$

Here θ_{SH} is the spin-Hall angle of Pt, λ_{Pt} is the spin diffusion length of Pt, d_N is the thickness of the Pt overlayer, ρ_{xx}^{Pt} is the resistivity of Pt obtained from longitudinal resistance measurement on the Hall bar device, ρ_{xy}^{SMR} and $\rho_{xy}^{AHE,SMR}$ are Hall resistivities corresponding to SMR and AHE-like SMR respectively and G_r and G_i are real and imaginary components of spin mixing conductance respectively. Without being able to saturate the films in-plane we could not determine ρ_{xy}^{SMR} and G_r. However, dropping G_r in the denominator in equation (8) and inserting $\rho_{xy}^{AHE,SMR}$ amplitudes from Fig. 4(a) and 4(b), d_N = 4 nm, θ_{SH} = 0.08 and λ_{Pt} = 1.4 nm [100] we have obtained lower bounds of G_i shown in Fig. 4(d) and Table II.

The lower bound of G_i obtained for the S1(TbIG)|Pt interface is of the same order of magnitude as those obtained for REIG|Pt interfaces in past studies [120]. However, nonmagnetic Sc^{3+} substitution on octahedral sites is accompanied by a significant enhancement in the lower bound of G_i as shown in Fig 4(d), and the lower bound of G_i obtained for S4|Pt is higher than those reported for TmIG|Pt, EuIG|Pt and

TbIG|Pt in past studies [100,120]. The net magnetic moment of the iron sublattice in iron garnets is given by the difference between the magnetic moment of the tetrahedral and octahedral sublattices [131], and therefore increases with Sc^{3+} substitution on octahedral sites. These observations indicate a correlation between the spin mixing conductance of substituted REIG|Pt interfaces and the magnetic moment of the iron sublattice.

4.4 Temperature-Dependent Magnetization of TbScIG Films

Temperature dependent VSM measurements on all films (S1-S4) show the effect of Sc content on the Curie temperature (T_{Curie}) and compensation temperature (T_{comp}) (Fig. 5). T_{Curie}, T_{comp} and room temperature M_s and coercivity for all films are displayed in Table II. T_{Curie} decreases with increasing Sc content which is attributed to a decrease in the number of Fe^{3+}(a)-O^{2-}-Fe^{3+}(d) antiferromagnetic exchange interactions per formula unit due to Sc substitution on the octahedral (a) sites. T_{comp} decreases with increasing Sc content, a result of the lower moment of the octahedral and dodecahedral sublattices relative to the magnetic moment of the tetrahedral sublattice. These observations are consistent with past studies on nonmagnetic substitution in bulk YIG and REIGs [130,131]. The room temperature coercivity decreases with increasing Sc content (see Table II). The film with the lowest Sc content (S1: TbIG) is close to its T_{comp} at room temperature and has a high coercivity while the film with the highest Sc content (S4) is furthest away from T_{comp} at room temperature and has lowest coercivity, consistent with the results of Rosenberg et al. for the temperature-dependent coercivity of TbIG [120].

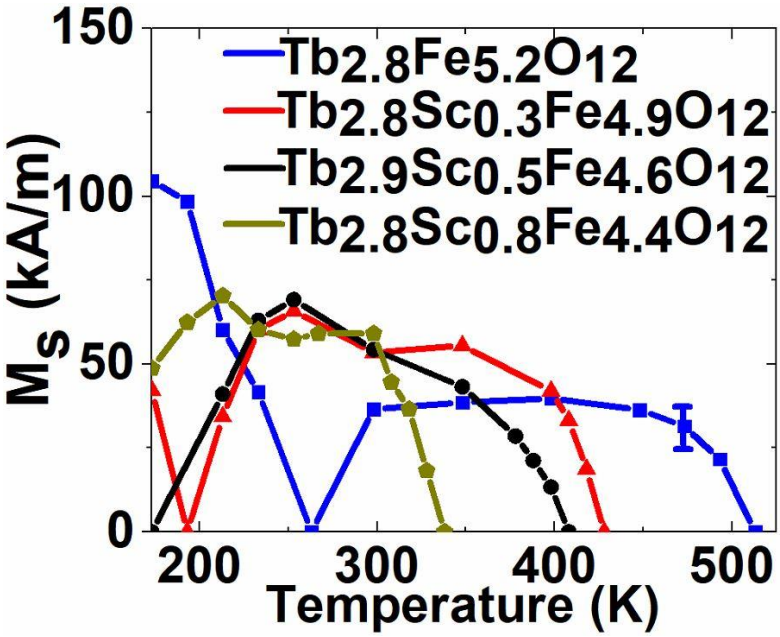

FIG. 4.5 Magnetic moment versus temperature for GGG|TbScIG thin films with varying Sc content. A typical error bar is attached.

A model based on the molecular field coefficient theory of Dionne [53,143] and others was developed to compare with the experimental data. This model accounts for nonmagnetic substitution on the iron sublattices by reduction of the values of molecular field coefficient according to empirically determined relationships. The off-stoichiometry (Tb:(Fe+Sc) < 0.6) is incorporated into the model by assuming that the excess Fe^{3+} occupies the dodecahedral sublattice, and couples ferromagnetically to the dodecahedral rare-earth ions. It is assumed that the molecular field coefficients do not change in the composition range studied here and we neglect the presence of cation vacancies. Fig. 6(a) shows magnetization versus temperature plots produced by the model for the compositions determined by WDS. There is a clear decrease in compensation temperature with increasing Sc content as shown in Table II, corresponding qualitatively to the experimental values.

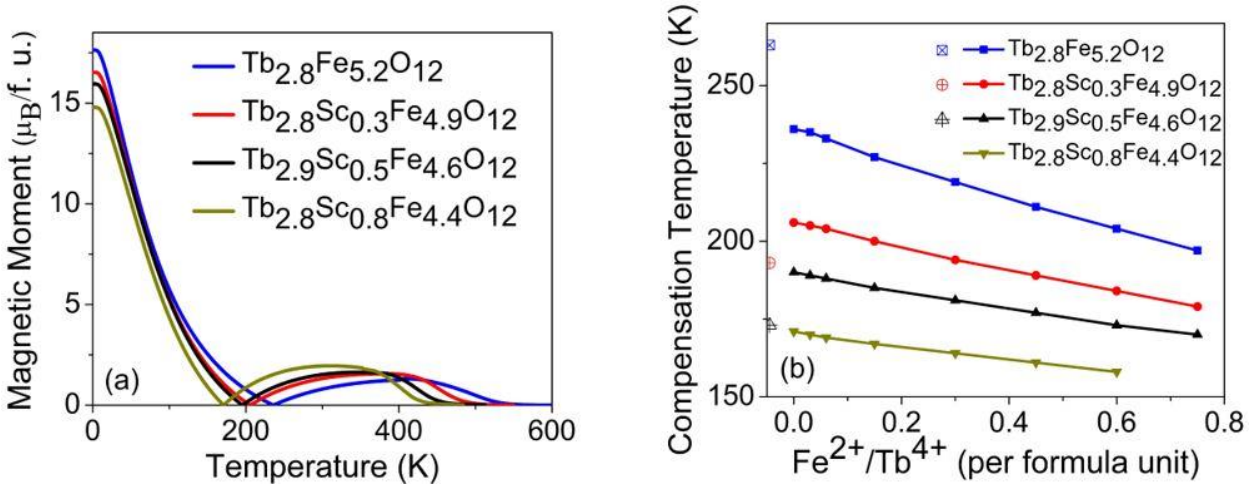

FIG. 4.6 (a) Magnetic moment per formula unit versus temperature for TbScIG obtained from molecular field coefficient (MFC) model (b) Compensation temperature versus number of $Fe^{2+}$and Tb^{4+} ions per formula unit in MFC model.

The Curie temperature was estimated as the temperature at which magnetization becomes lower than a value of 0.1 μ_B per formula unit (displayed in Table II). The magnetization approaches zero asymptotically in the model, in contrast to experimental observations, but the threshold selected gives a reasonable value of the Curie temperature when the model is applied to YIG. Both model and experiment show a fall in T_{Curie} with increasing Sc, with the model values higher than the experiment.

The model was modified to account for the presence of Tb^{4+} by assuming that there are equal amounts of Fe^{2+} and Tb^{4+} to ensure charge balance, and that the Fe^{2+} preferentially occupies the dodecahedral sites due to its larger ionic radius. The results are shown in Fig. 6(b). This indicates that including equal amounts of Fe^{2+} and Tb^{4+} lowers the calculated T_{comp}, which is already lower than the experimental value for S1, suggesting a more complex defect distribution than that encompassed by the model. The small Fe^{2+} peak in XMCD (Fig. 1e) and the large Tb^{4+} peak (Fig. 2a) suggest that the amount of Fe^{2+} does not balance the Tb^{4+} and therefore additional defects are required to balance the charge. Fe vacancies, which could be present on either octahedral or tetrahedral sites, or Tb vacancies on the dodecahedral sites may be present, although first principles calculations in YIG indicate that cation vacancies have higher formation energies

than antisite defects [144]. The non-ideality of the site occupancy accounts for the higher than bulk compensation temperature of the S1 composition, and will be described in detail elsewhere [37].

Table 4.1: Results of structural and magnetic characterization of representative GGG|TbScIG thin films. Calc. = calculated, Lit. = literature, NA = not available.

Material	β (deg.)	d_{444} (nm)	Thickness (nm)	H_K (kA/m)	M_S (kA/m) (±7)	$\lambda_{111}(10^{-6})$ (Calc.)	$\lambda_{111}(10^{-6})$ (Lit.)	$V_{cell}(nm^3)$ (Calc.)	$V_{cell}(nm^3)$ (Lit.)
$Tb_{2.8}Fe_{5.2}O_{12}$	89.42	0.1814	63	>120	37	>1.8	12	1.926	1.92
$Tb_{2.8}Sc_{0.3}Fe_{4.9}O_{12}$	89.23	0.1823	67	>120	53	>2.3	NA	1.935	NA
$Tb_{2.9}Sc_{0.5}Fe_{4.6}O_{12}$	89.24	0.1822	73	>120	54	>2.3	NA	1.934	NA
$Tb_{2.8}Sc_{0.8}Fe_{4.4}O_{12}$	89.14	0.1827	66	>120	59	>2.3	NA	1.939	NA

Table 4.2: Comparison of magnetic and spintronic properties of TbScIG thin films. Exp. = experimental, Calc. = calculated, NA = not available.

Material	300 K M_S (±7) (kA/m) (Exp.)	300 K M_S (kA/m) (Calc.)	T_{comp} (K) (±10) (Exp.)	T_{comp} (K) (Calc.)	T_{Curie} (K) (±10) (Exp.)	T_{Curie} (K) (Calc.)	Coercivity (kA/m) (±1) (from VSM)	Coercivity (kA/m) (from SMR)	Lower bound of G_i ($10^{12}\ \Omega^{-1}\ m^{-2}$)
$Tb_{2.8}Fe_{5.2}O_{12}$	37	30.7	263	236	503	537	35	259 ± 4	2.4
$Tb_{2.8}Sc_{0.3}Fe_{4.9}O_{12}$	53	51.0	193	206	423	497	9	NA	NA
$Tb_{2.9}Sc_{0.5}Fe_{4.6}O_{12}$	54	58.7	173	195	403	460	8	3.0 ± 0.2	6.2
$Tb_{2.8}Sc_{0.8}Fe_{4.4}O_{12}$	59	73.7	<173	171	333	435	4	2.1 ± 0.2	9.6

4.5 Conclusion

The effect of Sc substitution on the magnetic properties of TbIG films is investigated, in particular the effect on the spin mixing conductance of the Pt|garnet interface. The films have (111) orientations with high epitaxial quality and perpendicular magnetic anisotropy, originating from magnetoelastic anisotropy with possible growth-induced contribution. Up to 40% of the octahedral Fe is replaced by Sc. There is a Tb deficiency with Tb:(Fe+Sc) = 0.54-0.57. Tb is present as both Tb^{3+} and Tb^{4+}, and there is some Fe^{2+} present.

Sc substitutes onto the octahedral Fe sites, raising the net magnetic moment of the (octahedral + tetrahedral) sublattices and lowering the compensation temperature. The dilution of octahedral Fe also

lowers the number of antiferromagnetic Fe^{3+}-O^{2-}-Fe^{3+} interactions per formula unit and reduces the Curie temperature. These results agree qualitatively with the temperature dependence of magnetic moment obtained from molecular field coefficient modelling of TbScIG with varying Sc content.

The most significant finding is the substantial increase (by a factor of ~4) of the imaginary part of the spin mixing conductance on increasing the Sc content. The increase in G_i is correlated to the increase in the net Fe magnetization, suggesting that the spin transport across the interface and the consequent SMR is strongly dependent on the Fe sublattice magnetization. This is consistent with prior results showing that SMR changes sign at the compensation temperature instead of going to zero. This result provides a path to enhance spin mixing conductance and SMR through stoichiometry control of garnets.

4.6 Methods

Thin Film Deposition and Characterization. Pulsed laser deposition (PLD) was used for deposition of thin films on (111) gadolinium gallium garnet (GGG) substrates. Mixed oxide sintering of Tb_2O_3 and Fe_2O_3 powders was used to prepare $Tb_3Fe_5O_{12}$ target. Similarly, mixed oxide sintering of Tb_4O_7, Fe_2O_3 and Sc_2O_3 powders was used to prepare a $Tb_3Sc_{1.5}Fe_{3.5}O_{12}$ target. Conditions during the deposition were a laser fluence of 2.0 J/cm^2, backside substrate temperature of 900 ^oC, laser repetition rate of 10 Hz and oxygen partial pressure of 150 mTorr. After the deposition films were cooled down to room temperature at a rate of 20 ^oC/min in oxygen partial pressure of 150 mTorr. High resolution x-ray diffraction (HRXRD) measurements were performed using a Bruker D8 Discover HRXRD. AFM model Cypher S was used to obtain topographical images of film surface. An Olympus microscope equipped with a polarizer and an analyzer was used to carry out the MOKE microscopy imaging. The original MOKE images were recorded by one AmScope camera and the final images are obtained by subtracting the initial image from images obtained at different fields to enhance the contrast. A small electromagnet was installed under the microscope to apply perpendicular magnetic field to the films. Element-specific magnetic structure of TbScIG film was investigated using XMCD at Argonne National Laboratory, USA. XAS data was

collected for Tb M and Fe L absorption edges using TFY measurements. Magnetic measurements were performed using an ADE 1660 VSM.

Compositional Characterization. High-resolution XPS spectra was taken using a Physical Electronics VersaProbe II for films with thickness less than 90 nm used for magnetometry. Adventitious carbon on the sample surface was removed by a cleaning procedure using an argon ion beam prior to acquiring data. A pass energy of 23.5 eV was used to acquire data. WDS measurements were performed on garnet films with thickness greater than 200 nm using a JEOL JXA-8200 electron probe microanalyzer with an accelerating voltage of 15 kV and a beam current of 10 nA and the data was reduced with the GMRFILM software package for thin film analysis.

Hall Cross Fabrication and Spintronic Measurements. Hall crosses of dimensions 200 μm × 20 μm were fabricated by photolithography. Negative images were created on garnet films with sputtered platinum overlayers and ion milling was used to form mesa structures. Residual photoresist was removed by dissolution in acetone. Spintronic measurements were performed on Hall crosses using a home-made four-point probe.

Contributors to this paper:

MOKE measurements were performed by Yabin Fan. XPS measurements were performed by Libby Shaw. SMR measurements were performed by Pengxiang Zhang. Molecular field coefficient modeling was performed by Jackson Bauer.

Chapter 5: Substrate-Dependent Anisotropy and Damping in Epitaxial Bismuth Yttrium Iron Garnet Thin Films

This work is adapted from a publication to which the author contributed multiple sections and published in Advanced Materials Interfaces [29]. *It is presented mostly in unaltered form.*

5.1 Introduction

Iron garnets are ferrimagnetic insulators with composition $A_3Fe_5O_{12}$, where the dodecahedral A-sites are occupied by a rare earth (RE), Y, Bi, and so on. Films of many iron garnets such as $Tm_3Fe_5O_{12}$ can be grown with PMA as a result of magnetoelastic anisotropy [70,100,145], which is useful in a range of spintronic device applications [146]. Iron garnets also exhibit fast magnetization dynamics due to their low Gilbert damping (α). Yttrium iron garnet (YIG) has the lowest damping among known magnetic materials [28,147], and all the RE iron garnets (REIGs) exhibit larger values [99,148]. For bulk YIG, values of α as low as 10^{-5} have been reported, whereas for thin films of YIG, $\alpha = 6 \times 10^{-5}$ in the best case [108] and commonly $\alpha = (1–2) \times 10^{-4}$, as summarized in ref. [149]. The ferromagnetic resonance (FMR) full width at half maximum linewidth (FWHM) of YIG films is $\mu_0\Delta H_0 = (0.4–0.6)$ mT [149]. A combination of PMA and low α is advantageous, but it is challenging to grow YIG thin films with PMA. PMA YIG films have been obtained by the use of buffer layers of $Sm_3Ga_5O_{12}$ [112] or by growth on gadolinium scandium gallium garnet substrates ($Gd_3Sc_2Ga_3O_{12}$) to increase magnetoelastic anisotropy [150]. The latter experiment yielded $\alpha = (4–11) \times 10^{-4}$ and FWHM $\mu_0\Delta H_0 = (1$ to $4)$ mT measured in an out-of-plane field.

Bismuth-substituted yttrium iron garnet (BiYIG, $Bi_xY_{3-x}Fe_5O_{12}$) combines PMA and a moderately low damping, intermediate between that of YIG and REIGs. Soumah et al. [119] reported Bi_1Y_2IG with PMA grown on substituted gadolinium gallium garnet (SGGG, $Gd_{2.6}Ca_{0.4}Ga_{4.1}Mg_{0.25}Zr_{0.65}O_{12}$) with damping of $\alpha = 3 \times 10^{-4}$ and FWHM $\mu_0\Delta H_0 = 0.40$ mT measured at an $\approx 27°$ angle from the in-plane direction at frequencies up to 20 GHz. The linewidth was over two orders of magnitude higher for an in-plane

measurement. Lin et al. reported PMA Bi_1Y_2IG grown on SGGG with $\alpha = 7.03 \times 10^{-4}$ [151] and peak-to-peak linewidth of 2 mT (i.e., FWHM = 3 mT) measured out-of-plane in the frequency range of 6–13 GHz.

In this work, we report the structure, magnetic properties, and FMR characterization of BiYIG films that are grown epitaxially on a range of (111)-oriented garnet substrates with varying lattice parameters. In FMR, a limited frequency range for damping measurements can lead to nonlinearities in linewidth as reported in both metallic systems [85] and YIG [152] owing to a slow-relaxing impurity mechanism and low-field losses. We therefore carry out FMR measurements at frequencies up to 40 GHz, obtaining damping as low as 1.3×10^{-4} and inhomogeneous broadening FWHM linewidth of 2–5 mT for an out-of-plane field. The domain structure and reversal characteristics of the films are investigated by MOKE imaging. Finally, a lower bound for the spin-mixing conductance is reported for BiYIG/Pt bilayers, which is comparable with previous reports of spin-mixing conductance in PMA REIG/Pt bilayers.

5.2 Results and Discussion

5.2.1 Structure and Magnetic Anisotropy

BiYIG films ranging from 20–70 nm in thickness were grown by pulsed laser deposition (PLD) on (111)-oriented substituted gadolinium gallium garnets of composition $Y_3Sc_2Ga_3O_5$ (YSGG), SGGG, $Gd_3Sc_2Ga_3O_{12}$ (GSGG), $Gd_{0.63}Y_{2.37}Sc_2Ga_3O_{12}$ (GYSGG), and neodymium gallium garnet ($Nd_3Ga_5O_{12}$, NGG). The bulk lattice parameters of YSGG, SGGG, NGG, GYSGG, and GSGG were 1.2426, 1.2480, 1.2505, 1.2507, and 1.2554 nm, respectively, all larger than that of $Gd_3Ga_5O_{12}$ (GGG) of 1.2375 nm. BiYIG films grown on these substrates therefore exhibit a range of epitaxial strains and magnetoelastic anisotropy. The target used for the thin film growth had a composition of $Bi_{0.8}Y_{2.2}Fe_5O_{12}$. An analysis of the growth conditions that gave high quality epitaxial BiYIG film is given in our previous work [71,153,154], and optimized conditions used in the present work can be found in the Experimental Section. Bi has a larger ionic radius than Y and it causes an expansion of 0.0083 nm per Bi atom substituted in the formula unit [155].

Figure 5.1a shows high resolution X-ray diffraction (HRXRD) 2θ − ω data for BiYIG films grown on GSGG, NGG, GYSGG, SGGG, and YSGG. The well-defined Laue fringes indicate the high crystalline quality and uniformity of the BiYIG films. Both the unstrained and strained unit cell of BiYIG are shown in Figure 1b,c, where the three different lattice sites for the cations with respect to O^{2-} are indicated. Reciprocal-space mapping (RSM) for the (642) reflection shows that all the BiYIG films up to 70 nm thick on GSGG, NGG, and SGGG were lattice matched to the substrate. RSM for 28.3 and 70 nm thick BiYIG films on GSGG is shown in Figure 1d,e. We conclude that the films are under in-plane tensile strain, and the unit cell of the BiYIG is distorted from cubic to rhombohedral (Figure 1c). A rhombohedral-to-hexagonal transformation was used to simplify the calculation of the strain tensor as detailed in our previous work [102]. The in-plane lattice parameter a_H and the c-axis lattice parameter c of the hexagonal unit cell are given by $a_H = \sqrt{12\, d_{11\bar{2}}^2}$ and $c = 12 d_{444}$. Here, $d_{11\bar{2}}$ is the $(11\bar{2})$ plane spacing of the BiYIG cubic unit cell which is assumed to match the substrate $(11\bar{2})$ plane spacing and d_{444} is the spacing of the (444) planes. The corner angle β of the strained unit cell as shown in Figure 1c is given by $\sin\left(\frac{\beta}{2}\right) = \frac{3}{2\sqrt{3+\left(\frac{c}{a_H}\right)^2}}$.

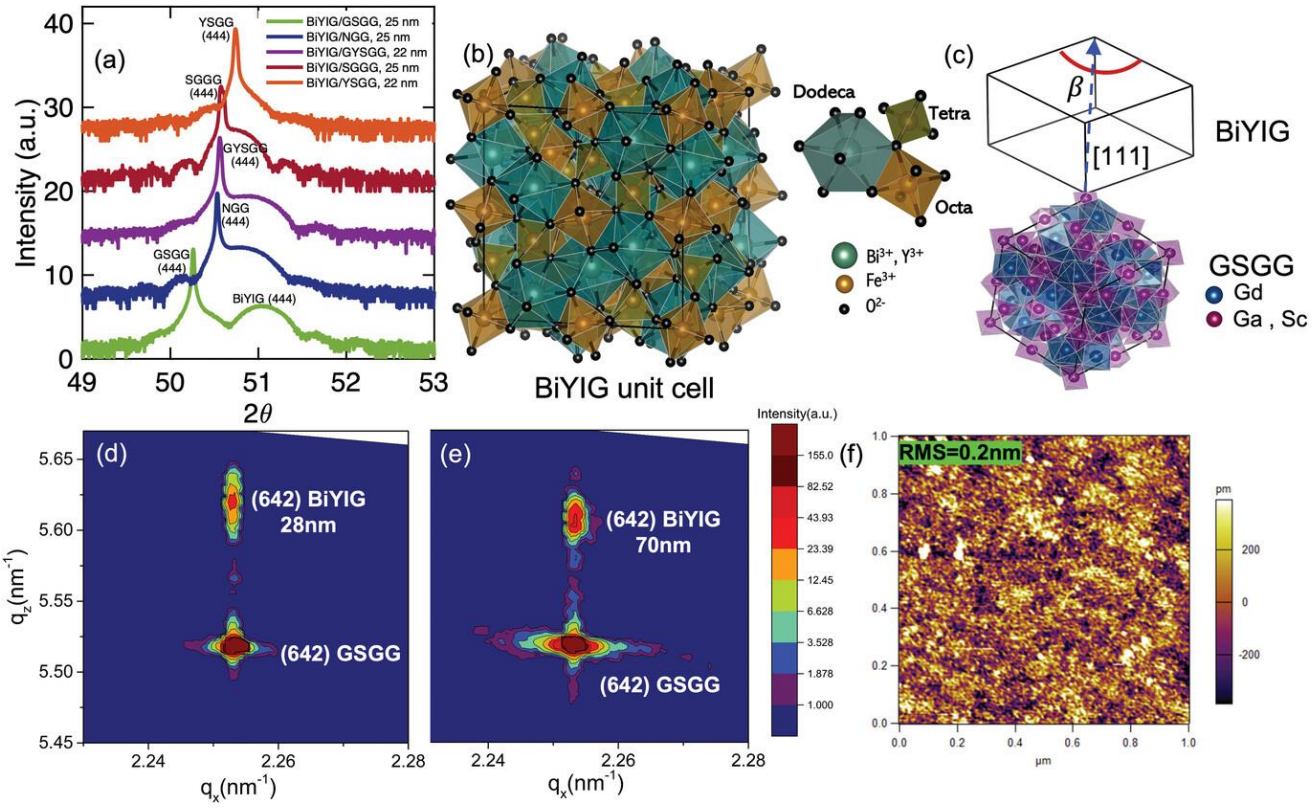

FIG 5.1 a) HRXRD ω−2Θ scans around the BiYIG (444) and GSGG, NGG, GYSGG, SGGG, and YSGG (444) peaks. b) Cubic unit cell of BiYIG showing octahedrally, tetrahedrally, and dodecahedrally-coordinated cation sites. The cation sites are surrounded by O^{2-} (indicated by black spheres) at the vertices of the polyhedra. c) Schematic of a strained BiYIG cubic unit cell on GSGG with the corner angle β marked. d,e) HRXRD reciprocal-space map of 28 nm BiYIG/GSGG (d) and 70 nm BiYIG/GSGG (e). f) AFM scan on 7 nm thick BiYIG film on GSGG.

Atomic force microscopy (AFM) shows that the BiYIG films have a root mean square (RMS) surface roughness of less than 0.2 nm (Figure 1f). High-resolution high-angle annular dark-field scanning transmission electron microscopy (HAADF STEM) images of 7 nm thick BiYIG grown on GSGG were described in our prior publication [156] and indicate epitaxial growth without visible dislocations or other interfacial defects.

The magnetic hysteresis loops of the films were characterized by vibrating sample magnetometry (VSM). Measurements with field applied in-plane (IP) and out-of-plane (OP) are shown in Figure 2 a–f. The films

grown on GSGG and NGG demonstrate PMA with square OP hysteresis loops whereas films grown on SGGG have an IP easy axis. BiYIG films grown on NGG, YSGG, and GYSGG show OP coercivity of ≈ 1.6 kA m^{-1} and films on GSGG have higher coercivity of 8.0 kA m^{-1}. The saturation magnetization of BiYIG was (135 ± 10) kA m^{-1} for thicknesses of 20–70 nm on all the substrates. The large paramagnetic background signal of the GSGG, NGG, and SGGG substrates prevented background subtraction for the hard axis loops of most of the BiYIG films, and net anisotropy was measured using FMR as described below.

The total magnetic anisotropy of the films includes contributions from magnetocrystalline, shape, magnetoelastic, and growth-induced anisotropy. The total uniaxial anisotropy K_u of the films was given by the difference between the magnetic energy E when the magnetization was oriented IP versus OP:

$$K_u = E_{IP} - E_{OOP} = K_{mc} + K_{sh} + K_{me} + K_g$$
$$= \frac{-K_1}{12} - \frac{\mu_0}{2} M_s^2 + \frac{9}{4} c_{44} \lambda_{111} \left(\frac{\pi}{2} - \beta\right) + K_g \qquad (5.1)$$

Here, K_{mc} is the magnetocrystalline, K_{sh} the shape, K_{me} the magnetoelastic, and K_g the growth-induced anisotropy. K_1 is the first order cubic magnetocrystalline anisotropy constant, M_s is the saturation magnetization, λ_{111} is the magnetostriction coefficient, c_{44} is the shear modulus, and β is the corner angle of the rhombohedrally-distorted unit cell. A positive K_u corresponds to an out-of-plane easy axis. K_1 for BiYIG is negative which favors PMA for (111) films, but this contribution is small (≈ −650 J m^{-3} [54]); and thus, the magnetocrystalline anisotropy will be neglected. The shape anisotropy ($-\frac{\mu_0}{2} M_s^2$) favors in-plane magnetization.

K_{me} is proportional to both λ_{111} and the shear strain ($\frac{\pi}{2} - \beta$). The magnitude of λ_{111} is linearly dependent on the Bi content according to [54] λ_{111} ($Bi_zY_{3-z}IG$) = − 2.73 × 10^{-6} (1 + 0.23z). The higher magnetostriction of BiYIG compared to YIG is attributed to an increase in the spin-orbit coupling due to mixing between the 6p Bi^{3+} orbitals and the 3d and 2p orbitals from $Fe^{3+}$and O^{2-}. [54] The λ_{111} for BiYIG

is negative; and therefore, favors an easy axis along the compressively strained OP direction, promoting PMA in BiYIG films grown on larger lattice parameter substrates. Thus, magnetoelastic anisotropy contributes to PMA in BiYIG films grown on substrates with larger lattice parameter than that of the film.

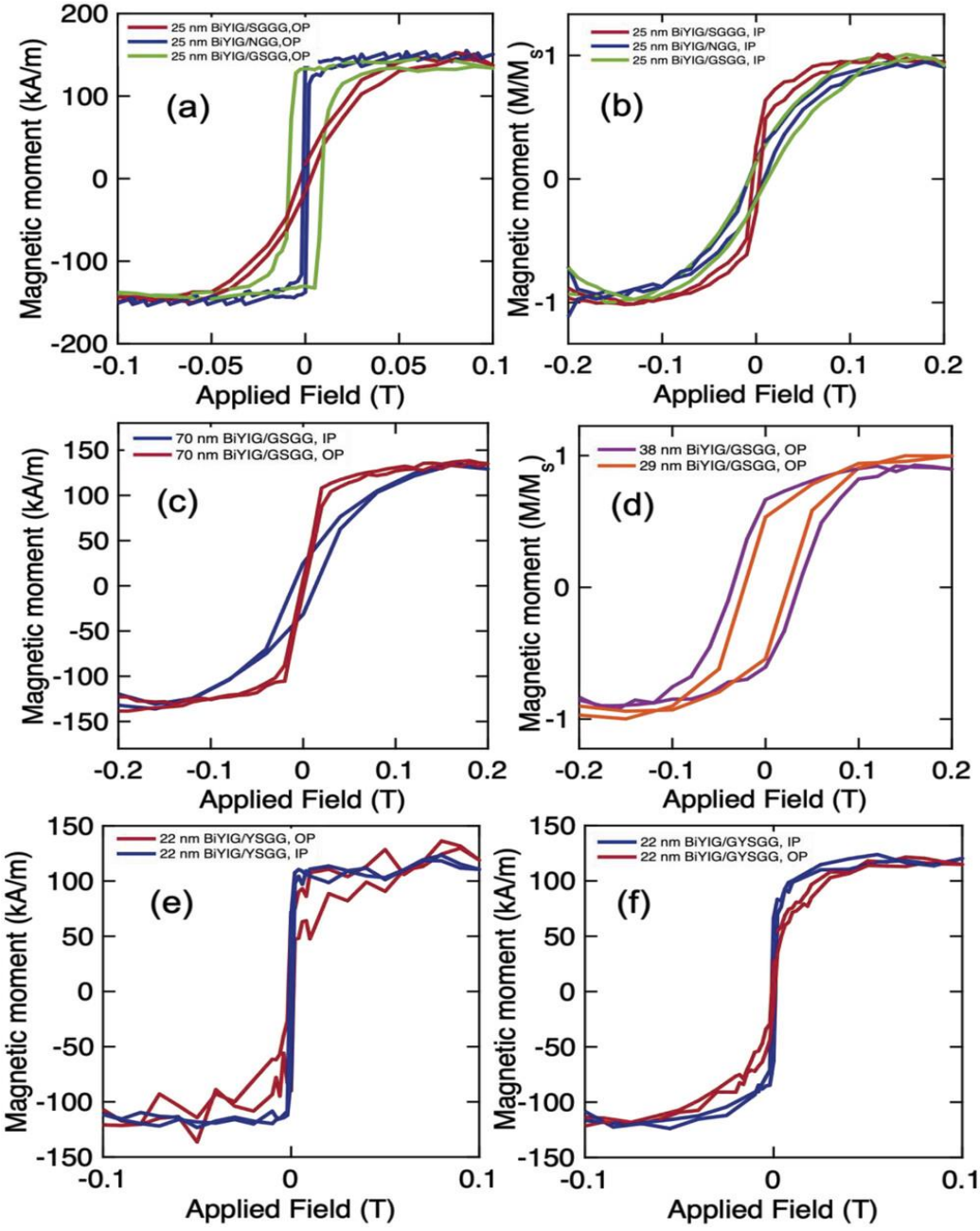

FIG 5.2: Hysteresis loops with field applied a) out-of-plane (OP) and b) in-plane (IP) for 25 nm BiYIG on SGGG, NGG, and GSGG. c) IP and OP loops for 70 nm BiYIG on GSGG. d) OP loops for 38 and 28 nm BiYIG on GSGG. e,f) IP and OP loops for 22 nm BiYIG on YSGG and GYSGG.

Like Soumah et al. [119], we find that magnetoelastic anisotropy alone is insufficient to account for the PMA in our BiYIG films, as shown in Table 1. We observe an increase in β with increasing substrate lattice parameter, as expected. However, the net anisotropy does not increase monotonically with the strain. In fact, the magnetoelastic contribution is a relatively small part of the total anisotropy, leading to the conclusion that the growth-induced anisotropy is dominant. Partially substituted garnet films like BiYIG exhibit K_g due to the non-random distribution of Bi^{3+} and Y^{3+} in nonequivalent dodecahedral sites, driven by the ionic size difference. Growth-induced anisotropy has been analyzed in mixed rare earth and other mixed composition garnets grown by liquid phase epitaxy (LPE) [46,157–160], and more recently, in PLD-grown (Tm,Y)IG [141]. It leads to a uniaxial magnetic anisotropy term in (111)-oriented (and (001)-oriented) films. The magnitude and the sign of K_g depend on the ions present and their atomic fraction, and for Bi^{3+} substitution in YIG, K_g favors PMA [161]. In LPE-grown Bi-containing $(Y,Lu)_3Fe_5O_{12}$, the addition of Bi can increase K_g by an order of magnitude [162]. We calculate K_g from the total anisotropy K_u after subtracting the shape and magnetoelastic contributions. BiYIG on GSGG and NGG have very large growth-induced anisotropies while films on SGGG, GYSGG, and YSGG have lower growth-induced anisotropy and an in-plane easy axis as shown in Figure 2. K_g calculated for the PLD-grown BiYIG in Table 1 varies with substrate and film thickness, and in many samples, it exceeds that of LPE-grown garnets [157–160,163] and PLD-grown (Tm,Y)IG [141].

5.2.2 Domain Imaging

Magneto-optical Kerr effect (MOKE) microscopy was carried out on PMA BiYIG films with thicknesses 25, 28, and 33 nm grown on GSGG substrates, and 25 and 27 nm grown on NGG substrates. All the films were a.c. demagnetized using an electromagnet with an alternating OP magnetic field with an initial value of $\mu_0 H = 500$ mT and a reduction ratio of 0.95 between each step. MOKE images for the resulting domain structures for these films are shown in Figure 3. After demagnetization, the net magnetization is close to zero and up and down domains occupy roughly equal areas. The average domain size was calculated using

images taken from multiple locations on each film and is displayed in Table 1. The large standard deviations in the domain sizes are indicative of heterogeneities in the domain structures in different regions of the samples.

MOKE images for a.c. demagnetized films with thickness 25 nm grown on GSGG and 25 and 27 nm grown on NGG show a labyrinthine domain structure, Figure 3a,d,e. In comparison, 28 and 33 nm BiYIG films on GSGG show triangular domains indicating preferential formation of domain walls along certain crystallographic directions. (Figure 3b, c). The two films in our study that exhibited triangular domains also have higher lattice distortion β and higher K_{me} as well as higher K_g compared to similar thickness films with stripe domains. This suggests that the domain shape correlates with strain state and anisotropy and has a different origin from the triangular domain structures reported in thin metal films [164,165]. There have been multiple reports of threading and misfit dislocation defects in micron-thickness BiYIG films due to lattice and thermal mismatch [166–169]. We speculate that localized strain relaxation accompanied by the formation of dislocations leads to crystallographically-preferred orientations for domain walls due to favorable interaction with their strain fields which can potentially result in anisotropy in the domain wall energy. The critical lattice mismatch causing the onset of triangular defects has been reported to be 4.1 pm (at growth temperatures) in REIGs and lower in Bi-substituted garnets [166]. At room temperature, our BiYIG/GSGG has a lattice misfit of 10.4 pm which is well above this threshold.

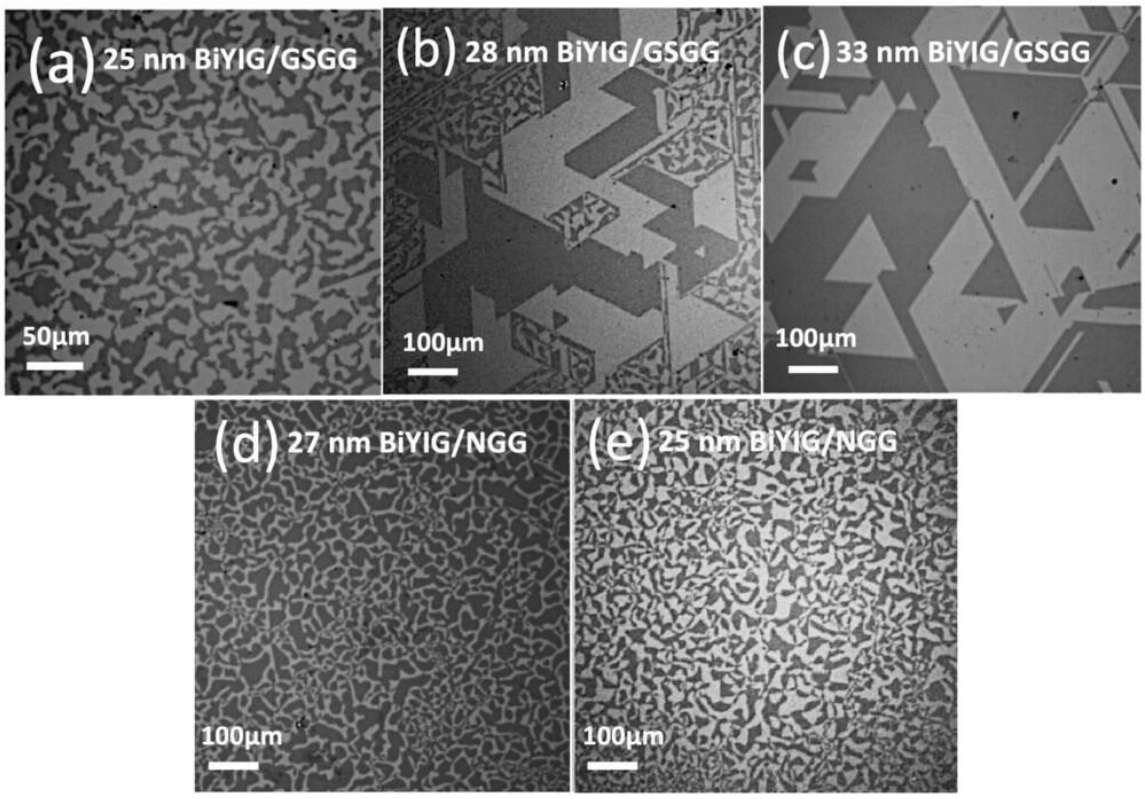

FIG 5.3: MOKE images showing equilibrium domain structure after a.c. demagnetization of a) 25 nm BiYIG/GSGG, b) 28 nm BiYIG/GSGG, c) 33 nm BiYIG/GSGG, d) 27 nm BiYIG/NGG, and e) 25 nm BiYIG/NGG.

MOKE microscopy was used to study magnetization reversal for 28 and 70 nm thick BiYIG/GSGG and 25 nm BiYIG/NGG, Figure 4. MOKE images were collected while applying an OP magnetic field of −60 mT, followed by an OP field sweep from 0 mT to a positive value to magnetize the film in the positive direction. The image collected at −60 mT was subtracted from all the subsequent images to remove the non-magnetic contrast.

Magnetization reversal for 70 nm BiYIG/GSGG and 25 nm BiYIG/NGG shown in Figure 4 a,b proceeds by formation of labyrinthine stripe domains. A similar stripe domain structure has been reported for TmIG [170] and (Tm,Y)IG [141]. Magnetization reversal was almost complete at +15 mT for the 70 nm thick BiYIG/GSGG substrate and at +4 mT for the 25 nm thick BiYIG/NGG. However, magnetization reversal for the 28 nm thick BiYIG/GSGG proceeded by formation of triangular domains such as those

observed in its a.c.-demagnetized state, along with stripe domains within the triangular regions as shown in Figure 4c. After applying −60 mT, the field was swept from 0 mT to +100 mT with 0.5 mT steps. The film did not reach positive saturation even at +100 mT. This agrees with the hysteresis loop of this film shown in Figure 2d, where the film is not saturated even at 200 mT. A supplementary video showing the images in 0.5 mT field increments from 0 to 100 mT has been included as Supporting Information.

5.2.3 Ferromagnetic Resonance Characterization

To extract the damping of the BiYIG thin films, their dynamic magnetic properties were studied with broadband perpendicular FMR spectroscopy based on the vector network analyzer (VNA) technique in the 10–40 GHz range [85–87,171]. The complex transmission parameter S_{21} was measured at a fixed frequency while the external perpendicular magnetic field was swept [85], as shown in Figure 5a,b. The resonance field for the films was fitted to the Kittel equation for perpendicular geometry to extract the effective magnetization M_{eff} and the Landé g-factor [172], as shown in Figure 5c for one film as an example. Here:

$$H_{res} = \frac{2\pi f}{|\gamma|\,\mu_0} + M_{eff} \qquad (5.2)$$

where H_{res} is the resonance field, f is the excitation frequency, and γ is the gyromagnetic ratio $(g\mu_B)/h$, where μ_B is the Bohr magneton and $\hbar$ is the reduced Planck constant. The anisotropy of the film excluding the shape anisotropy, $K = K_u - K_{sh}$, is extracted from M_{eff} using the equation [20,30]:

$$M_{eff} = M_s - \frac{2\,K}{\mu_0\,M_s} \qquad (5.3)$$

The damping α and the inhomogeneous broadening FWHM linewidth ΔH_0 were extracted by fitting the linewidth to the following expression, Figure 5d–f:

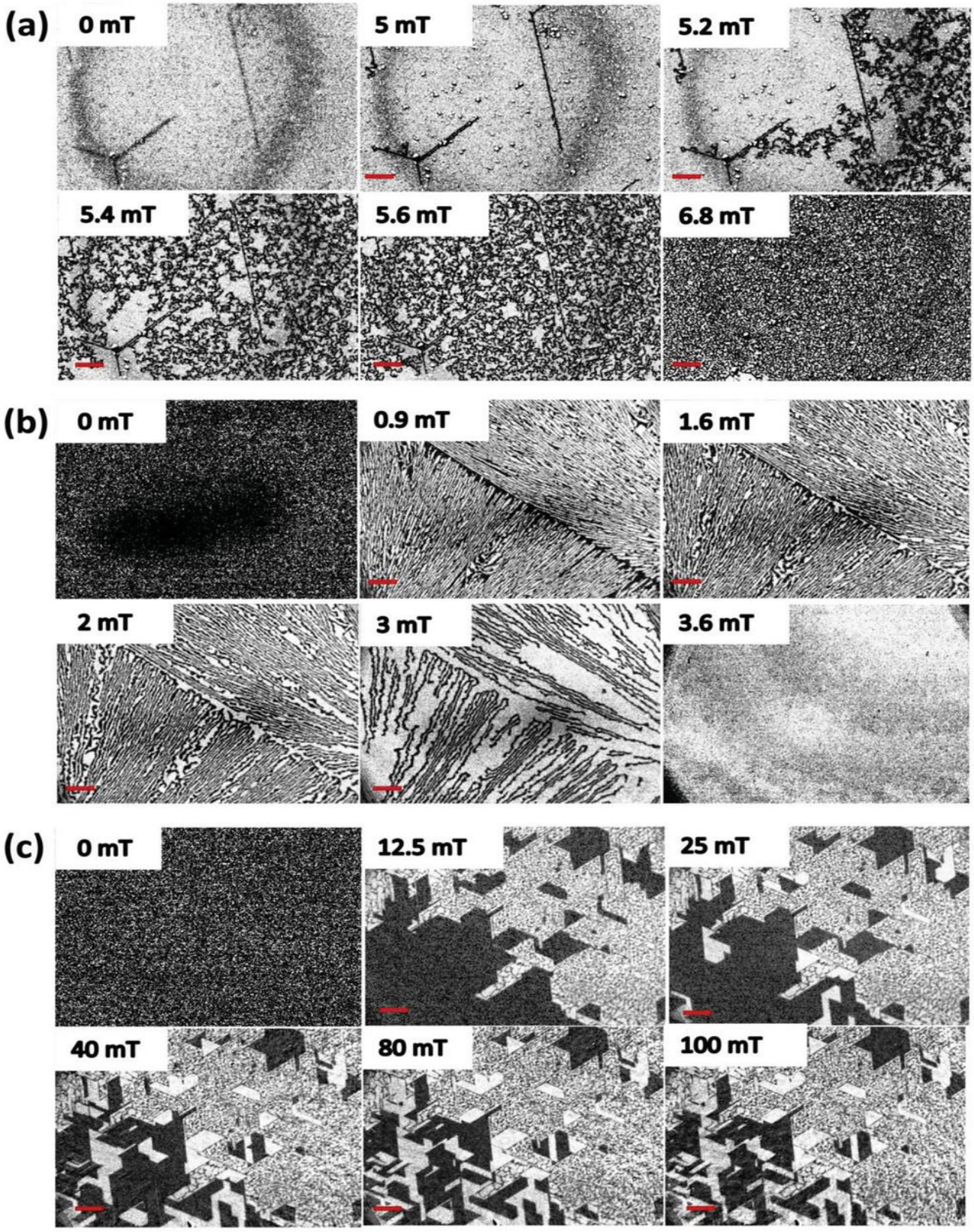

FIG 5.4: MOKE images showing domain structure during reversal of a) 70 nm BiYIG/GSGG, b) 25 nm BiYIG/NGG, and c) 28 nm BiYIG/GSGG. The films were saturated at +60 mT for (a) and −60 mT for (b,c). The red scale bar represents 100 μm.

$$\Delta H = \frac{4\pi\alpha f}{|\gamma|\ \mu_0} + \Delta H_0 \qquad (5.4)$$

where ΔH is the experimentally observed linewidth determined from fitting the S_{21} data with the complex susceptibility. 25 nm BiYIG/SGGG yielded $\alpha = 1.3 \times 10^{-4}$ and $\mu_0\Delta H_0 = 2.7$ mT. For 70 nm BiYIG/GSGG, $\alpha = 5.6 \times 10^{-4}$ and $\mu_0\Delta H_0 = 5$ mT, and for 23 nm BiYIG/NGG, α was higher at 2.1×10^{-3}, with $\mu_0\Delta H_0 = 3.7$ mT. No systematic change was observed with varying thickness or substrate, but the higher damping of BiYIG/NGG may correlate with the comparatively poorer crystalline quality of the as-supplied NGG substrates that led to growth of BiYIG with lower intensity Laue fringes. Our results confirm that low damping and moderately low linewidth of a few mT are achievable for BiYIG measured in the OP direction up to 40 GHz.

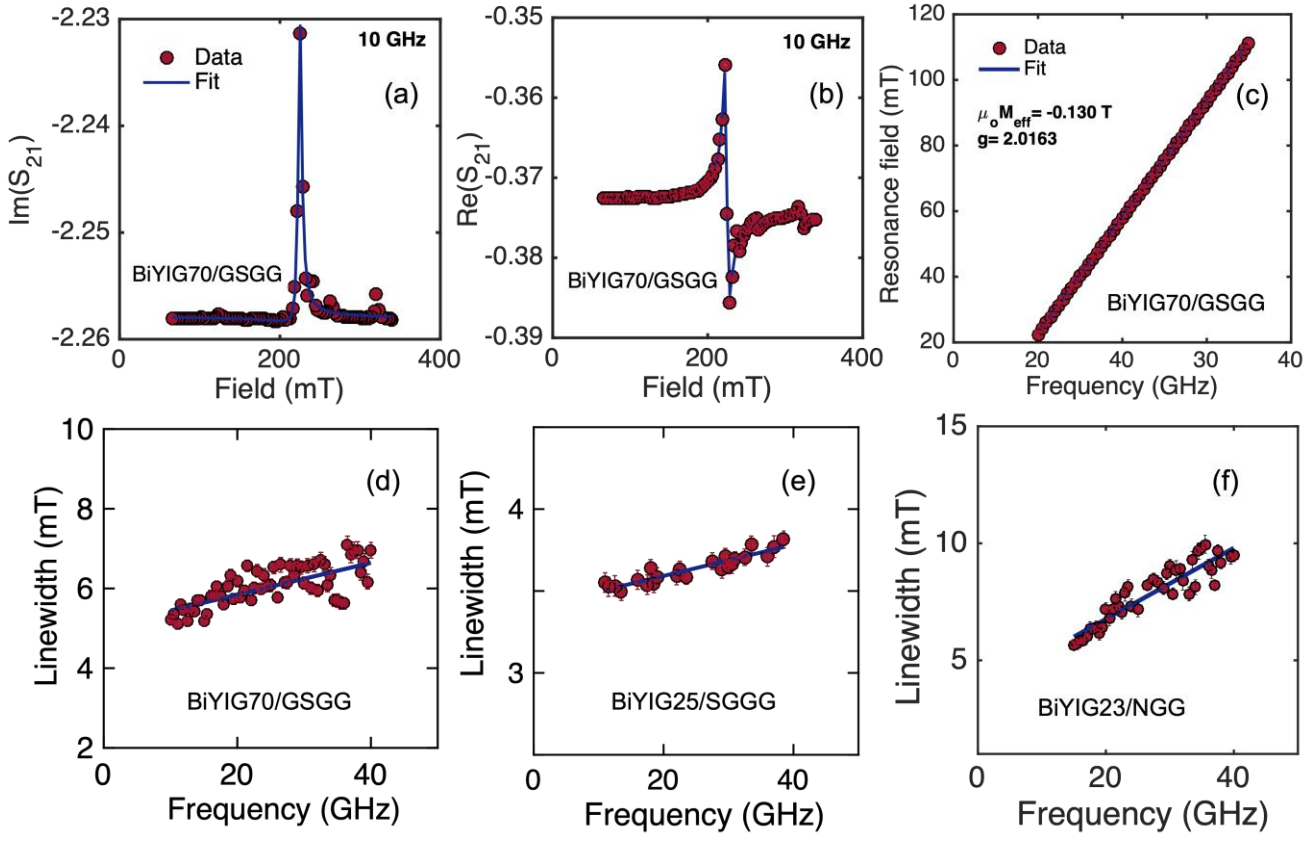

FIG 5.5: Representative FMR spectra taken at 10 GHz showing a) the imaginary and b) the real part of S21 for a 70 nm BiYIG/GSGG. c) Representative fit of the resonant field, H_{res}, versus frequency for 70

nm BiYIG/GSGG. FMR linewidth as a function of frequency for d) 70 nm BiYIG/GSGG, e) 25 nm BiYIG/SGGG, and f) 23 nm BiYIG/NGG.

5.2.4 Spin Mixing Conductance of BiYIG/Pt Interface

To characterize the efficiency of spin transport through the Pt/BiYIG interface, we measure the spin-mixing conductance of a bilayer of 4 nm Pt/4.3 nm BiYIG. A charge current in the Pt yields a spin current perpendicular to the film due to the spin Hall effect (SHE). The spin current is partially reflected at the garnet/heavy metal (HM) interface based on the relative orientation of the polarization of the spin current (σ) and the magnetization of the garnet (m). The real component of spin-mixing conductance $G_r^{\uparrow\downarrow}$ is associated with a damping-like torque which is proportional to $m \times (\sigma \times m)$, and the imaginary component of spin-mixing conductance $G_i^{\uparrow\downarrow}$ is associated with a field-like torque which is proportional to $\sigma \times m$ [8,97]. The reflected spin current produces a charge current in the HM layer due to the inverse spin Hall effect; and thus, modulates the resistance of the HM layer leading to a spin Hall magnetoresistance (SMR). Longitudinal and transverse components of SMR are given by the following equations [94,102]:

$$R = R_0 + \Delta R^{SMR} sin^2\theta \, sin^2\varphi \qquad (5.5)$$

$$R_H = R_H^{SMR} sin^2\theta \, sin(2\phi) + R_H^{AHE,SMR} \cos\theta + R_H^{OHE} H_z \qquad (5.6)$$

Here R_0 is the m-independent longitudinal resistance of the HM layer and ΔR^{SMR} is its modulation due to SMR. R_H^{SMR} and $R_H^{AHE,SMR}$ are the transverse components of SMR and anomalous Hall effect (AHE)-like SMR, respectively. R_H^{OHE} is the contribution from the ordinary Hall effect (OHE) of the HM, H_z is the out-of-plane magnetic field, and θ and φ are the polar and azimuthal angles of m [100]. The Pt (4 nm)/BiYIG (4.3 nm)/NGG heterostructure was patterned into Hall cross devices and a probe station was used to perform transverse SMR measurements with an out-of-plane magnetic field. The Hall resistance for an OP field sweep from −15 to +15 mT is shown in Figure 6a after subtraction of a sample-dependent offset

and linear OHE signal. The loop shows 100% remanence which agrees with the PMA observed from the VSM measurements. Sharp switching can be observed with a coercivity of (3 ± 0.5) mT. We obtained values of $R_H^{AHE,SMR} = -0.86$ mΩ and $R_H^{OHE} = -10.7$ mΩ T^{-1}, which gives $\rho_{xy}^{AHE,SMR} = -3.44 \times 10^{-4}$ μΩ cm and $\rho_{xy}^{OHE} = -4.28 \times 10^{-3}$ μΩ cm T^{-1}. The maximum magnitude of magnetic field available in the probe station was 100 mT which was not sufficient to saturate the film IP, precluding in-plane SMR measurements.

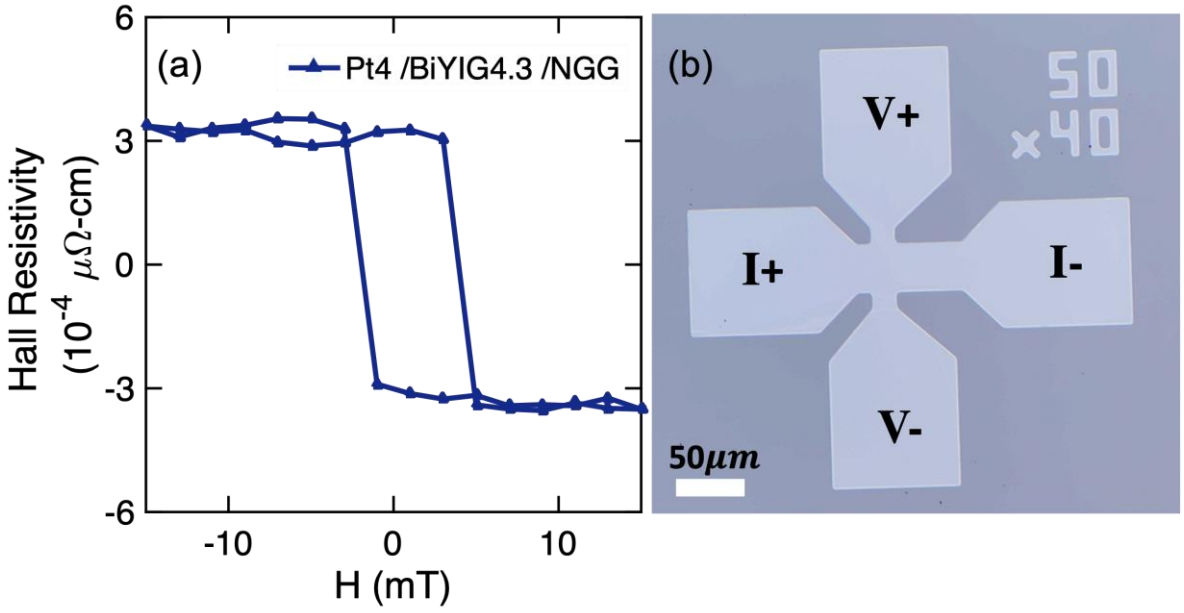

FIG 5.6. a) Anomalous Hall effect (AHE)-like spin Hall magnetoresistance (SMR) hysteresis loops for NGG(111)|BiYIG(4.3 nm)/Pt(4 nm) heterostructure. b) Optical micrograph of Hall cross used for measurement.

The model of Chen et al. for spin mixing conductance yields [95]:

$$\frac{\rho_{xy}^{SMR}}{\rho_{xx}^{Pt}} = \frac{\theta_{SH}^2 \lambda_{Pt}}{d_N} \frac{2\lambda_{Pt} G_r \tanh^2 \frac{d_N}{2\lambda_{Pt}}}{\sigma_{xx}^{Pt} + 2\lambda_{Pt} G_r \coth \frac{d_N}{2\lambda_{Pt}}} \qquad (5.7)$$

$$\frac{\rho_{xy}^{AHE,SMR}}{\rho_{xx}^{Pt}} = \frac{2\theta_{SH}^2 \lambda_{Pt}^2}{d_N} \frac{\sigma_{xx}^{Pt} G_i \tanh^2 \frac{d_N}{2\lambda_{Pt}}}{(\sigma_{xx}^{Pt} + 2\lambda_{Pt} G_r \coth \frac{d_N}{\lambda_{Pt}})^2} \qquad (5.8)$$

where ρ_{xy}^{SMR} and $\rho_{xy}^{AHE,SMR}$ are Hall resistivities due to SMR and AHE-like SMR, respectively; $\rho_{xx}^{Pt} = 47.1$ μΩ cm is the resistivity (and σ_{xx}^{Pt} is the conductivity) of Pt which we measure from the Hall bar, θ_{SH} is the spin-Hall angle of Pt, λ_{Pt} is the spin diffusion length in Pt, d_N is the thickness of the Pt layer = 4 nm, and G_r and G_i are the real and imaginary components of spin-mixing conductance. Without being able to achieve IP saturation for the film, we cannot obtain ρ_{xy}^{SMR}; and hence G_r. However, $\lambda_{Pt}G_r$ is generally much lower than σ_{xx}^{Pt} [98,120]. Thus, if we drop G_r in the denominator of the second equation, we can obtain a lower bound for G_i. This value is $3.1 \times 10^{12}\ \Omega^{-1}\ m^{-2}$ for $\theta_{SH} = 0.08$ [173], $\lambda_{Pt} = 1.4$ nm [95] or $6.1 \times 10^{10}\ \Omega^{-1}\ m^{-2}$ for $\theta_{SH} = 0.387$ [173], and $\lambda_{Pt} = 4.2$ nm [174]. G_i is comparable to previous results reported for several REIG/Pt interfaces, [120] suggesting that the spin transport across the interface is dominated by the Fe sublattices.

Table 5.1: Magnetic properties of BiYIG films on garnet substrates

Film thickness (nm)	Substrate	PMA	β (°)	K_u- K_{sh} (kJ m^{-3})	K_{sh} (kJ m^{-3})	K_{me} (kJ m^{-3})	K_{sh} + K_{me} (kJ m^{-3})	K_g (kJ m^{-3})	Domain shape	Domain size (μm)
22	YSGG	No	90	≈10.7	−10.7	0	−10.7	10.7	–	–
25	SGGG	No	90.1	11.1	−13.2	1.7	−11.5	9.4	–	–
25	NGG	Yes	90.2	29.1	−13.1	2.2	−10.9	26.9	Stripe	30 ± 9
27	NGG	Yes	90.3	25.5	−11.1	3	−8.1	22.5	Stripe	26 ± 8
22	GYSGG	No	90.3	≈9.8	−9.8	3	−6.8	6.8	–	–
25	GSGG	Yes	90.6	30.2	−9.8	5.8	−4.0	24.4	Stripe	32 ± 8
28	GSGG	Yes	90.7	49.2	−13.1	7.1	−6.0	42.1	Triangular	67 ± 22
32.9	GSGG	Yes	90.7	44.8	−13.2	7.1	−6.1	37.7	Triangular	84 ± 35
70	GSGG	Yes	90.6	17.9	−12.3	5.8	−6.5	12.1	Stripe	–

5.3 Conclusion

Epitaxial BiYIG films with thicknesses ranging from 20 to 70 nm were grown by pulsed laser deposition from a target with composition $Bi_{0.8}Y_{2.2}Fe_5O_{12}$ onto several (111)-oriented single crystal garnet substrates with different lattice parameters. The films were coherently strained to the substrates and increasing the lattice parameter of the substrates promoted perpendicular magnetic anisotropy. Magnetoelastic anisotropy was insufficient to explain the net anisotropy, implying the presence of growth-induced anisotropy of 7–42 kJ m^{-3}, generally higher for more highly strained films. Most of the films exhibited stripe domains, but the films with highest anisotropy showed triangular domain patterns. We found a lower

bound for the spin mixing conductance which was similar to that of other iron garnets, a damping of 1.3 × 10^{-4} to 2.1 × 10^{-3}, and an inhomogeneous broadening of $\mu_0 H_0$ = 2.7–5 mT for out-of-plane measurements up to 40 GHz. The low damping, tunable anisotropy, and high magnetooptical contrast were advantageous for a range of magnetooptical and spintronic applications and phenomena.

5.4 Experimental Section

BiYIG films ranging from 20 to 70 nm in thickness were grown by pulsed laser deposition (PLD) on (111) oriented substituted gadolinium gallium garnets YSGG, SGGG, NGG, GYSGG, and GSGG. The target used for the thin film growth had a composition of $Bi_{0.8}Y_{2.2}Fe_5O_{12}$. The chamber was pumped to 5 × 10^{-6} Torr base pressure prior to introducing oxygen and depositing the films. The laser repetition rate was 10 Hz, the laser fluence was ≈ 2 J cm^{-2}, and the target-substrate distance was 6 cm. The substrate temperature was 560 °C and the O_2 pressure was 20 Pa (150 mTorr). After growth, the samples were cooled down under 230 Torr of O_2. Pt was grown in a magnetron sputtering system at room temperature, with an Ar pressure of 0.26 Pa (2 mTorr). HRXRD measurements were performed using a Bruker D8 Discover HRXRD. For broadband perpendicular FMR spectroscopy based on the vector network analyzer technique, the samples were placed face-down on a 50 Ω coplanar waveguide. A static out-of-plane magnetic field up to 2.2 T was swept to saturate the film in the out-of-plane direction. A variable microwave field was applied in-plane while the microwave transmission at frequencies from 10–40 GHz was measured. Certain commercial instruments were identified to specify the experimental study adequately. This does not imply endorsement by NIST or that the instruments were the best available for the purpose.

Contributors:

Deposition of films, VSM, XRD, MOKE measurements, analysis and manuscript preparation were performed jointly by Takian Fakhrul and author of this thesis. FMR measurements were performed by Hans Nembach, Justin Shaw and Grant Riley.

Chapter 6: Damping and interfacial Dzyaloshinskii–Moriya interaction in thulium iron garnet/bismuth-substituted yttrium iron garnet bilayers

This work is adapted from a publication which the author wrote and published in ACS Applied Materials & Interfaces [175]. *It is presented mostly in unaltered form.*

6.1 Introduction

Magnetically ordered oxide materials such as spinels, ferrites [176,177] and rare earth iron garnets (REIGs) [102,178,179] have been studied intensely for spintronic and photonic devices. In REIGs, the choice of rare earth (or other) ion allows tuning of a variety of properties including saturation magnetization, compensation temperature, [180,181] magnetocrystalline anisotropy, [182] magnetostriction [183] and Gilbert damping. [28,120] Magnetoelastic anisotropy can be introduced via lattice mismatch strain in epitaxial films or thermal mismatch strain for films grown on silicon or other non-garnet substrates, [98,99] and growth induced anisotropy can be present in REIGs with mixed RE ions. [141,184]

Thin films of a number of REIGs have been grown with perpendicular magnetic anisotropy (PMA), [8,121,185] which is advantageous for the study of spin orbit torque (SOT) and other magnetic phenomena. REIGs are good insulators, enabling lower ohmic losses than metallic ferromagnets as they avoid parasitic current shunting from a metal overlayer. [67] PMA in epitaxial REIGs can be present even for thick films, as it originates from bulk anisotropy terms unlike the interfacial anisotropy dominating metallic ferromagnet films. [67,141] Thulium iron garnet ($Tm_3Fe_5O_{12}$ (TmIG))/heavy metal (HM) stacks grown epitaxially on gallium garnet substrates are the most extensively studied PMA REIG films in terms of their spintronic properties. [30,68,100,103,148] TmIG|Pt heterostructures exhibit considerable spin transparency at the interface, comparable to that of the Co|Pt interface, [8,186] and current induced switching of TmIG has been demonstrated using the damping-like SOT from a Pt overlayer. [68,70,156,187]

The Dzyaloshinskii–Moriya interaction (DMI) plays an important role in the stabilization and current driven manipulation of chiral magnetic textures including Néel domain walls and skyrmions, which have been proposed to represent bits in data storage devices. [72,73] Key ingredients to obtain interfacial DMI are a broken inversion symmetry at the interface [70] and spin-orbit coupling. [74] While the HM overlayer contributes some spin-orbit coupling, [188] it appears that the RE^{3+} ions provide a critical contribution to DMI, [156] evident from the observation of DMI-stabilized skyrmions in TmIG grown on $Gd_3Ga_5O_{12}$ (GGG) in the absence of any HM overlayer [103] and the absence of DMI in bismuth substituted yttrium iron garnet (BiYIG) (an iron garnet which does not have strong spin-orbit coupling due to the absence of RE^{3+} ions) with a HM overlayer. [156] The DMI in TmIG|Pt heterostructures stabilizes chiral Néel domain walls which can be translated by SOT produced by a charge current in the Pt overlayer without application of any in-plane field. [156] The strength of DMI for TmIG films varies with the substrate composition and has a non-monotonic dependence on lattice mismatch strain, reaching 0.029 mJ m^{-2}. [188,189]

Gilbert damping governs the magnetization dynamics, including the critical current required for magnetization reversal in spin-transfer-torque devices [146,190] and the domain wall velocity for racetrack memory devices. [191] Yttrium iron garnet ($Y_3Fe_5O_{12}$, YIG) has the lowest known Gilbert damping, as low as 10^{-5} in bulk. [28,147,149] However, growth of high quality YIG films with PMA has been challenging, despite several demonstrations of epitaxial [112–114] and polycrystalline [115] PMA YIG films. Instead, epitaxial bismuth substituted yttrium iron garnet (BiYIG) can be grown with PMA on garnet substrates with higher lattice parameter than GGG by exploiting a combination of magnetoelastic and growth-induced anisotropies. [29,119] The Gilbert damping of BiYIG films is 1.3×10^{-4} to 5.6×10^{-4}, an order of magnitude higher than that of YIG but much lower than that of REIGs with strong spin-orbit coupling. [28,98,119,120,141] For example the damping of TmIG films is around 0.02. [30,148,192] While the low damping of BiYIG films enables fast domain wall dynamics, BiYIG films exhibit no DMI

and SOT-driven domain wall motion can be achieved only in the presence of an in-plane magnetic field. [71,156]

Garnet thin films with DMI, low damping, and PMA would combine the advantages of fast dynamics and field-free SOT switching and bring substantial benefits to spintronic device development. In this article we introduce a bilayer BiYIG|TmIG which exhibits both DMI and moderate damping. Velez et al. described an exchange-coupled YIG|TmIG|Pt heterostructure, [193] demonstrating DMI-stabilized skyrmions, but the PMA was present only in the TmIG layer and the damping was not reported. There have also been various studies on multilayers of iron garnets for photonic and magneto-optic applications, [194,195] but DMI and damping are not reported. Here we report the growth, and the structural, magnetic and spintronic properties of BiYIG|TmIG heterostructures deposited on substituted gadolinium gallium garnet (GSGG) and neodymium gallium garnet (NGG) substrates. The films have PMA, and bubble domains in BiYIG|TmIG|GSGG were formed by applying simultaneous in-plane field and out-of-plane fields. The key result of this work is showing that BiYIG|TmIG|NGG exhibits both a substantial DMI and damping an order of magnitude lower than that of TmIG.

6.2 Structural and Magnetic Characterization

The $Bi_{0.8}Y_{2.2}Fe_5O_{12}$ target was prepared by solid state sintering, and the TmIG target was purchased from Furuuchi Chemical Corporation. Thin films of BiYIG, codeposited films of $(Tm,Bi,Y)_3Fe_5O_{12}$ (BiYTmIG) and bilayered films of TmIG|BiYIG were deposited on GSGG ($Gd_3Sc_2Ga_3O_{12}$, lattice parameter a = 1.2554 nm) and NGG ($Nd_3Ga_5O_{12}$, a = 1.2505 nm) substrates with (111) orientation using pulsed laser deposition (PLD) with a 248 nm wavelength laser. The BiYTmIG films were codeposited by alternately ablating the targets using 25 laser shots on the BiYIG target and 2 or 5 laser shots on the TmIG target. Based on the calibration of the growth rates from BiYIG and TmIG targets the two codeposited BiYTmIG films have nominal compositions of $Tm_{0.15}Bi_{0.75}Y_{2.1}Fe_5O_{12}$ and $Tm_{0.3}Bi_{0.7}Y_2Fe_5O_{12}$ respectively. The bilayered films consisted of a TmIG layer in contact with the substrate and an overlaid

BiYIG layer. Several studies show DMI originating from the TmIG|substrate interface, [188,189] thus stacks of BiYIG|TmIG|substrate were examined instead of TmIG|BiYIG|substrate. The optimized growth conditions for epitaxial high quality BiYIG films are described in our previous work. [196] The growth conditions used in the present work can be found in the Methods section.

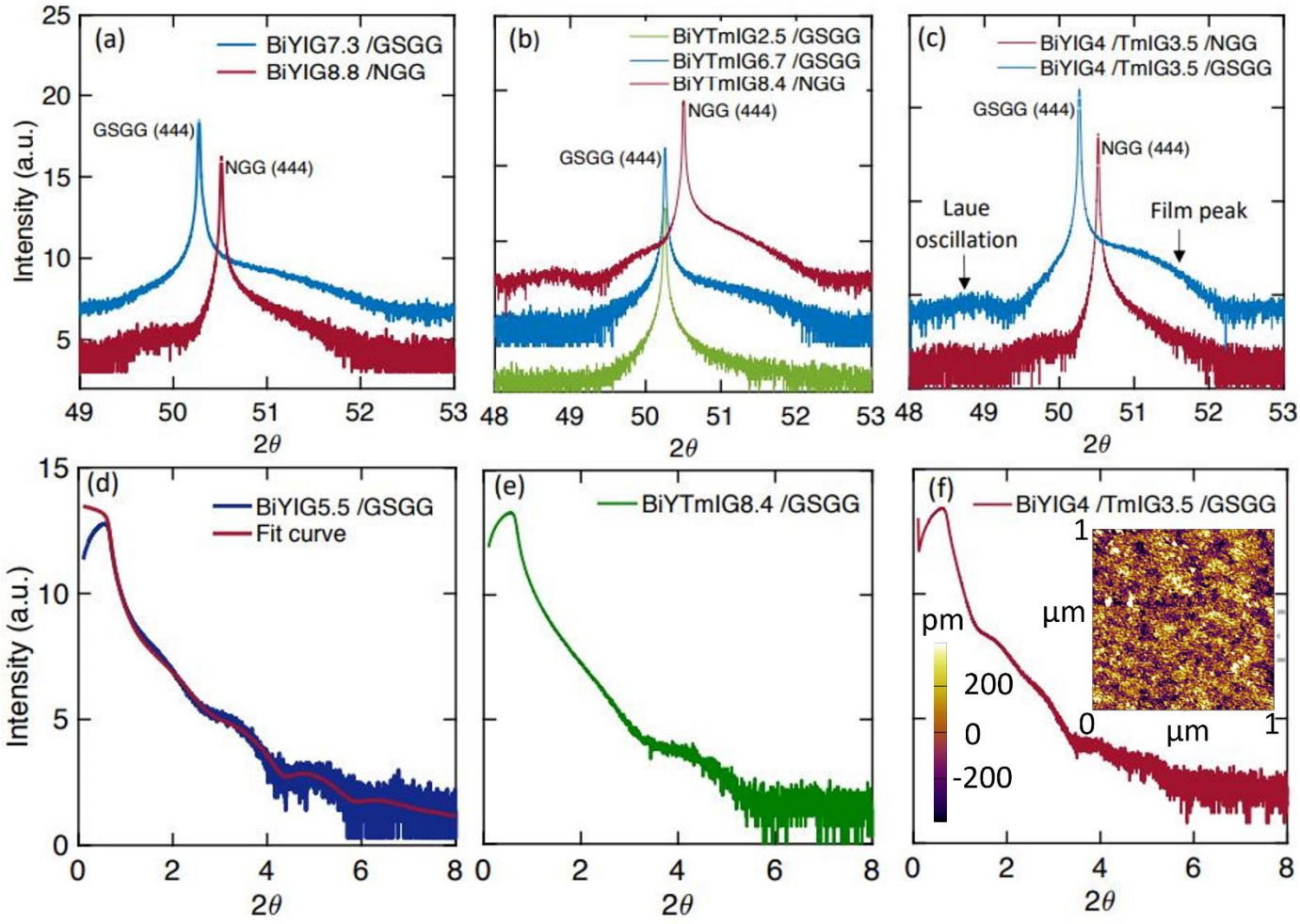

FIG 6.1 (a-c): High-resolution x-ray diffraction (HRXRD) scans of BiYIG, BiYTmIG and BiYIG|TmIG thin films deposited on GSGG and NGG substrates. (d-f): x-ray reflectivity (XRR) scans of BiYIG, BiYTmIG and BiYIG|TmIG thin films deposited on GSGG substrate. A BiYIG:TmIG shot ratio of 25:5 was used for making the 2.5 nm thick BiYTmIG film and 25:2 was used for the 6.7 nm and 8.4 nm thick BiYTmIG films. Inset of (f) shows topographic image from an atomic force microscopy (AFM) scan on BiYIG (3.5 nm)/TmIG (3.1 nm)/GSGG film.

REIGs, YIG and BiYIG belong to the cubic $Ia\bar{3}d$ space group [133] with a lattice parameter of about 1.2 nm, well matched to that of gallium garnets. Fig. 1 shows symmetric high-resolution x-ray diffraction (HRXRD) scans around the (444) substrate peak for BiYIG, codeposited BiYTmIG and bilayered TmIG|BiYIG films. All the films grow with an in-plane tensile strain due to lattice mismatch with the substrates. Due to the few-nm film thickness the intensity of the film peaks and Laue fringes is low, and the film peaks are very broad and overlap the substrate peaks. However, thicker epitaxial iron garnet films grown under similar conditions exhibit well defined film peaks and Laue fringes indicating high crystalline quality and thickness uniformity in epitaxial REIG films. [29,102,141] High-resolution x-ray reflectivity (HRXRR) measurements were performed to determine the film thickness as shown in Fig. 1. Fits to the Kiessig fringes in HRXRR scans for BiYIG and BiYTmIG films deposited on a GSGG substrate indicate uniform thicknesses of 5.5 nm and 8.4 nm respectively. The observation of two distinct periodicities in the HRXRR scan for the bilayered film validates that the BiYIG layer and TmIG layer are not intermixed. Fits to the Kiessig fringes for the bilayered film indicate that the thicknesses of the BiYIG layer and TmIG layer are 4 nm and 3.5 nm respectively. Prior work has shown, based on reciprocal space map (RSM) measurements performed on BiYIG, [29] TmIG [100] and terbium iron garnet (TbIG) [120] epitaxial films deposited on garnet substrates, that such garnet films are fully strained in-plane to match the substrate lattice parameter for thickness of 70 nm, 20 nm and 90 nm respectively. Since all the BiYIG films, bilayered films and codeposited films used in this study have thickness lower than 21 nm, we expect that they are all coherently lattice-matched to the substrate. Atomic force microscopy (AFM) measurements were performed on a BiYIG (3.5 nm)/TmIG (3.1 nm)/GSGG film and its rms surface roughness was 0.2 nm as shown in the inset of Fig. 1 (f).

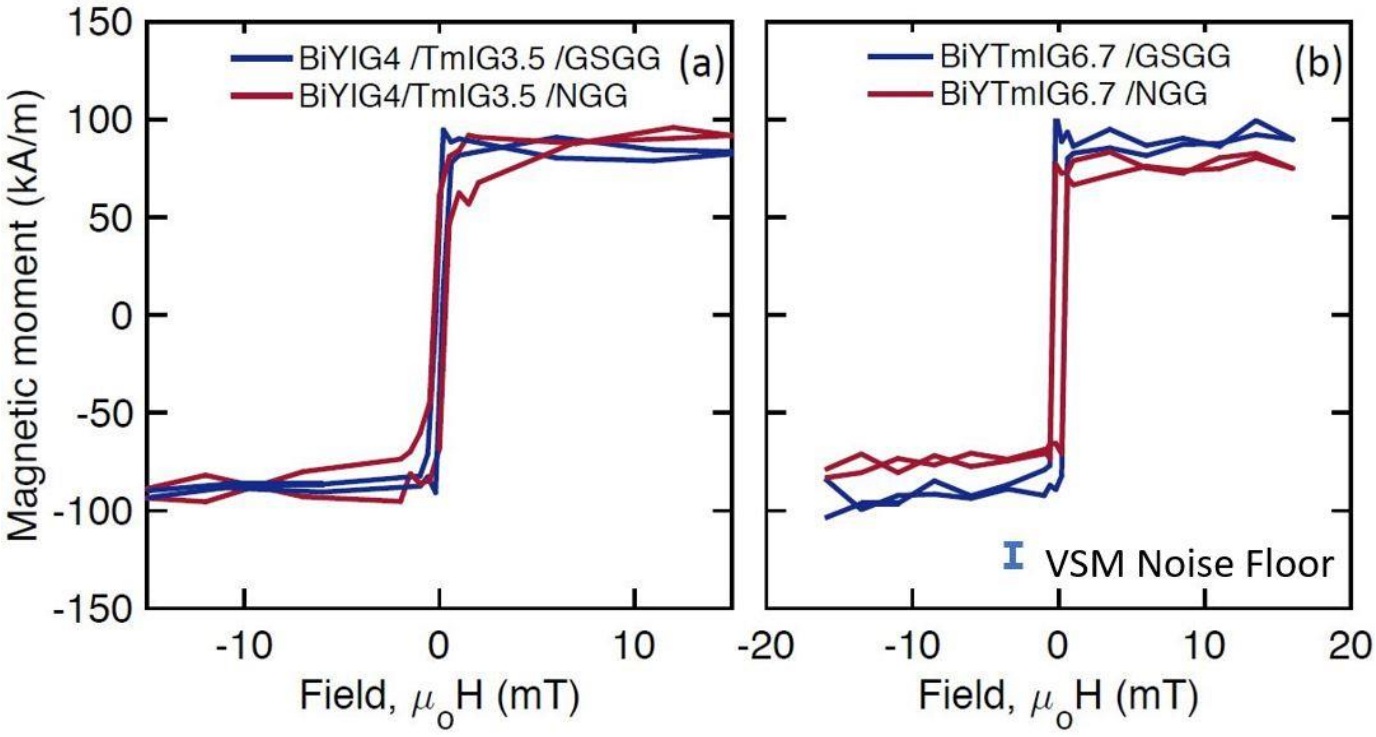

FIG 6.2 Room-temperature out-of-plane vibrating sample magnetometry hysteresis loops of (a) BiYIG (4 nm)|TmIG (3.5 nm) and (b) BiYTmIG (6.7 nm) thin films deposited on GSGG and NGG substrates. A BiYIG:TmIG shot ratio of 25:2 was used for BiYTmIG films.

The uniaxial magnetic anisotropy K_u is defined as the magnetic energy difference between orienting the magnetization direction in-plane (E_{IP}) vs. out-of-plane (E_{OOP}). Positive (negative) K_u implies an out-of-plane (in-plane) easy axis. For an epitaxial iron garnet film lattice-matched to a garnet substrate with (111) orientation, K_u is given by: [98]

$$K_u = E_{IP} - E_{OOP} = -\frac{K_1}{12} - \frac{\mu_0}{2} M_s^2 + \frac{9}{4} c_{44}\, \lambda_{111} \left(\frac{\pi}{2} - \beta\right) + K_G \qquad (6.1)$$

Here K_1 is the first order cubic magnetocrystalline anisotropy constant, which is negative favoring PMA but is negligible compared to the other terms. [138] The second term is shape anisotropy with M_s the saturation magnetization, which favors an in-plane magnetization direction. The third term is the magnetoelastic anisotropy which is proportional to magnetostriction λ_{111} and shear strain ($\pi/2 - \beta$), with β the corner angle of the rhombohedrally distorted unit cell. c_{44} is the shear modulus of the film and its value

lies between 74 GPa and 90 GPa for REIGs. [138] K_G, the fourth term, represents a uniaxial growth-induced anisotropy which originates from preferential occupancy of cations or vacancies in non-equivalent sites. [139–141,184] Surface and interface anisotropies [197] may also contribute to K_u.

All the films in this study exhibited PMA. Vibrating sample magnetometry (VSM) hysteresis loops for representative bilayered films and codeposited films deposited on GSGG and NGG substrates are shown in Fig. 2. The measurement with out-of-plane field shows square hysteresis loops and a low coercivity of less than 400 A/m. The large paramagnetic nonlinear signal of the GSGG and NGG substrates prevented background subtraction for the in-plane hysteresis loops of the films. The saturation magnetization of these films is between 80 - 105 kA/m at room temperature, comparable to TmIG (90-120 kA/m) [100,170] and BiYIG films (125-145 kA/m). [29] Both BiYIG [54] and TmIG [100] have negative λ_{111} and an in-plane tensile strain, so that the magnetoelastic anisotropy favors PMA. Additionally, the growth-induced anisotropy due to preferential occupancy of cations in non-equivalent dodecahedral sites favors PMA in BiYIG, [29,119] and likely also contributes to the anisotropy of the BiYTmIG codeposited film.

6.3 Measurements of Damping

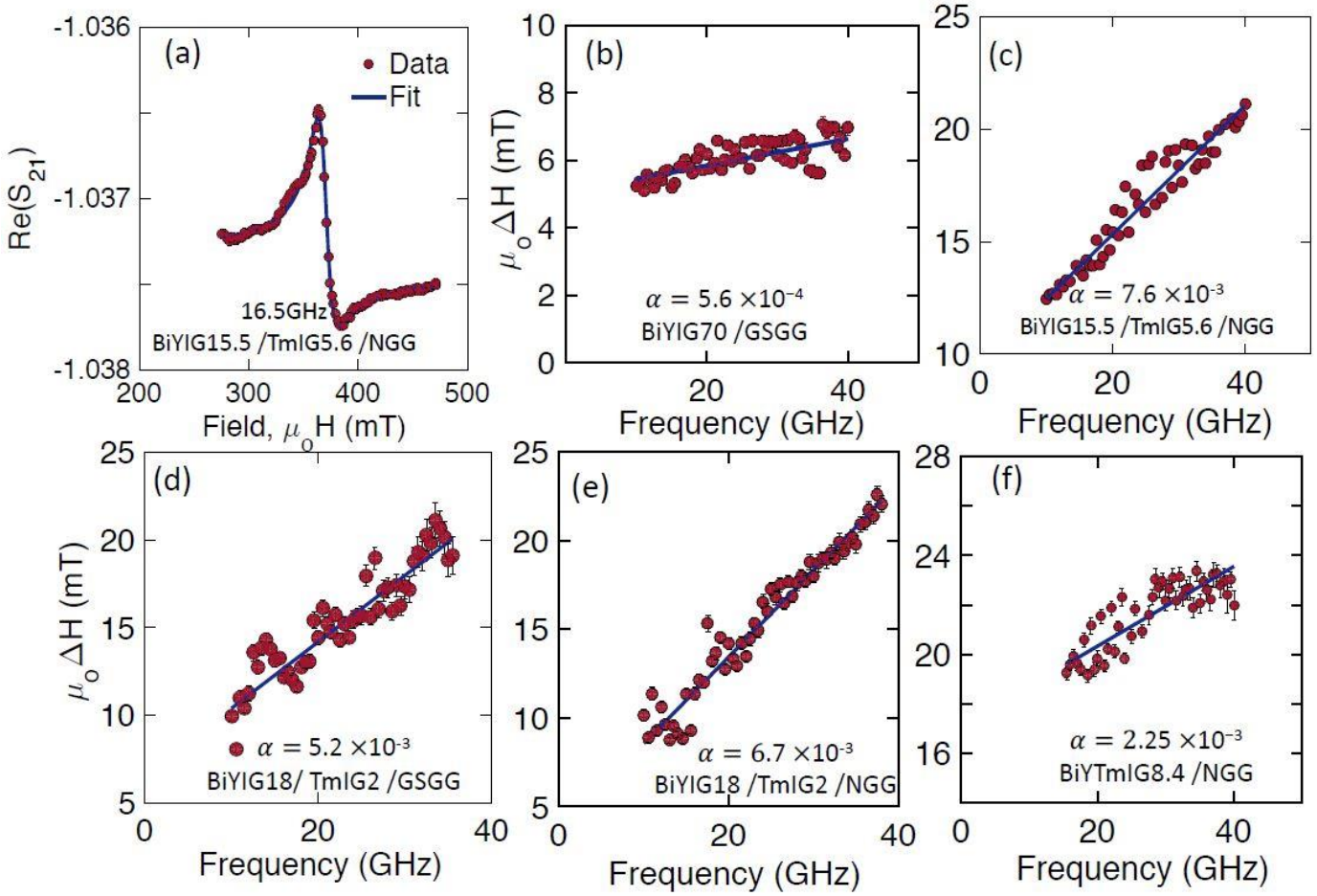

FIG 6.3 (a) A representative FMR spectrum taken at 16.5 GHz showing the real part of S_{21} for BiYIG (15.5 nm)/TmIG (5.6 nm)/NGG. Fits of linewidth, ΔH, as a function of frequency for (b) BiYIG (70 nm)/GSGG, (c) BiYIG (15.5 nm)/TmIG (5.6 nm)/NGG (d) BiYIG (18 nm)/TmIG (2 nm)/GSGG (e) BiYIG (18 nm)/TmIG (2 nm)/NGG (f) BiYTmIG (8.4 nm)/NGG with BiYIG:TmIG shot ratio of 25:2.

The damping was measured using broadband perpendicular ferromagnetic resonance (FMR) spectroscopy with a vector network analyzer (VNA) in the frequency range 10-40 GHz. [85–87,171] The complex transmission parameter S_{21} was measured at a particular frequency as the magnetic field was swept. [85] Damping α of the films was obtained by fitting FWHM linewidth ΔH to the following equation:

$$\Delta H = \frac{4\pi\alpha f}{|\gamma|\ \mu_0} + \Delta H_0 \qquad (6.2)$$

ΔH is obtained by fitting the S_{21} data to the complex susceptibility as shown in Fig. 3 (a). f is the excitation frequency, ΔH_0 is the inhomogeneous linewidth broadening and γ is the gyromagnetic ratio given by $(g\mu_B)/\hbar$ where μ_B is the Bohr magneton, $\hbar$ is the reduced Planck's constant and g is the Lande´ g-factor.

The linear fits obtained from $\Delta H(f)$ and the corresponding damping values for various bilayer and codeposited films are shown in Fig. 3. The data for a 70 nm thick BiYIG film deposited on a GSGG substrate from our previous work has been included for comparison. [29] Damping and ΔH_0 values for bilayered and codeposited films from this study are displayed in Table I. The data obtained from the codeposited film shows a less clear linear fit than that of the other films, but we nevertheless include its damping value in Table I. The damping of the bilayer films is between 5.2×10^{-3} and 7.6×10^{-3} with $\mu_0\Delta H_0$ of 4 - 9 mT. While these damping values are one order of magnitude higher than that of BiYIG, [29,119] they are still an order of magnitude lower than what has been reported for TmIG. [30,148,192] ΔH_0 values for TmIG/BiYIG bilayer films are also intermediate between those of BiYIG and TmIG. The codeposited BiYTmIG film, which contains a low fraction of Tm (with nominal composition of $Tm_{0.15}Bi_{0.75}Y_{2.1}Fe_5O_{12}$) has damping between that of the bilayers and that of BiYIG, but its $\mu_0\Delta H_0$ is higher.

The resonance field was fitted to the Kittel equation for perpendicular geometry: [85]

$$H_{res} = \frac{2\pi f}{|\gamma|\,\mu_0} + M_{eff} \qquad (6.3)$$

Here H_{res} is the resonance field, and M_{eff} is the effective magnetization. M_{eff} obtained from the fit was used to calculate the net anisotropy of these films K_u using the following equation:

$$K_u = \frac{-\mu_0 M_s M_{eff}}{2} \qquad (6.4)$$

Calculated K_u values for various films are displayed in Table I. All the films have positive K_u values indicating PMA in these films. This is consistent with the high remanence out-of-plane VSM hysteresis loops displayed in Fig. 2.

6.4 Measurements of DMI

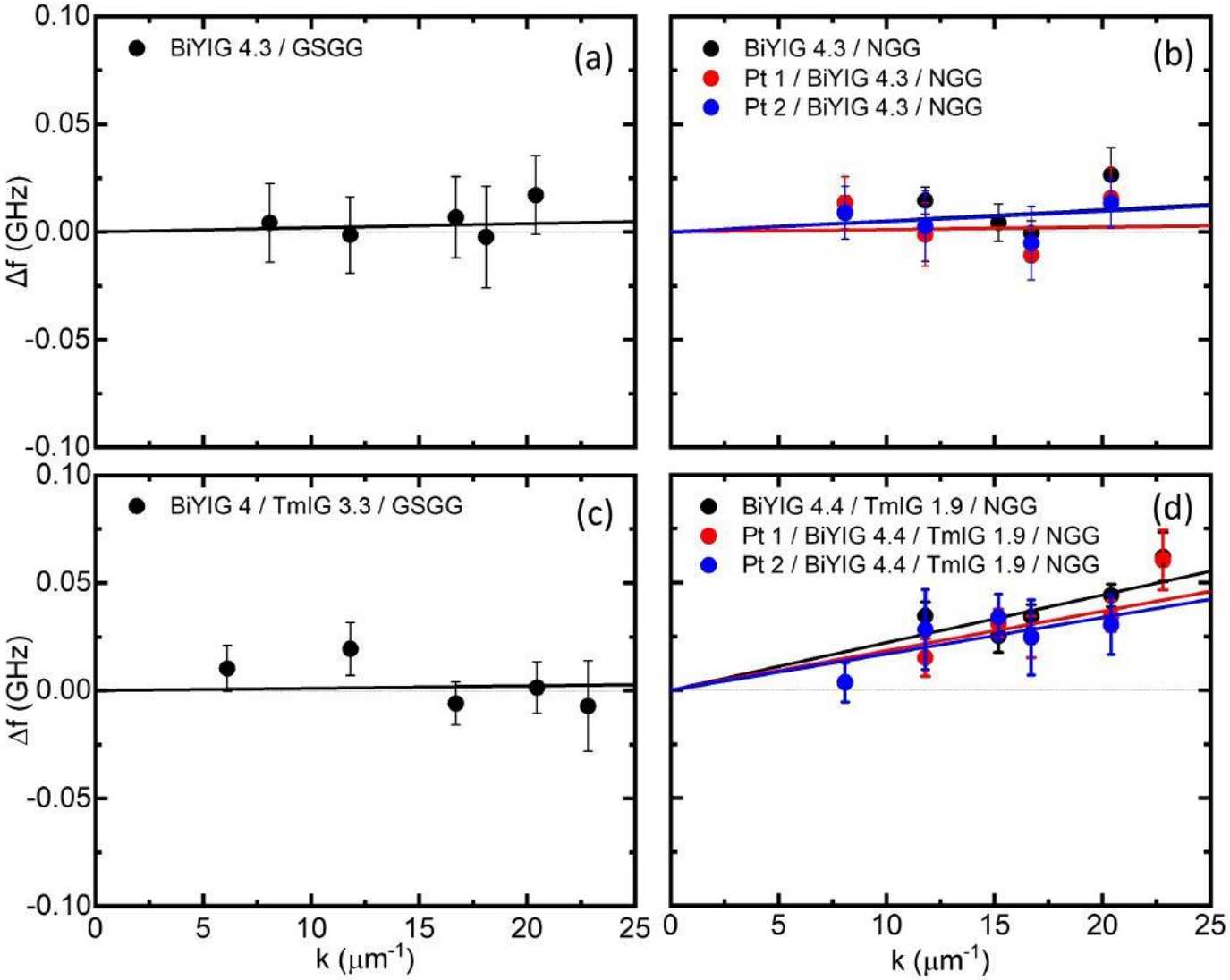

FIG 6.4 BLS frequency change Δf versus wavenumber k for (a) BiYIG (4.3 nm)/GSGG (b) BiYIG (4.3 nm)/NGG, Pt (1 nm)/ BiYIG (4.3 nm)/NGG, Pt (2 nm)/ BiYIG (4.3 nm)/NGG (c) BiYIG (4 nm)/TmIG (3.3 nm)/GSGG (d) BiYIG (4.4 nm)/TmIG (1.9 nm)/NGG, Pt (1 nm)/BiYIG (4.4 nm)/TmIG (1.9 nm)/NGG, Pt (2 nm)/BiYIG (4.4 nm)/TmIG (1.9 nm)/NGG.

Brillouin Light Scattering (BLS) measurements [90–92] were performed at room temperature in the Damon-Eshbach geometry [93,198] with an in-plane field of 5 kOe perpendicular to the spin wave propagation direction. For the DE mode, DMI provokes non-reciprocity in the counter-propagating DE mode frequencies, with frequencies given by: [91]

$$f_{DE}(\pm k) = f_0 \pm f_{DMI} = f_0 \pm \frac{\gamma D k}{\pi M_s} \qquad (6.5)$$

where f_0 is the DE mode frequency in the absence of DMI, k is the wavevector of the spin wave and D is the strength of the DMI. Then the frequency difference between Stokes and anti-Stokes peaks, $\Delta f = f(k) - f(-k)$ is measured as a function of wavevector, k. The D values for various films from this study were obtained by least-square fitting to $\Delta f = \frac{2\gamma D k}{\pi M_s}$, and are displayed in Table I.

Figure 6.4a,b indicates a lack of peak splitting and hence negligible DMI in BiYIG(4.3 nm)|GSGG and in BiYIG(4.3 nm)|NGG without a Pt overlayer and with a Pt overlayer of thickness 1 nm and 2 nm (their D values along with error bars displayed in Table I include the possibility that DMI is zero). These observations are consistent with prior results for BiYIG. [156] The paramagnetic substrates GSGG and NGG contain rare earths Gd^{3+} ($4f^7$, L = 0) and Nd^{3+} ($4f^3$, L = 6) respectively, but neither BiYIG sample yields DMI. The importance of orbital angular momentum for obtaining DMI in REIG films has been noted, [156] but here the Gd^{3+} has no orbital moment and the Nd^{3+} in the NGG substrate may be ineffective in promoting DMI due to the paramagnetic host.

The BiYIG|TmIG|GSGG bilayer film has no DMI, Fig. 4 (c), but BiYIG(4.4 nm)|TmIG(1.9 nm)|NGG without a Pt overlayer and with Pt of thickness 1 nm and 2 nm do exhibit DMI, Fig. 4 (d), of D = 0.0145 ± 0.0011 mJ/m^2. The critical D for stabilization of Néel domain walls is given by $(2t.ln(2)/\pi^2)\mu_0 M_s^2$ = 0.010 ± 0.003 mJ/m^2, where t is the thickness of the magnetic layer and M_s is its saturation

magnetization. [70] For BiYIG|TmIG|NGG this indicates that DMI is sufficient to stabilize Néel domain walls.

Considering the inverse dependence of interfacial DMI on thickness, the measured DMI is comparable to that of TbIG|Pt deposited on GGG and TmIG|Pt deposited on $Gd_3Ga_5O_{12}$ (GGG), NGG, and SGGG (composition $Gd_{2.6}Ca_{0.4}Ga_{4.1}Mg_{0.25}Zr_{0.65}O_{12}$) [70,93,186,187] but an order of magnitude lower than that of metallic ferrimagnetic [44] and metallic ferromagnetic thin films. [199,200]

Introducing 1.9 nm TmIG at the interface results in a DMI of BiYIG|TmIG bilayers consistent with that of single layers of TmIG based on domain wall depinning measurements, where 6.6 nm TmIG|NGG had $D = 0.007 \pm 0.0015$ mJ m^{-2} but TmIG|GSGG had $D = 0.0015 \pm 0.002$ mJ m^{-2}. [189] Xu et al. also demonstrated a dependence of DMI strength on substrate composition in TmIG|Pt heterostructures. [188] The codeposited BiYTmIG films did not show a measurable DMI, likely due to their low Tm content.

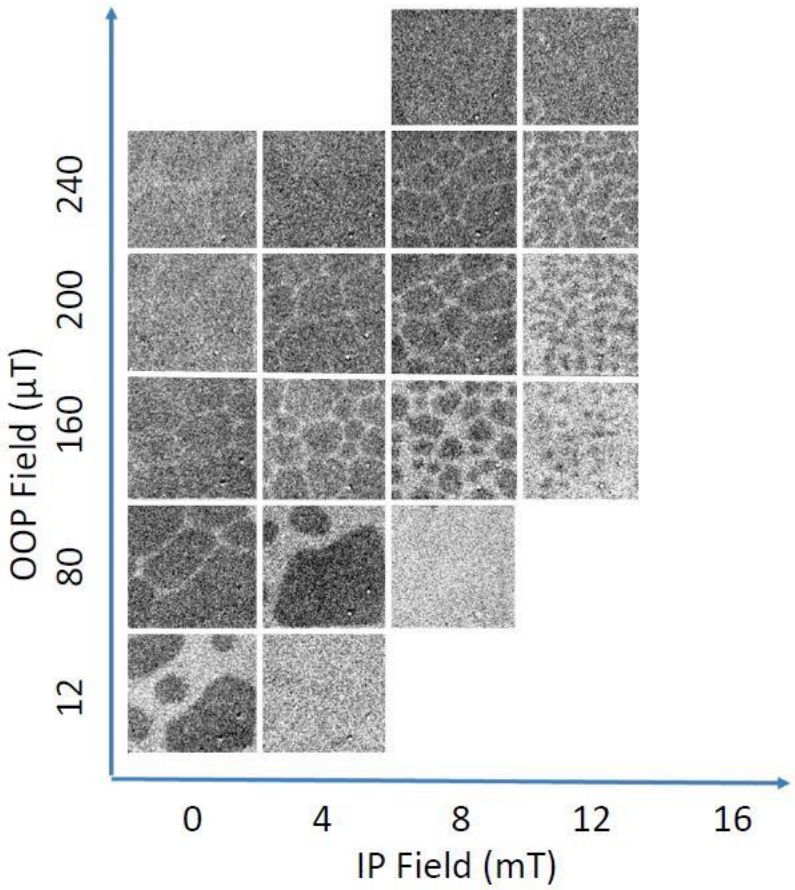

FIG 6.5 Domain structure of Pt(4 nm) /BiYIG(4 nm)/TmIG(3.5 nm)/GSGG for various values of in-plane field and out-of-plane field for a 100 μm × 100 μm area observed using MOKE microscope.

The domain structure of bilayer films was examined using MOKE. An in-plane field was able to generate bubble domains at room temperature in Pt(4 nm)|BiYIG(4 nm)|TmIG(3.5 nm)|GSGG. Combinations of in-plane and out-of-plane fields were able to tune the bubble domain size over a wide range as shown in Figure 6.5. The domains changed their sizes within small IP and OP field ranges indicating high domain wall mobility. Due to the low DMI for this sample, these bubble domains are unlikely to be DMI stabilized skyrmions. We were unable to observe bubble domains in bilayered films deposited on NGG.

Table 6.1: Gilbert damping and D values for various films

Stack	K_u (kJ/m^3)	Gilbert Damping	Inhomogeneous Linewidth Broadening $\mu_0\Delta H_0$ (mT)	D ($mJ\ m^{-2}$)
BiYIG (70 nm)/GSGG	8.8 ± 0.7	$5.6 \pm 0.7 \times 10^{-4}$	5 ± 0.1	n/a
BiYIG (4.3 nm)/GSGG	n/a	n/a	n/a	0.001 ± 0.002
BiYIG(4.3 nm)/NGG	n/a	n/a	n/a	0.003 ± 0.002
Pt(1 nm)/BiYIG(4.3 nm)/NGG	n/a	n/a	n/a	0.003 ± 0.018
Pt(2 nm)/BiYIG(4.3 nm)/NGG	n/a	n/a	n/a	0.001 ± 0.001
BiYTmIG (8.4 nm)/NGG (BiYIG:TmIG shot ratio of 25:2)	8.6 ± 1.2	$2.25 \pm 0.2 \times 10^{-3}$	17 ± 0.5	n/a
BiYIG (15.5 nm)/TmIG (5.6 nm)/NGG	11.6 ± 1.6	$7.6 \pm 0.27 \times 10^{-3}$	9.2 ± 0.5	n/a
BiYIG (18 nm)/TmIG (2 nm)/GSGG	8.4 ± 1.1	$5.2 \pm 0.32 \times 10^{-3}$	6.6 ± 0.5	n/a
BiYIG (18 nm)/TmIG (2 nm)/NGG	5.7 ± 0.8	$6.7 \pm 0.21 \times 10^{-3}$	3.7 ± 0.4	n/a
BiYIG (4 nm)/TmIG (3.3 nm)/GSGG	n/a	n/a	n/a	0.001 ± 0.003
BiYIG (4.4 nm)/TmIG (1.9 nm)/NGG	4.6 ± 0.6	n/a	n/a	0.014 ± 0.002
Pt(1 nm)/BiYIG (4.4 nm)/TmIG (1.9 nm)/NGG	n/a	n/a	n/a	0.011 ± 0.003
Pt(2 nm)/BiYIG (4.4 nm)/TmIG (1.9 nm)/NGG	n/a	n/a	n/a	0.011 ± 0.001

6.5 Conclusions

The Gilbert damping and DMI strength of epitaxial BiYIG, codeposited BiYTmIG and bilayered BiYIG|TmIG films deposited on (111) GSGG and NGG substrates were investigated with the aim of

identifying a path to develop films with low damping, high DMI and PMA. The films exhibit PMA with high remanence, attributed to magnetoelastic and growth-induced anisotropy, and show bubble domains with field-tunable size.

BiYIG|TmIG bilayers have a damping value 10x higher than that of BiYIG but 10x lower than that of single layer TmIG. Additionally, their inhomogeneous linewidth broadening was lower than that reported for TmIG. BiYIG|TmIG|NGG has D = 0.0145 ± 0.0011 mJ/m^2, but BiYIG|TmIG|GSGG had no DMI. This indicates a dependence of DMI strength on substrate composition, as seen for single layer TmIG films where TmIG|NGG had higher DMI than TmIG|GSGG. [189] BiYIG|GSGG and BiYIG|NGG films had no DMI, consistent with other measurements. BiYIG|TmIG|NGG therefore provides a compromise, exhibiting PMA, DMI and a damping that is an order of magnitude lower than that of TmIG. This work suggests that bilayers or multilayers of garnets provide opportunities to engineer combinations of magnetic properties that are not available from single layer garnet films.

6.6 Methods

Target fabrication, thin film deposition and characterization: Precursor powders with the stoichiometric element ratios of the final target composition ($Bi_{0.8}Y_{2.2}Fe_5O_{12}$) were mixed and ball milled with yttrium stabilized zirconia grinding media for 24 hours in ethanol. The mixture was then dried and calcinated in a tube furnace in air to form the desired phase. Then the calcinated powders were uniaxial and cold isostatic pressed at 40,000 psi for 2 min into a 1.1" diameter pellet. Finally, the pellet was transferred to a tube furnace and sintered to form the BiYIG target.

BiYIG, BiYTmIG and TmIG|BiYIG films were grown by pulsed laser deposition (PLD) on (111) oriented garnet substrates of composition $Gd_3Sc_2Ga_3O_{12}$ (GSGG) and $Nd_3Ga_5O_{12}$ (NGG). The targets used for deposition had compositions of $Bi_{0.8}Y_{2.2}Fe_5O_{12}$ and $Tm_3Fe_5O_{12}$. Prior to introducing oxygen and deposition of films, the chamber was pumped down to 5×10^{-6} Torr base pressure. A laser repetition rate of 10 Hz, laser fluence of 2 J/cm^2 and target-substrate distance of 6 cm were used. For the TmIG|BiYIG

bilayer growth the O_2 pressure was 150 mTorr and the substrate temperature was 560° C and 720°C during the deposition of BiYIG and TmIG layers respectively. For the codeposited BiYTmIG films the O_2 pressure was 150 mTorr and the substrate temperature was 560° C. An O_2 pressure of 230 Torr was maintained in chamber as the samples cooled down after growth.

An ultrahigh vacuum magnetron sputtering system with Ar pressure of 2 mTorr was used for Pt deposition at room temperature. A Bruker D8 Discover HRXRD was used to perform HRXRD measurements. An ADE 1660 VSM was used to perform magnetic measurements. A custom-built, wide-field Kerr microscope with independent out-of-plane and in-plane magnetic field control was used to perform polar MOKE measurements to observe domains. Kohler illumination was adopted with a ×10 objective and a 456.6 nm wavelength LED light source.

Ferromagnetic resonance (FMR): The vector network analyzer (VNA) technique was used to perform broadband perpendicular FMR spectroscopy. The samples were placed face-down on a 50 Ω coplanar waveguide. The films were saturated in the out-of-plane direction by sweeping an out-of-plane magnetic field up to $\mu_0 H = 2.2$ T. Microwave transmission over a frequency from 10 to 40 GHz was measured with a variable microwave field applied in-plane.

Brillouin light scattering (BLS): Due to the interfacial nature of DMI and its inverse dependence on film thickness, films with thickness lower than 10 nm were used for the BLS measurements, whereas thicker films were used for damping measurements by FMR. The BLS measurements were performed in backscattering geometry using a (3+3) tandem Fabry-Pérot interferometer and 532 nm continuous-wave laser of 532 nm wavelength. The thermally generated Damon-Eshbach mode is measured with in-plane applied field of 0.5 T. The wavevector of the DE mode is then determined by the angle θ between the film normal and incident laser, given by $k = \frac{4\pi}{\lambda} sin\Theta$. Each Stokes and anti-Stokes frequency is obtained from the Voigt fitting of the BLS spectra. Voigt fit and Lorentzian fits for the experimental data yield similar values for frequency, but the Voigt fit resulted in a lower error bar.

Contributors:
Film deposition, XRD and VSM measurements were performed jointly by Takian Fakhrul and author of this thesis. FMR measurements were performed by Hans Nembach. BLS measurements were performed by Byung Hun Lee. Observation of bubble domains using MOKE was performed by Siying Huang.

Chapter 7: Rare earth iron garnet superlattices with sub-unit-cell composition modulation

7.1 Introduction

Complex oxide heterostructures exhibit fascinating emergent phenomena driven by the broken symmetry, structural distortions and charge transfer that occur at oxide interfaces. Examples include the 2D electron gases or magnetic moments that appear at interfaces between otherwise insulating and nonmagnetic perovskites $LaAlO_3$ and $SrTiO_3$ [201], improper ferroelectricity in $PbTiO_3/SrTiO_3$ perovskite superlattices [202], anomalous spin-glass transitions in superlattices of magnetically-frustrated $ZnCr_2O_4/ZnFe_2O_4$ spinels [203], and metallicity in rutile-structured TiO_2/IrO_2 superlattices [204]. Garnets, with formula $A_3B_2C_3O_{12}$, have three different types of cation sites in the b.c.c. unit cell, enabling an even greater range of compositional variation than in perovskites, ABO_3. Moreover, iron garnets in particular ($A_3Fe_5O_{12}$) are ferrimagnetic insulators with a high Curie temperature of 560 K, and their magnetooptical properties, low damping, and high domain wall velocities make them essential components of a range of microwave, magnetic and photonic devices [205–207]. Other garnets have applications in lasing materials (e.g. aluminum garnets) and as ionic conductors (Li-stuffed garnets) [208–210].

In rare earth iron garnets ($RE_3Fe_5O_{12}$, REIG) the RE ion has fundamental importance in determining the magnetic anisotropy, magnetostriction, magnetic moment, compensation temperature, damping, and optical properties of the garnet [26,40,211]. As a perovskite analogy, in rare earth nickelates ($RENiO_3$), changing the RE leads to a dramatic change in electronic and magnetic properties [212], and in rare earth orthoferrites ($REFeO_3$), the RE determines the Néel temperature and spin reorientation of the Fe sublattice and drives improper ferroelectricity [213–216]. A variety of studies have demonstrated growth of perovskite and spinel superlattices [203,217–221], including orthoferrite or nickelate superlattices with intriguing properties [222–224]. Therefore, we might expect RE garnet multilayers to provide a rich opportunity for materials engineering, where interfacial strain and composition gradients and the loss of inversion symmetry could drive

piezomagnetic [225] or flexomagnetic [226,227] effects, growth-induced anisotropy [29,141], Dyaloshinskii-Moriya interactions or a ferroelectric response [74].

Despite the exceptional properties of garnets and the opportunities inherent in interface engineering, there has been little study of garnet heterostructures and multilayers. Garnet superlattices of $Y_3Fe_5O_{12}$/$Bi_3Fe_5O_{12}$ (YIG/BiIG), YIG/$(EuBi)_3Fe_5O_{12}$, YIG/$Gd_3Fe_5O_{12}$, and $(Bi,Dy)_3(Fe,Ga)_5O_{12}$/ $(Bi,Lu)_3(Fe,Al)_5O_{12}$ with layer thicknesses of tens to hundreds of nm were synthesized for magneto-optical and optical applications such as Bragg reflectors [194,195,228,229]. The study of garnet superlattices with nm-scale layer thicknesses is restricted to YIG/$Gd_3Ga_5O_{12}$ (GGG) with minimum layer thickness of one unit cell (cubic lattice parameter a = 1.2 nm) [230], GGG/$Gd_3Sc_2Ga_3O_{12}$ (GSGG) with layers of ~2 nm [221] and YIG/GGG/$Ca_3Sc_2Si_2TiO_{12}$ with each layer 3.5 nm thick [219,231–234]. Structural characterization is limited, and the only magnetic component is YIG.

Here we describe the structure and magnetic properties of coherent superlattices made from terbium iron garnet (TbIG, $Tb_3Fe_5O_{12}$), europium iron garnet (EuIG, $Eu_3Fe_5O_{12}$), and thulium iron garnet (TmIG, $Tm_3Fe_5O_{12}$) and from lutetium iron garnet (LuIG, $Lu_3Fe_5O_{12}$) and bismuth iron garnet (BiIG). Unlike prior work, all layers are ferrimagnetic and the composition modulation involves only the dodecahedral sites. Compositionally modulated layers of 0.45 nm, half the out-of-plane lattice spacing, are confirmed both by elemental analysis of a EuIG/TmIG superlattice and from the magnetic anisotropy of a TbIG/TmIG superlattice, which differs qualitatively from that of the solid solution $(Tb_{0.5}Tm_{0.5})_3Fe_5O_{12}$. LuIG/BiIG superlattices exhibit ferromagnetic resonance linewidths characteristic of the end-member BiIG, and not the solid solution. These findings demonstrate the engineering of garnet multilayers with layering at a sub-unit cell scale, providing opportunities to explore interfacial phenomena in iron garnets with tunable magnetic and spintronic properties.

7.2 Results

The superlattices in this study, summarized in Table 1 (Supplementary Note 1), were deposited by pulsed laser deposition (PLD) on GGG and GSGG substrates at oxygen pressures of 50-150 mTorr, a substrate temperature of 650˚ C and a laser repetition rate of 10 Hz (Methods). Superlattices of total thickness 15-44 nm consisting of 2-56 individual layers were formed by ablating from targets of the end-members (TbIG, TmIG, EuIG, LuIG, BiIG) based on the deposition rate established from each target. In contrast, a substitutional solid solution film, $(Tb_{0.5}Tm_{0.5})_3Fe_5O_{12}$ (TbTmIG) or $(Lu_{0.5}Bi_{0.5})_3Fe_5O_{12}$ (LuBiIG) was formed when the number of shots per layer is low enough to allow complete intermixing of the species.

Fig. 1 reveals direct evidence of superlattice formation from transmission electron microscopy (TEM) high-angle annular dark-field (HAADF) imaging and 3D atom probe tomography (APT). A cross-section of the 44 nm thick, 16 layered TbIG/TmIG film on (111) GGG and its energy dispersive spectroscopy (EDS) map (Figs. 1a,b and Supplementary Note 2) reveal a coherent, compositionally-modulated superlattice with layer thicknesses of 2.8 nm in which the transition between the layers occurs within an interfacial width below 1 nm. No dislocations are present within the image area and the film is fully strained to the substrate, consistent with the epitaxial growth of a variety of single-layer iron garnet films with thicknesses of up to 90 nm on garnet substrates [102,120]. A separate TbIG/TmIG sample made with various layer thicknesses, analyzed via APT (Fig. 1c, Methods) also shows interface widths below 1 nm. The RE:Fe cation stoichiometry was close to its bulk value of 3:5 for TbIG and TmIG layers of 4.5 nm and 3.2 nm respectively (Supplementary Note 1). A TmIG/EuIG film on (110) GGG (Fig. 1d,e) imaged along the $[\bar{1}11]$ in-plane zone axis exhibits layers of 0.45 nm thickness, half the out-of-plane spacing of $a/\sqrt{2}$.

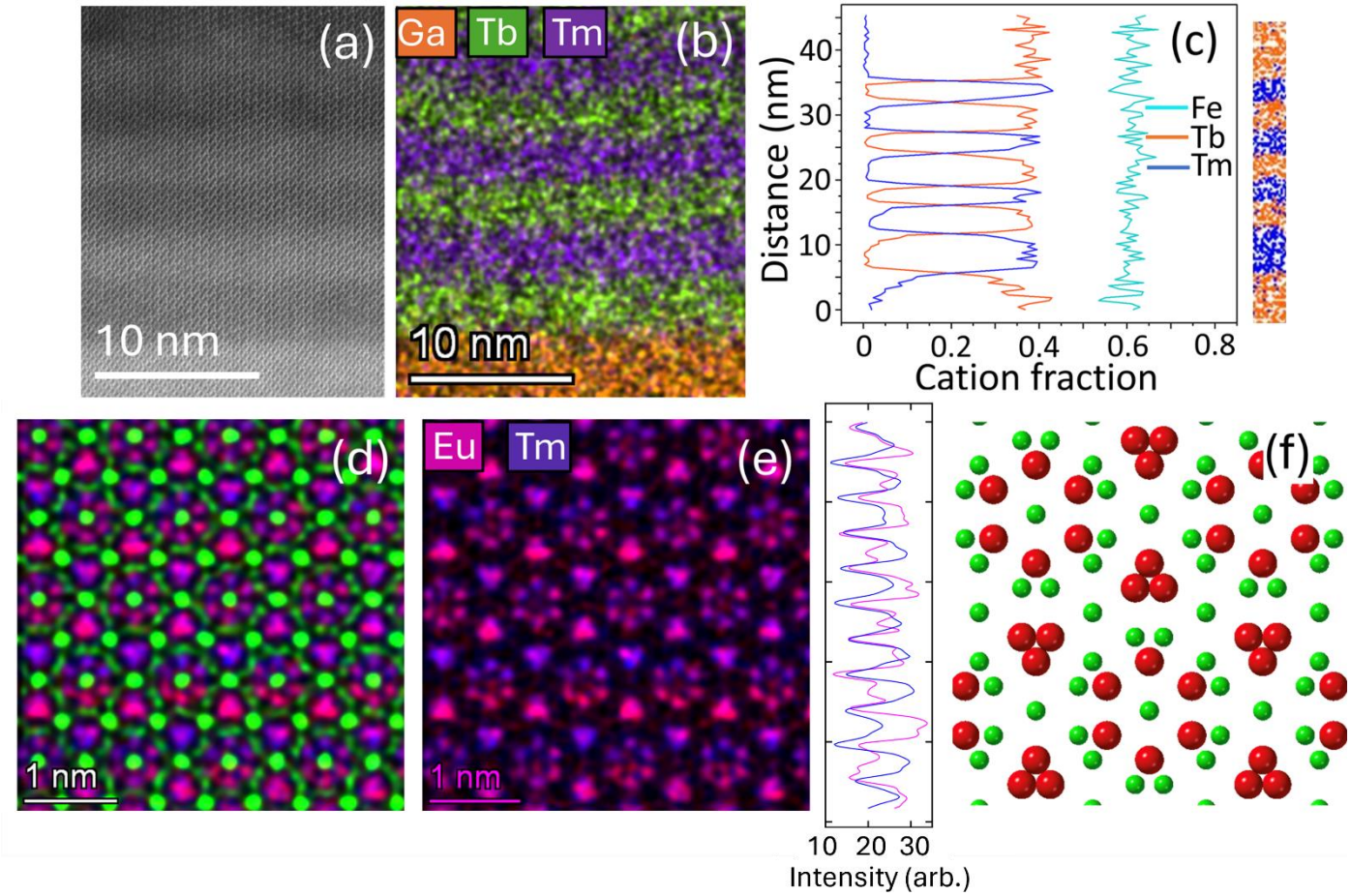

FIG. 7.1 Superlattice garnet films. (a) HAADF image for a cross-section of a 16 layered (TbIG/TmIG)/(111)GGG superlattice with overall thickness of 44 nm along a [1$\bar{1}$0] zone axis. (b) TEM EDS map for the sample in (a). (c) Projected 2D image for APT data for a (TbIG/TmIG)/(111)GGG multilayered film with different layer thicknesses of TbIG and TmIG. In the inset image, each dot represents the position of the ion detected by mass spectrometry. (d,e) Elemental maps of a superlattice of EuIG-TmIG grown on a (110) substrate imaged along the [$\bar{1}$11] in-plane zone axis. Fe is shown in green in (d), Eu in magneta and Tm in purple. (f) Crystal structure of REIG along the [111] zone axis showing the Fe (green) and RE (red) sites, matching the arrangement seen in (d,e).

TEM and APT, as well as atomic force microscopy (Supplementary Notes 2, 3) show that while multilayers initially grow with a smooth surface (e.g. r.m.s. roughness of 0.2 nm for a 15 nm thick film, Fig. S4b) roughness develops in multilayers grown at 150 mTorr when the thickness exceeds ~25 nm, Fig. S4a, corresponding to waviness in the compositionally modulated layers. Roughness was suppressed by growing the films at 50 mTorr (Fig. S4c), suggesting that it is promoted by the lower mobility conditions present during deposition at high oxygen pressures.

Considering the in-plane lattice match to the substrate, symmetric high resolution x-ray diffraction (HRXRD) scans of single-layer films TbIG, TmIG and TbTmIG, Figure 2a, show that the TbIG is under in-plane compressive strain and the TmIG under tension, whereas the TbTmIG displays little strain. For a multilayer film consisting of thick layers, e.g. 22 nm, the HRXRD scans (Fig. 2b and Supplementary Note 4) resemble a superposition of peaks corresponding to the single-layer TbIG and TmIG films. However, for multilayer films consisting of thinner layers, multiple peaks occur at positions different from those of the end member peaks, including satellite peaks on either side of the main peak. XRD modeling of TbIG/TmIG multilayers with a finite number of layers, Fig. 2c, yields a good agreement with the measured spectra, further supporting the existence of a superlattice. Multilayer films made at lower oxygen pressure exhibit more prominent fringes indicating reduced roughness and greater thickness uniformity (Fig. S7).

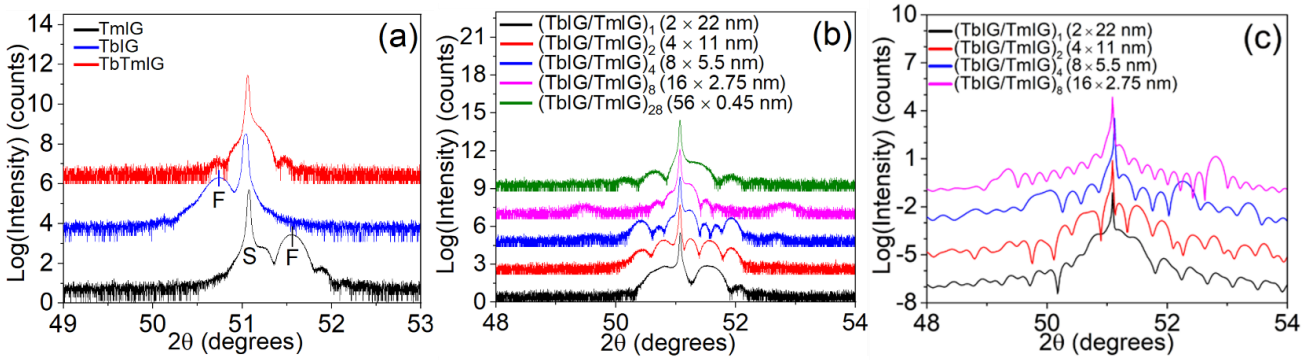

FIG. 7.2 X-ray diffraction of garnet films. (a) HRXRD scans of TmIG, TbIG and TbTmIG films deposited on GGG substrates with (111) orientation (vertically offset for clarity with film and substrate peaks labeled F and S, respectively). (b) HRXRD scans of bilayered, 4 layered, 8 layered, 16 layered and 56 layered films of (TbIG/TmIG)/(111)GGG (vertically offset for clarity). (c) Simulation of XRD scans for bilayered, 4 layered, 8 layered and 16 layered films of (TbIG/TmIG)/(111)GGG with total thickness of 44 nm.

Hysteresis loops from vibrating sample magnetometry (VSM), Fig. 3 and Supplementary Note 5, show an out-of-plane easy axis for the TbIG and TmIG films and the TbIG/TmIG superlattices on (111) GGG substrates, whereas the solid solution TbTmIG film and superlattices grown on (100)-oriented GGG and (111)-oriented GSGG have an in-plane easy axis. To analyse these differences we consider

the net anisotropy, K_{eff}, defined as the difference in energy between the magnetization being oriented in-plane vs. out-of-plane. For (111)-oriented iron garnet films [102,120,141]:

$$K_{eff} = \frac{-K_1}{12} - \frac{\mu_0}{2} M_s^2 + \frac{9}{4} c_{44} \lambda_{111} \left(\frac{\pi}{2} - \beta\right) + K_G + K_I. \qquad (7.1)$$

Here K_1 is the first order cubic magnetocrystalline anisotropy constant, which is small compared to other terms; M_s is the saturation magnetization of the film, c_{44} is the shear modulus of the film, λ_{111} is the magnetostriction coefficient, β is the corner angle of the rhombohedrally distorted unit cell, K_G is the uniaxial growth induced anisotropy [140,141,184] originating from the preferential occupancy of cations or vacancies in nonequivalent sites and K_I captures any interfacial contributions to anisotropy [235,236]. A positive K_{eff} results in an out-of-plane easy axis, i.e. perpendicular magnetic anisotropy (PMA).

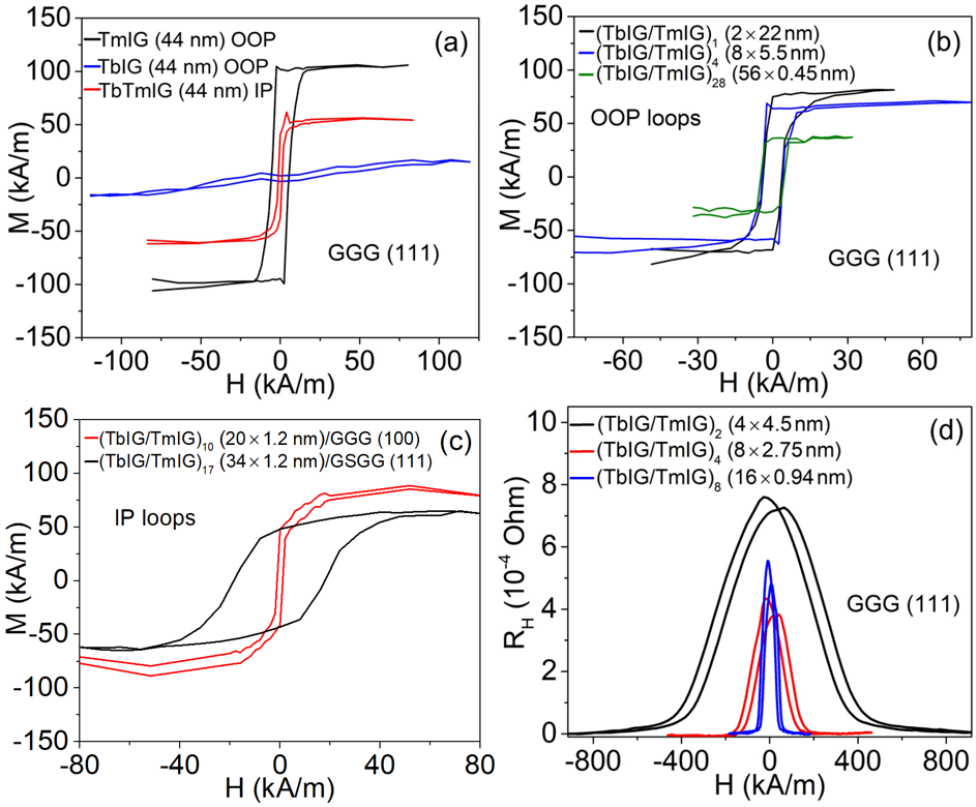

FIG. 7.3 (a) VSM hysteresis loops of TmIG, TbIG and TbTmIG films deposited on GGG substrates with (111) orientation. (b) VSM hysteresis loops of bilayered, 8 layered and 56 layered films

(TbIG/TmIG)/(111)GGG with overall thickness of 44 nm or 25 nm. (c) VSM hysteresis loops of 20 layered (TbIG/TmIG) deposited on GGG substrate with (100) orientation and 34 layered (TbIG/TmIG) deposited on GSGG substrate with (111) orientation with thicknesses of 24 nm and 41 nm respectively. (d) In-plane SMR loops for 4 layered, 8 layered and 16 layered (TbIG/TmIG)/(111)GGG with and overall thicknesses of 18 nm, 22 nm and 15 nm respectively deposited on GGG substrates with (111) orientation.

The PMA of the TmIG film (in-plane tensile strain; λ_{111} = -5.2 × 10^{-6}) and the TbIG film (in-plane compressive strain; λ_{111} = +12 × 10^{-6}) originates from their dominant magnetoelastic energy contributions [138]. In contrast, the TbTmIG solid solution has little strain and an interpolated λ_{111} = +3.4 × 10^{-6}, hence the magnetoelastic energy term is small. The in-plane easy axis indicates that any perpendicular growth-induced or surface anisotropy is insufficient to overcome the dominant shape anisotropy of $-\frac{\mu_0}{2}M_S^2$. Therefore, the presence of PMA in the multilayer films is an indication that they are not intermixed, but instead consist of layers that retain the magnetic characteristics of the end-members. In particular, the PMA of the 56-layer 25 nm thick TbIG/TmIG superlattice, which is qualitatively different from the in-plane easy axis of the TbTmIG solid solution, indicates that a composition modulation exists for TbIG/TmIG layers of 0.45 nm.

Multilayers were also deposited onto other substrates: (111)-oriented GSGG, which has a larger lattice parameter than GGG, and (001)-oriented GGG. First, considering films on (111) GSGG, based on the strain state and magnetostriction we expect a TmIG film to have PMA but TbIG and TbTmIG to have in-plane anisotropy. A TbIG/TmIG superlattice on (111) GSGG showed an in-plane easy axis (Fig. 3c), which is consistent with its having a multilayer structure but it is also consistent with intermixing to form a solid solution TbTmIG (Supplementary Note 7). Next, for a film on a (100) oriented substrate, analogously to Eq. 1 the anisotropy is given by [120]:

$$K_{eff,100} = \frac{3}{2}\lambda_{100}(c_{11} - c_{12})(\varepsilon_{zz} - \varepsilon_{xx}) - \frac{\mu_0}{2}M_S^2 + K_G + K_I \,. \qquad (7.2)$$

Here λ_{100} is the magnetostriction coefficient along <100>, c_{11} and c_{12} are elastic constants of the film material and ε_{ii} denotes the i^{th} normal strain component. The in-plane easy axis observed for the

TbIG/TmIG superlattice on (100) GGG (Fig. 3c) is consistent with behavior expected from a multilayer, but also with a solid solution (Supplementary Note 8). Therefore, unlike the (111) GGG substrate, neither (111) GSGG nor (100) GGG substrates enable us to distinguish between a TbIG/TmIG multilayer and a TbTmIG solid solution based solely on the direction of the easy axis.

We quantify the anisotropy of the TbIG/TmIG/(111)GGG superlattices and TbTmIG/(111)GGG solid solution using spin-Hall magnetoresistance (SMR) measurements of films with thickness below 22 nm and a root mean square roughness below 0.2 nm. A 4 nm thick Pt layer was sputtered onto the films and patterned into Hall crosses, and the anisotropy field H_K and net anisotropy $K_{eff} = \mu_0 M_s H_K/2$ were determined from the SMR (Methods). Fig. 3d shows that K_{eff} decreased as the layer thickness decreased, from 13.8 ± 1.9 kJ/m^3 for 4.5 nm layers to 1.9 ± 0.3 J/m^3 for 0.94 nm layers, i.e. the PMA becomes weaker as the layers become thinner. We attribute this to the increasing volume fraction of interfaces. The TbTmIG solid solution has an in-plane easy axis with K_{eff} = -3.8 ± 0.3 kJ/m^3, dominated by shape anisotropy of -2.5 kJ/m^3. The interfacial regions of the superlattice with their intermediate composition are similarly expected to contribute an in-plane anisotropy, and a higher density of interfaces therefore lowers the net PMA of the superlattice (Supplementary Note 9).

We now turn to superlattices of BiIG and LuIG, comparing single-layer films of BiIG (39 nm thickness), LuIG (35 nm thickness) and solid solution LuBiIG (21 nm thickness) with a BiIG/LuIG multilayer with 3 nm layers (35 nm thickness) on (111) GGG. While BiIG is not a stable phase in bulk, it crystallizes on a garnet substrate as an epitaxial thin film with lattice parameter 1.263 nm [237]. From XRD, Fig. 4a, epitaxial BiIG on GGG exhibits an in-plane compressive strain, whereas LuIG on GGG is in tension, and LuBiIG is under a smaller compressive strain.

Fig. 4b shows that BiIG, LuIG, LuBiIG and the BiIG/LuIG multilayer all have an in-plane easy axis of magnetization with M_s = 135 ± 15 kA/m, similar to the bulk magnetization of IGs with nonmagnetic

c-site ions including LuIG, YIG and BiYIG [29,138]. The net anisotropy, Lande g-factor and linewidth were measured by ferromagnetic resonance (FMR) [238–240] at 5 - 17 GHz, Fig. 4c. The net anisotropy from FMR for all four films (Supplementary Table S2, S3) indicates an in-plane easy axis in agreement with Fig. 4b, and the g-factor was close to 2 as expected for Fe^{3+} [241].

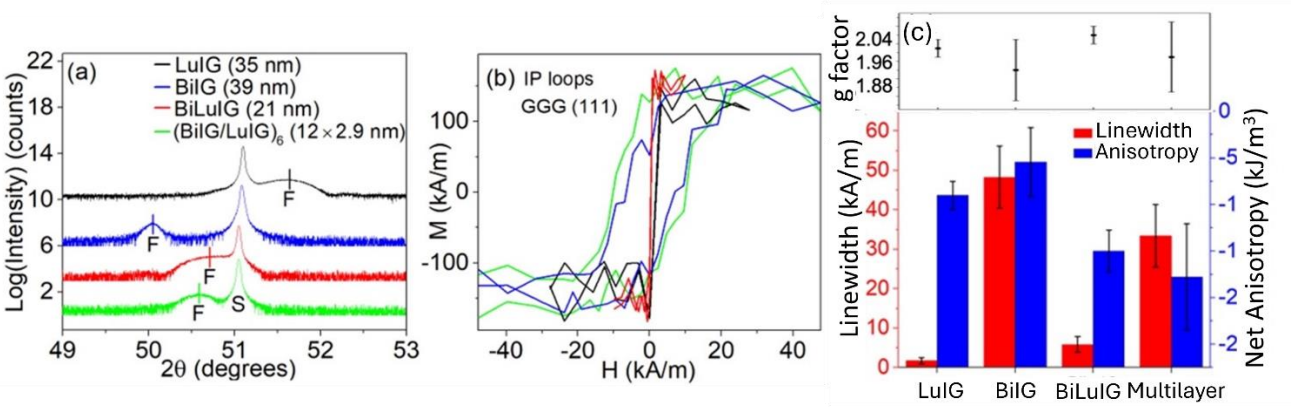

FIG. 7.4 (a) HRXRD scans of LuIG, BiIG, BiLuIG and BiIG/LuIG 12 layered films with thicknesses of 35 nm, 39 nm, 21 nm and 35 nm respectively deposited on GGG substrates with (111) orientation (vertically offset for clarity, with film and substrate peaks labeled F and S, respectively). (b) In-plane VSM hysteresis loops for the the films in (a). (c) Lande g-factor, FMR linewidth at 8 GHz frequency of ac magnetic field and net anisotropy of the films in (a).

Subtracting the shape anisotropy, the remaining anisotropy (sum of magnetoelastic, magnetocrystalline, growth and interfacial contributions) of the films is given in Supplementary Table S4. This is positive for LuIG and BiIG (i.e. favoring PMA) and negative for LuBiIG and the BiIG/LuIG multilayer. For the LuIG film, assuming the dominant term is magnetoelastic, we obtain $\lambda_{111} = -2.5 \times 10^{-6} \pm 1.5 \times 10^{-6}$, which is similar to the value for bulk YIG (-2.7×10^{-6}). An analogous calculation for BiIG yields a positive λ_{111} which is inconsistent with prior reports [54], suggesting instead that the PMA in BiIG is dominated by another mechanism such as growth-induced ordering of point defects. The LuBiIG and the BiIG/LuIG multilayer have similar anisotropy values (within the error bar); in each the magnetoelastic anisotropy is small and the in-plane anisotropy may originate from growth-induced or interfacial anisotropy.

Although the anisotropy and magnetization of the LuBiIG and the BiIG/LuIG multilayer are similar, their FMR linewidths are dramatically different. The BiIG film and the multilayer both have much greater linewidth (48 kA/m and 33 kA/m respectively at 8 GHz) compared to the LuIG and BiLuIG (1.7 kA/m and 5.8 kA/m respectively). The high linewidths associated with BiIG may be a result of defects in the metastable compound [242,243]. The high linewidth of the BiIG/LuIG multilayer is consistent with the presence of BiIG, implying a composition modulation within the film.

7.3 Discussion

We have demonstrated the synthesis of coherent superlattices of a complex oxide, iron garnet. Remarkably, a composition modulation in the c-site cation can be obtained for layer thicknesses of 0.45 nm, less than half of the lattice parameter. Superlattice formation is revealed directly by compositional mapping using both electron microscopy and atom probe tomography and by x-ray diffraction, and is inferred from the magnetic properties of the films. In particular, TbIG/TmIG superlattices with layers of 0.45 nm and above show perpendicular magnetic anisotropy in common with the end members TmIG and TbIG, dominated by magnetoelastic anisotropy, whereas a solid solution TbTmIG has an in-plane easy axis as a result of its low strain and low magnetostriction. Furthermore, LuIG/BiIG with 3 nm layer thicknesses has a high FMR linewidth in common with that of the end member BiIG, whereas the solid solution LuBiIG has a low linewidth.

Oxide heterostructures exhibit a wealth of useful and fascinating physical and electronic properties that emerge from gradients and asymmetry in strain, composition and charge transfer at interfaces. However, work to date has primarily focussed on perovskites. The garnet heterostructures demonstrated here provide an even greater range of compositional parameters resulting from the three different cation sites present in the crystal. The ability to modulate the composition on a sub-unit-cell lengthscale offers unprecedented opportunities for manipulating the electronic and magnetic properties of an important class of materials and revealing new interfacial phenomena.

7.4 Methods

Films were grown by pulsed laser deposition on GGG substrates with (111) and (100) orientation and on GSGG substrates with (111) orientation (MTI, Inc.). Commercially available TbIG ($Tb_3Fe_5O_{12}$), TmIG ($Tm_3Fe_5O_{12}$), EuIG ($Eu_3Fe_5O_{12}$), BiIG ($Bi_3Fe_5O_{12}$) and LuIG ($Lu_3Fe_5O_{12}$) targets with purity above 99.9% were used for PLD in a Neocera chamber with a Compex Pro laser of 248 nm wavelength, fluence of 2.0 J/cm^2, repetition rate of 10 Hz and oxygen partial pressure of 150 mTorr. TbIG, EuIG and TmIG were deposited in one chamber on substrates heated to 650 ˚ C (heater setpoint temperature of 900 ˚ C) while a different chamber was used for deposition of BiIG and LuIG with a substrate temperature of 550 ˚ C (heater setpoint of 700 ˚ C). The deposited films were cooled down to room temperature at a rate of 20 ˚ C/min in an oxygen pressure of 150 mTorr. A Bruker D8 Discover HRXRD was used to perform HRXRD measurements. XRD scans for multilayered films were simulated using LEPTOS. Each layer was assumed to be perfectly crystalline with the composition of the end member, and all layers were assumed to be strained in-plane to match the substrate lattice parameter. Interfaces were assumed to have an abrupt composition change from one end member to the other without any intermixing between layers. Topographical images of the film surface were obtained using an AFM model Cypher S. An ADE 1660 VSM was used to perform magnetic measurements.

The TEM lamella sample was prepared by VELION FIB-SEM system, with Au^+ ion beam working at 35 keV, followed by ion polishing by Ar^+. The HAADF and EDS images were acquired on a Themis Z STEM working at 200 keV with chromatic corrector. Specimen tips for the 3D APT were prepared using an FEI Helios 660 Nanolab Dual-Beam FIB/SEM. Standard APT sample preparation procedures were followed for the lift out; sharpening of the tips was performed first with an ion beam accelerating voltage of 30 kV, and then (for final shaping and cleanup) at 2 kV. APT was performed using a Cameca LEAP 4000X HR instrument in laser pulsing mode, with the following operating conditions: laser

pulse energy of 20 pJ and repetition rate of 100 kHz; base temperature of 40 K; detection rate of 1%. Reconstruction and analysis of the data was performed using Cameca IVAS 3.6.14 software. A 1D concentration profile along a cylindrical sub-volume parallel to the long axis of the specimen tip was extracted; the ion counts were converted into cation ratios. The accurate oxygen content cannot be determined via APT because oxygen field-evaporates as both O^+ and O_2^{++}, which have the same mass-to-charge-ratio. The thickness calibration was obtained from HRXRD analysis.

Ferromagnetic resonance (FMR) [238–240] measurements were performed to determine the net anisotropy of the films using a broadband FMR system with a coplanar waveguide. An r.f. magnetic field of f = 5 GHz to 17 GHz was applied perpendicular to the film while an in-plane dc magnetic field $\mu_0 H$ was swept from 0 to 0.6 T. The resonance field H_{res} and linewidth ΔH were determined for each frequency by fitting the detected voltage with the derivative of sum of a symmetric and antisymmetric Lorentzian [88]:

$$P = \frac{d}{dH}\left[\frac{S\,\Delta H^2 + A_s(H - H_{res})}{4(H - H_{res})^2 + \Delta H^2}\right] \qquad (7.3)$$

Here S and A_s are arbitrary fitting constants. The Lande g-factor and M_{eff} were obtained for all films by fitting the frequency of ac magnetic field f and H_{res} to the following equation [89]:

$$f = \frac{g\,\mu_0\mu_B}{2\pi\hbar}\sqrt{H_{res}(H_{res} + M_{eff})} \qquad (7.4)$$

Spin Hall magnetoresistance was measured by first depositing 4 nm Pt on top of the garnet film using RF magnetron sputtering with Ar pressure of 2 mTorr. The 22 nm thick films show PMA and similar hysteresis to that of the thicker multilayered films but have a root mean square roughness below 0.2 nm. The Pt/REIG longitudinal and Hall resistance are measured by wire bonding at the corners of a continuous square film sample in a Van der Pauw-Hall geometry. The magnetic field was applied by a solenoid coil magnet and the resistance was measured by standard low frequency lock-in amplifiers.

An electric current in the Pt layer produces a spin current perpendicular to the film plane by the spin-Hall effect (SHE) [241] which interacts with the REIG magnetization and modulates the resistivity of the Pt [94,95]. The transverse Hall resistance is given by:

$$R_H = R_H^{SMR} sin^2\Theta \sin(2\Phi) + R_H^{AHE,SMR} \cos\Theta + R_H^{OHE} H_z \qquad (7.5)$$

Here, Θ and Φ are the polar and azimuthal angles of the magnetization respectively. R_H^{SMR}, $R_H^{AHE,SMR}$ and R_H^{OHE} are manifestations of the SMR, anomalous Hall effect-like SMR and ordinary Hall effect (OHE) respectively and H_z is the applied out-of-plane magnetic field. For films with PMA we apply an in-plane magnetic field at 45˚ to the current direction and measure $H_{K,eff}$, the field required to saturate R_H, using a standard lock-in technique with Van der Pauw method [244] and fitting the data to a macrospin model.

Contributors:

TEM images were collected by Allison Kaczmarek and Tingyu Su. APT data was collected by Katharina Lasinger. SMR measurements were performed by Chung-Tao Chou. FMR measurements were performed by David Bono. Deposition of films at oxygen partial pressure of 100 mTorr and 50 mTorr and their characterization was performed by Tomas Grossmark.

Supplementary Information for Chapter 7

Note 1: Data Tables

Table S1: List of samples (all films were deposited at oxygen partial pressure of 150 mTorr unless stated otherwise)

Sample	**Layer 1**	**Layer 2**	**Laser shots**	**Layer 1 thickness, nm**	**Layer 2 thickness, nm**	**Film thickness, nm**	**Substrate**
Single layers							
TmIG	-	-	18800	-	-	44	(111) GGG
TbIG	-	-	20800	-	-	44	(111) GGG
$Tb_{0.5}Tm_{0.5}IG$	-	-	(94 + 104) × 100	-	-	44	(111) GGG
LuIG	-	-	56200	-	-	35	(111) GGG
BiIG	-	-	18800	-	-	39	(111) GGG
$Bi_{0.5}Lu_{0.5}IG$	-	-	(94 + 28) × 180	-	-	21	(111) GGG
Superlattices							
2 layer	TmIG	TbIG	(9400 + 10400) × 1	22	22	44	(111) GGG
4 layer	TmIG	TbIG	(4700 + 5200) × 2	11	11	44	(111) GGG
8 layer	TmIG	TbIG	(2350 + 2600) × 4	5.5	5.5	44	(111) GGG
16 layer	TmIG	TbIG	(1175 + 1300) × 8	2.8	2.8	44	(111) GGG
56 layer	TmIG	TbIG	(191 + 211) × 28	0.45	0.45	25	(111) GGG
20 layer	TmIG	TbIG	(513 + 567) × 10	1.2	1.2	24	(100) GGG
34 layer	TmIG	TbIG	(515 + 570) × 17	1.2	1.2	41	(111) GSGG
4 layer	TmIG	TbIG	(1923 + 2127) × 2	4.5	4.5	18	(111) GGG
8 layer	TmIG	TbIG	(1176 + 1301) × 4	2.8	2.8	22	(111) GGG
16 layer	TmIG	TbIG	(401 + 444) × 8	0.94	0.94	15	(111) GGG
10 layer	TmIG	TbIG	(1000 + 1000) × 5	2.3	2.3	23	(111) GGG
10 layer (100 mTorr)	TmIG	TbIG	(1000 + 1000) × 5	2	2	20	(111) GGG
10 layer (50 mTorr)	TmIG	TbIG	(1000 + 1000) × 5	3.3	3.3	33	(111) GGG
40 layer (50 mTorr)	TmIG	TbIG	(250 + 250) × 20	0.5	0.5	20	(111) GGG
12 layer	LuIG	BiIG	(4683 + 1406) × 6	2.9	2.9	35	(111) GGG

Table S2: Structure and Magnetic properties of samples (all films were deposited at oxygen partial pressure of 150 mTorr unless stated otherwise)

Sample	Layer thick-ness, nm	Film thick-ness, nm	beta angle	Substrate	Average M_s (kA/m)	Easy axis coercivity (kA/m)	Net anisotropy (kJ m^{-3})	Linewidth (kA/m)	g-factor
Single layers									
TmIG	-	44	90.33°	(111) GGG	103 ± 10	5.5 ± 0.5	-	-	-
TbIG	-	44	89.79°	(111) GGG	16 ± 10	-	-	-	-
$Tb_{0.5}Tm_{0.5}IG$	-	44	90.0°	(111) GGG	58 ± 10	1 ± 0.5	-3.8 ± 0.3	-	-
LuIG	-	35	90.34°	(111) GGG	135 ± 15	10 ± 1	-5.4 ± 3.7	1.7 ± 0.8	1.99 ± 0.02
BiIG	-	39	89.26°	(111) GGG	135 ± 15	7 ± 1	-9.0 ± 1.5	49 ± 8	1.94 ± 0.07
$Bi_{0.5}Lu_{0.5}IG$	-	21	89.8°	(111) GGG	135 ± 15	< 1	-15.0 ± 2.2	5.8 ± 2	2.02 ± 0.02

Superlattices									
TmIG/TbIG bilayer	22	44	-	(111) GGG	72 ± 10	4 ± 0.5	-	-	-
4 layer	11	44	-	(111) GGG	84 ± 10	16 ± 1	-	-	-
8 layer	5.5	44	-	(111) GGG	67 ± 10	4 ± 0.5	-	-	-
16 layer	2.8	44	-	(111) GGG	63 ± 10	13.5 ± 1	-	-	-
56 layer	0.4	25	-	(111) GGG	35 ± 10	5 ± 0.5	-	-	-
20 layer	1.2	24	-	(100) GGG	85 ± 10	1 ± 0.5	-	-	-
34 layer	1.2	41	-	(111) GSGG	63 ± 10	18 ± 1	-	-	-
4 layer	4.5	18	-	(111) GGG	-	-	13.8 ± 1.9	-	-
8 layer	2.8	22	-	(111) GGG	-	-	5 ± 0.8	-	-
16 layer	0.9	15	-	(111) GGG	-	-	1.9 ± 0.3	-	-
10 layer	2.3	23	-	(111) GGG	29.3 ± 4.2	19.3 ± 4	-	-	-
10 layer (100 mTorr)	2	20	-	(111) GGG	43.1 ± 1.7	1.9 ± 0.4	-	-	-
10 layer (50 mTorr)	3.3	33	-	(111) GGG	51.5 ± 1.1	0.3 ± 0.2	-	-	-
40 layer (50 mTorr)	0.5	20	-	(111) GGG	43.8 ± 2.3	0.7 ± 0.2	-	-	-
LuIG/BiIG 12 layer	2.9	35	-	(111) GGG	135 ± 15	< 1	-17.8 ± 5.7	32.5 ± 8	1.97 ± 0.08

The error estimates for saturation magnetization values were obtained from the noise of the VSM hysteresis loops. Errors for coercivity are based on the field step size used for VSM measurements. For TmIG/TbIG multilayer films, errors for net anisotropy values are based on errors for saturation magnetization values and errors for anisotropy field values extracted from fitting the SMR data. For all films of the LuIG – BiIG system, errors for net anisotropy values are based on errors for saturation magnetization values and errors for effective magnetization values extracted from fitting the FMR data. Errors for linewidth values are based on the field step size used for FMR measurements. Errors for g-factor are extracted from fitting FMR data.

Table S3: Effective magnetic anisotropy, shape anisotropy and K_{eff} - K_{shape} for BiIG and LuIG films.

Film on (111) GGG substrate	K_{eff} (kJ/m^3)	K_{shape} (kJ/m^3) for M_s = 135 kA/m	$K_{magnetoelastic} + K_{growth} + K_{interfacial}$ (kJ/m^3)
BiIG 39 nm	-5.5 ± 3.7	-11.5	6.0 ± 3.7
LuIG 35 nm	-9.0 ± 1.5	-11.5	2.4 ± 1.5
BiLuIG 21 nm	-15.0 ± 2.3	-11.5	-3.5 ± 2.3
$(BiIG/LuIG)_6$ 35 nm	-18.0 ± 5.7	-11.5	-6.6 ± 5.7

Errors for net anisotropy values are based on errors for saturation magnetization values and errors for effective magnetization values extracted from fitting FMR data.

Table S4: Composition measurements by atom probe tomography

Sample	RE:Fe ratio
TbIG	0.33:0.67 (± 0.01)
TmIG	0.38:0.62 (± 0.01)

The extracted cation fractions for both RE elements and for iron are in good agreement with the expected values, i.e. 3/8 = 0.375 for the RE elements and 5/8 = 0.625 for iron.

Note 2: Microstructure and composition of multilayered films

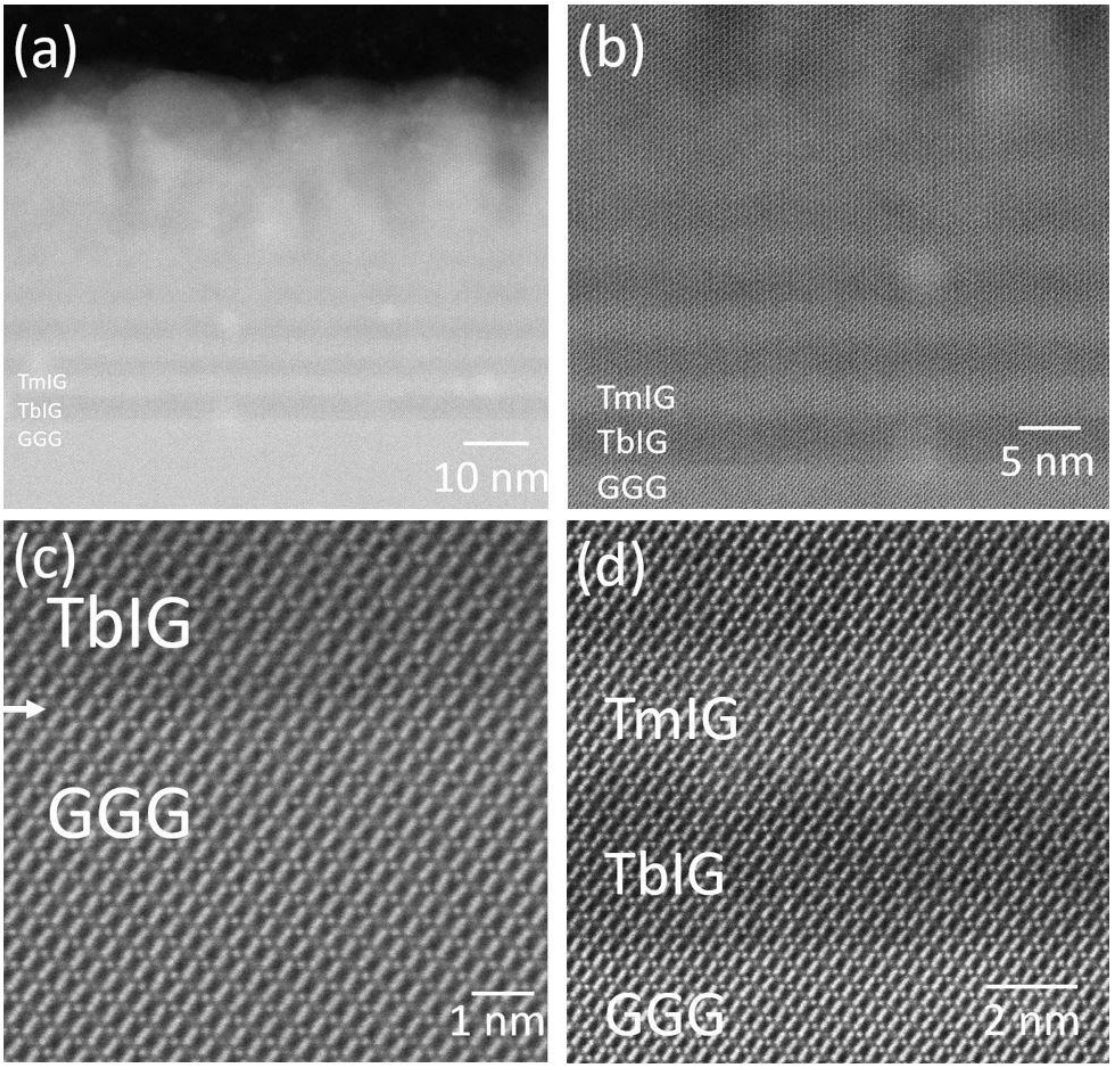

FIG. S1. HAADF images for a cross-section of a 16 layered film of (TbIG/TmIG)/(111)GGG with total thickness of 44 nm at different magnifications. In c) the interface is indicated with a white arrow.

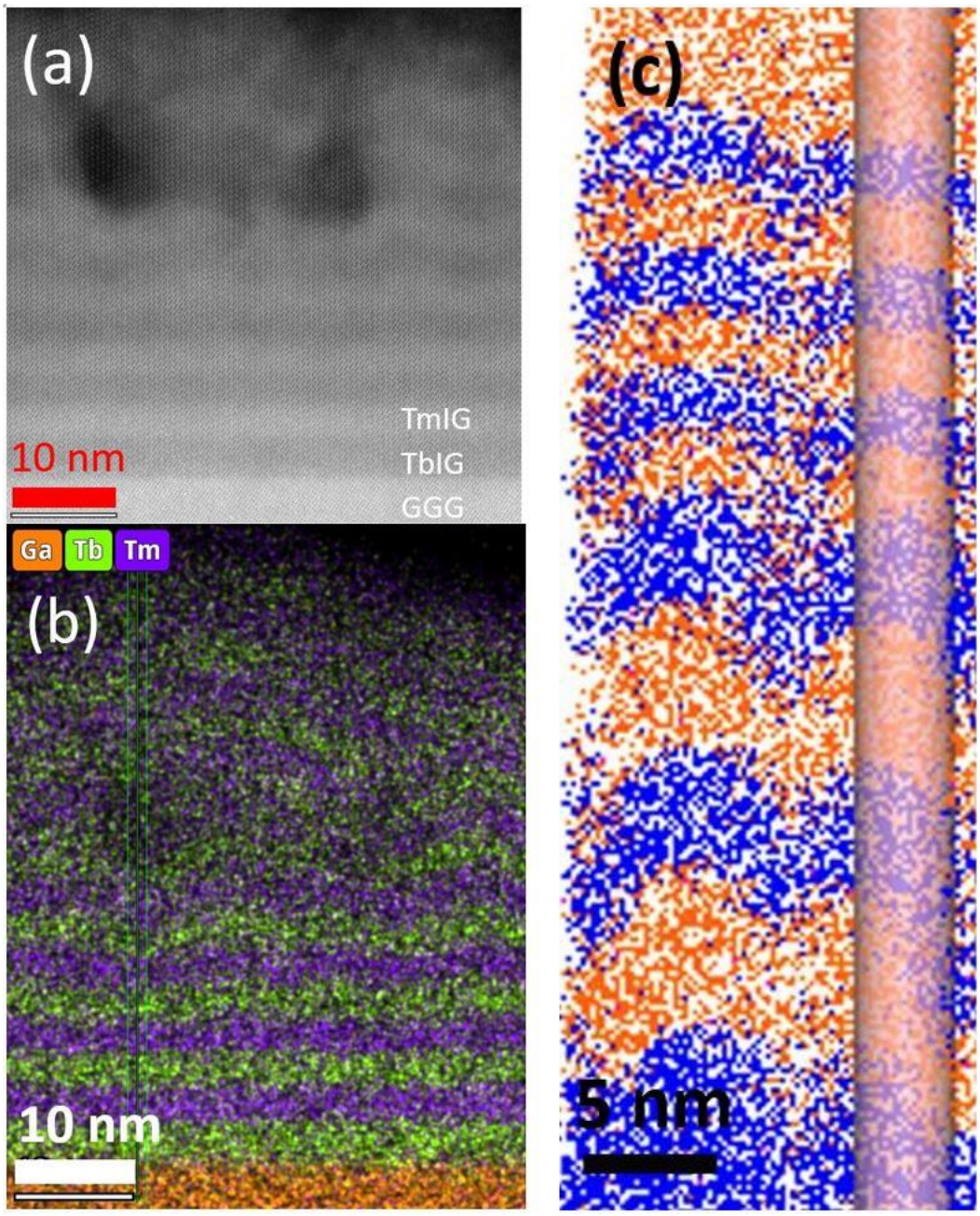

FIG. S2. Transmission electron microscopy (TEM) images and atom probe tomography (APT) images showing development of roughness in a TbIG/TmIG multilayer grown at 150 mTorr.

(a) HAADF image for a cross-section of a 16 layered film of (TbIG/TmIG)/(111)GGG with total thickness of 44 nm. (b) Corresponding EDS map. The layers are still present in the upper region of the film, but exhibit waviness when the thickness exceeds ~25 nm. (c) Projected 2D image for APT data for a (TbIG/TmIG)/(111)GGG with

different layer thicknesses. Each dot represents the position of an ion detected by mass spectrometry. The shaded region on the right represents the cylindrical volume of the data used to determine the composition profiles in the main text, Figure 1(c).

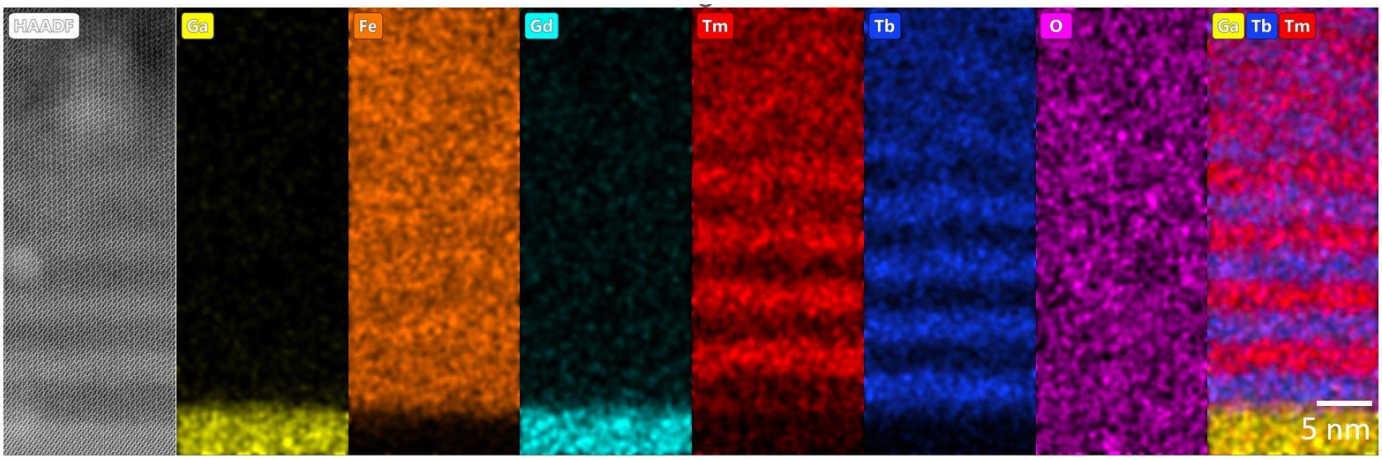

FIG. S3. Composition measurements. HAADF image and EDS maps for a cross-section of a 16 layered film of (TbIG/TmIG)/(111)GGG with total thickness of 44 nm.

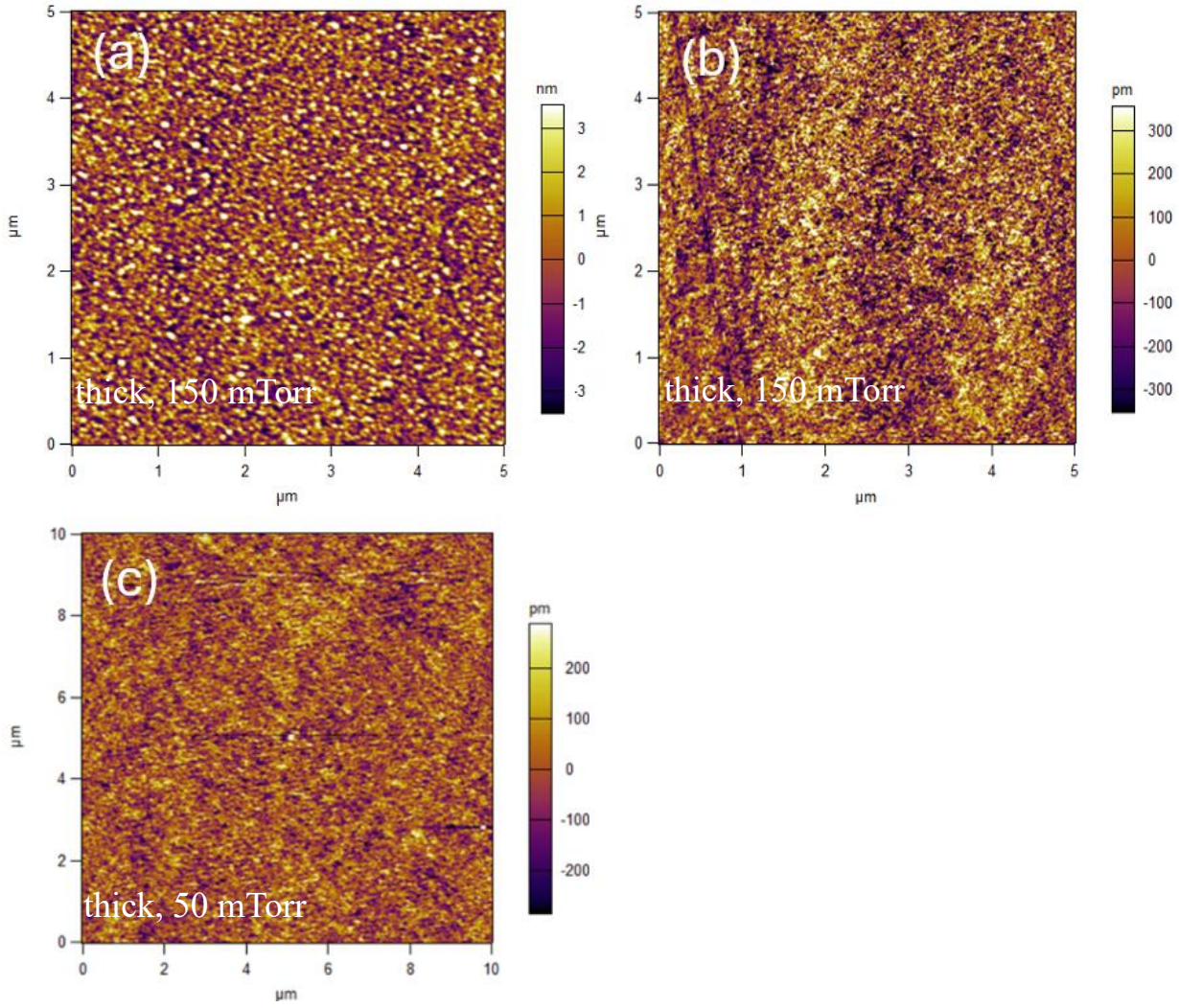

FIG. S4. Atomic force microscopy (AFM) images of TmIG/TbIG multilayers deposited on (111) GGG substrates. AFM scans for (a) 4 layered film with overall thickness of 44 nm and RMS surface roughness of 1.5 nm and (b) 16 layered film with overall thickness of 15 nm and RMS surface roughness of 0.2 nm. (a) and (b) were deposited at oxygen pressure of 150 mTorr. (c) 10 layered film with overall thickness of 33 nm and RMS surface roughness of 0.1 nm deposited at oxygen pressure of 50 mTorr. Note the different height scales for the three samples.

Note 3: Atom probe tomography of a sample with different layer sequences

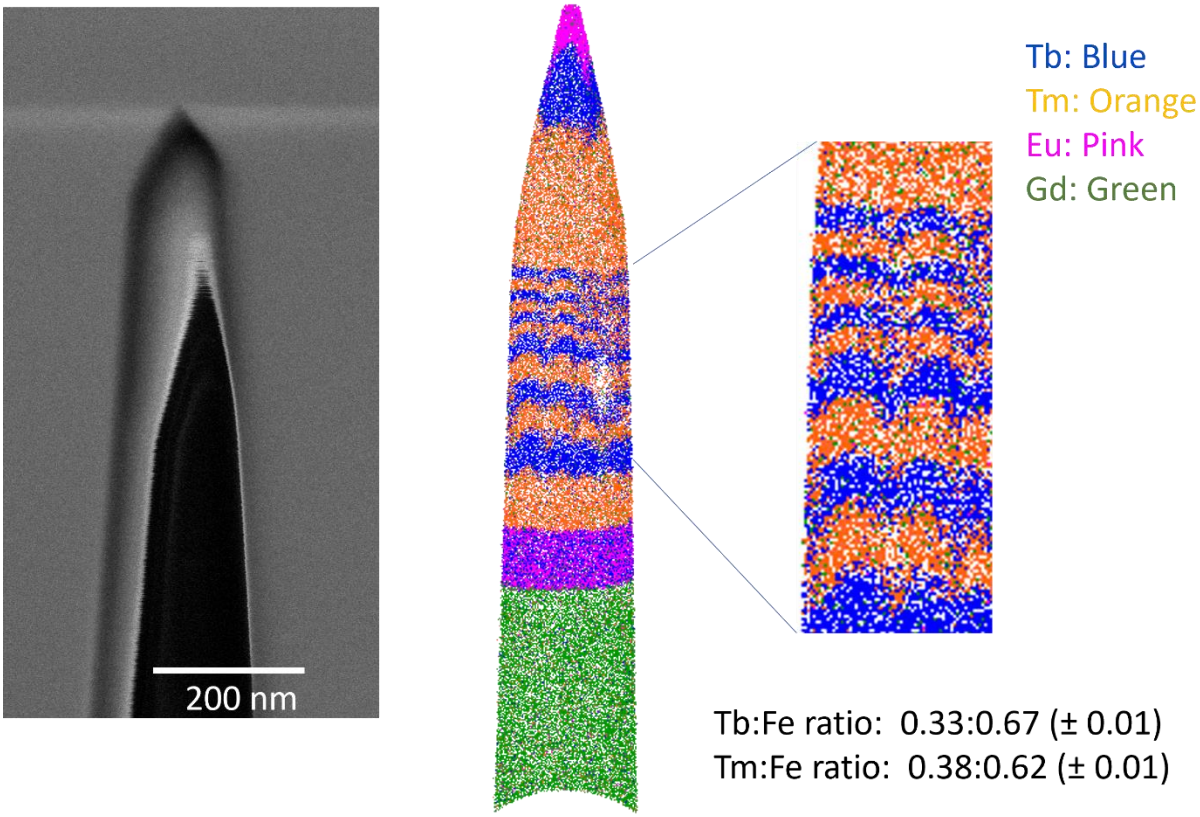

FIG. S5. Atom probe tomography. Left: The APT sample prepared by focussed ion beam from a multilayered iron garnet film deposited on a GGG substrate with (111) orientation, which included EuIG, TbIG and TmIG layers of various thickness. Center: composition map (rare-earth ion is specified by color). Development of roughness can be observed with increasing film thickness.

Note 4: Symmetric HRXRD scans of films

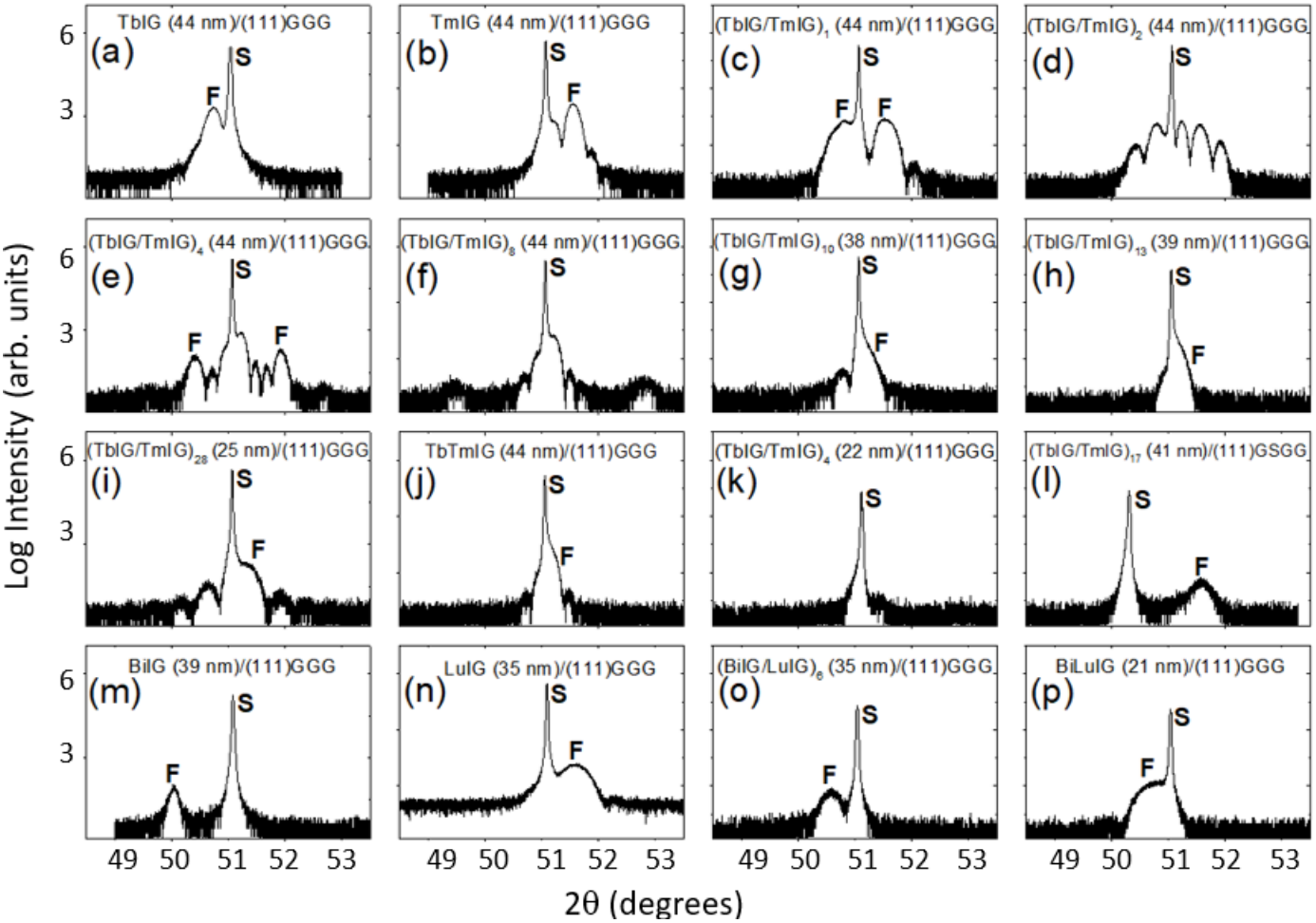

FIG. S6. Symmetric HRXRD scans around the substrate (444) peaks. Substrate peaks are indicated by S and film peaks are indicated by F. All samples were deposited at oxygen pressure of 150 mTorr.

(a) GGG|TbIG (44 nm)
(b) GGG|TmIG (44 nm)
(c) GGG|Bilayer TbIG/TmIG, thickness 44 nm
(d) GGG|4 layered TbIG/TmIG film with overall thickness 44 nm
(e) GGG|8 layered TbIG/TmIG film with overall thickness 44 nm
(f) GGG|16 layered TbIG/TmIG film with overall thickness 44 nm
(g) GGG|20 layered TbIG/TmIG film with overall thickness 38 nm
(h) GGG|26 layered TbIG/TmIG film with overall thickness 39 nm
(i) GGG|56 layered TbIG/TmIG film with overall thickness 25 nm
(j) GGG|Solid solution TbTmIG film (44 nm)
(k) GGG|8 layered TbIG/TmIG film with overall thickness 22 nm
(l) GSGG|34 layered TbIG/TmIG film with overall thickness 41 nm
(m) GGG|BiIG (39 nm)
(n) GGG|LuIG (35 nm)
(o) GGG|12 layered BiIG/LuIG film with overall thickness 35 nm
(p) GGG| Solid solution BiLuIG (21 nm).

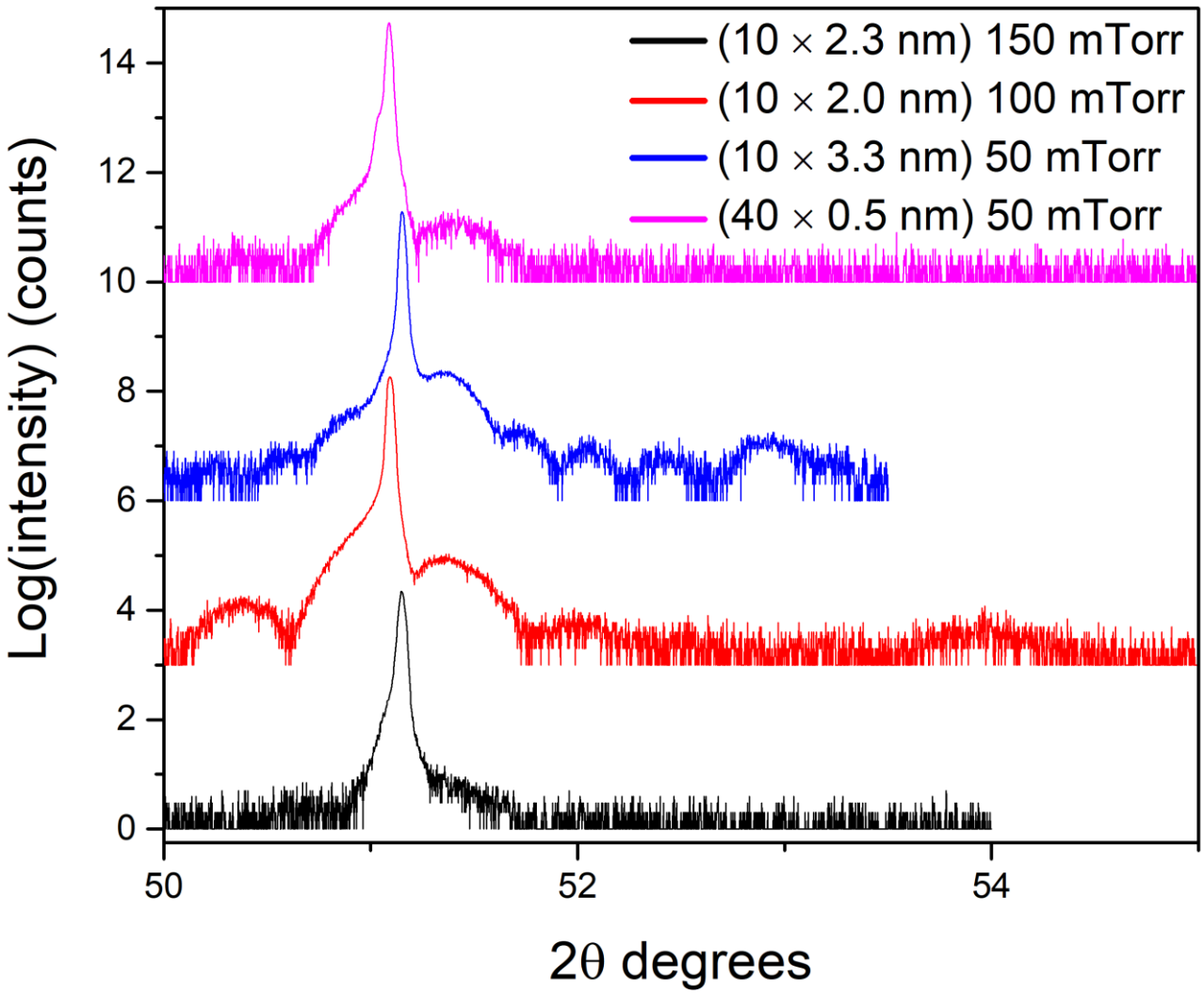

FIG. S7. Symmetric HRXRD scans around substrate (444) peaks for GGG|10 layered TbIG/TmIG film with thickness 23 nm deposited at oxygen pressure of 150 mTorr, GGG|10 layered TbIG/TmIG film with thickness 20 nm deposited at oxygen pressure of 100 mTorr, GGG|10 layered TbIG/TmIG film with thickness 33 nm deposited at oxygen pressure of 50 mTorr and GGG|40 layered TbIG/TmIG film with thickness 20 nm deposited at oxygen pressure of 50 mTorr.

Note 5: Hysteresis loops of TmIG/TbIG multilayers

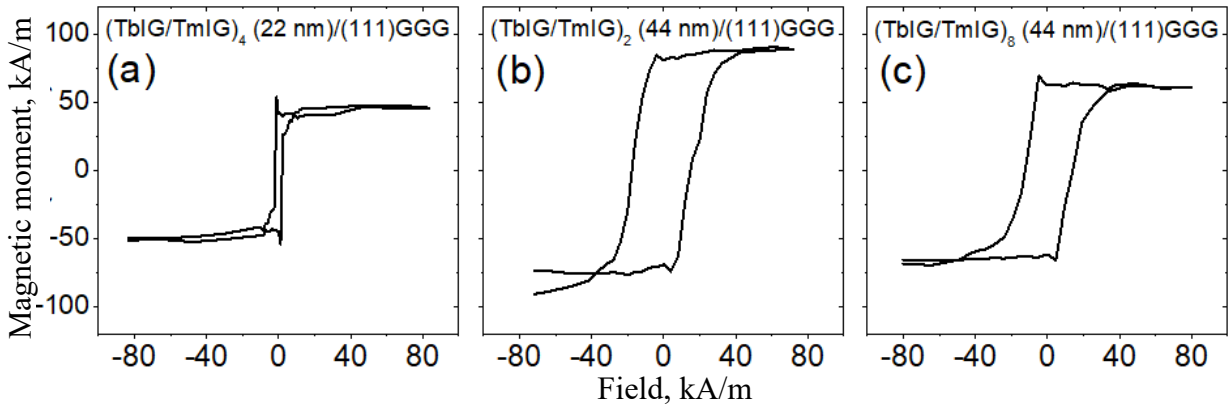

FIG. S8. Out of plane hysteresis loops of TmIG/TbIG multilayers on (111) GGG.
(a) 8 layered film of (TbIG/TmIG)/(111)GGG with overall thickness 22 nm
(b) 4 layered film with overall thickness 44 nm
(c) 16 layered film with overall thickness 44 nm.

Note 6: Ferromagnetic resonance data for BiIG – LuIG films

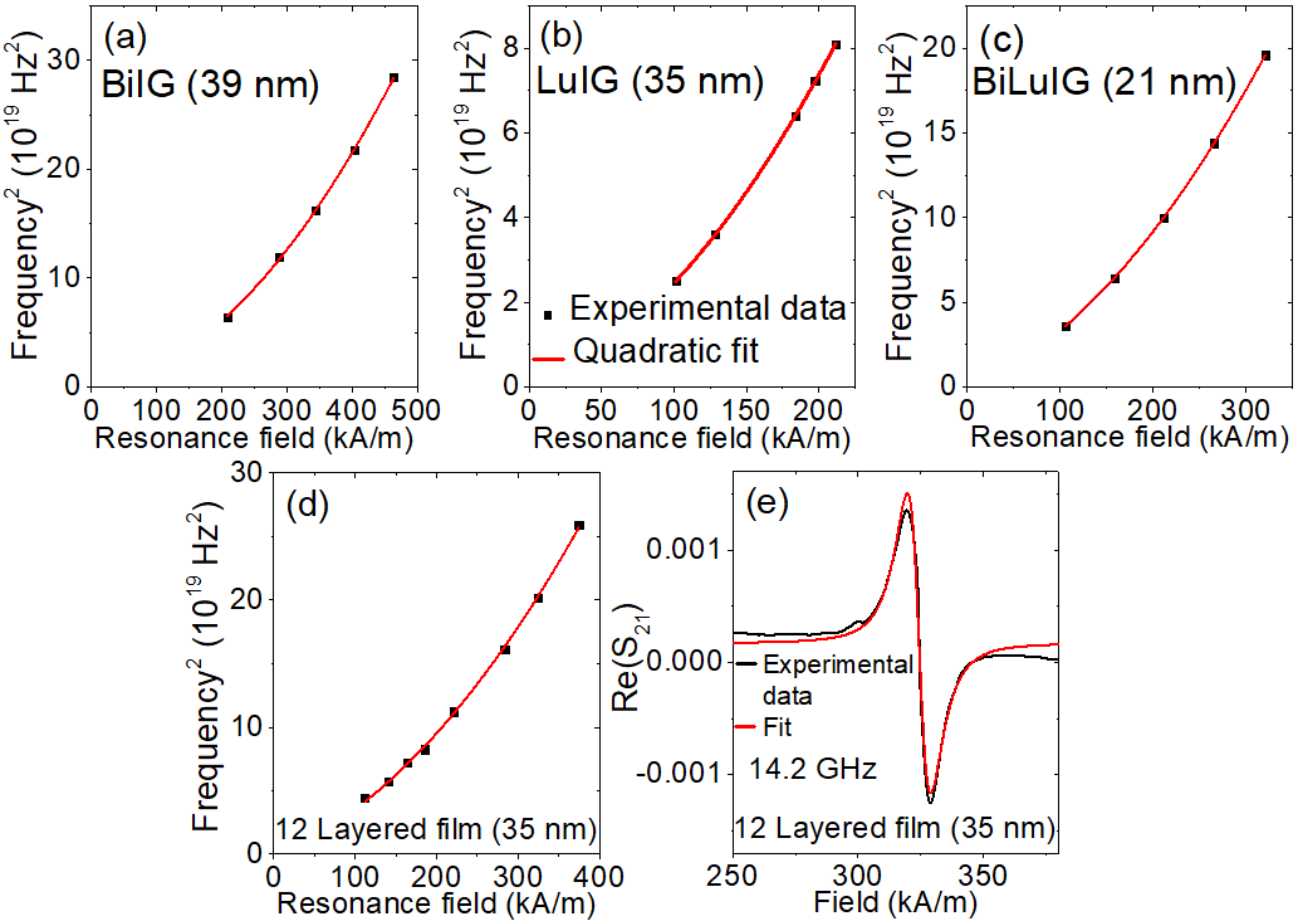

FIG. S9. Ferromagnetic resonance (FMR) data. (Frequency)^2 versus resonance field for (a) BiIG (39 nm) (b) LuIG (35 nm) (c) Solid solution BiLuIG (21 nm) (d) 12 layered (BiIG/LuIG)/(111)GGG (35 nm). All these films were deposited on GGG substrates with (111) orientation. (e) Real part of complex transmission parameter for the film in (d) at frequency of 14.2 GHz vs. in-plane field.

Note 7: Calculation of net anisotropy for TbIG and TmIG films on (111) GSGG substrate

For a TbIG film deposited on (111) GSGG substrate, the unit cell of the film undergoes a rhombohedral distortion. [245,246] Let the corner angle of the rhombohedrally distorted unit cell be β and its lattice parameter be a_R. In-plane lattice matching of the $[1\bar{1}0]$ lattice vectors gives us:

$$2\, a_R \sin\left(\frac{\beta}{2}\right) = \sqrt{2}\, a_{GSGG} \qquad (S.1)$$

Here a_{GSGG} is the lattice parameter of GSGG equal to 1.2554 nm according to the supplier (MTI), consistent with the HRXRD scan around the substrate (444) peak. The volume V_R of the rhombohedrally distorted unit cell is:

$$V_R = a_R^3 \sqrt{1 - 3\,cos^2\beta + 2\,cos^3\beta} \qquad (S.2)$$

If we consider a cartesian coordinate system with its x'-y' plane in the film and its z'-axis perpendicular to the film, the fractional change in the volume of the film unit cell due to epitaxy is given by:

$$\frac{\Delta V}{V} = e_{x'x'} \frac{2 - 4\nu}{1 - \nu} \qquad (S.3)$$

Here $e_{x'x'}$ is the strain along the in-plane x'-axis and ν = 0.29 is Poisson's ratio of the material [247], where:

$$e_{x'x'} = \frac{a_{GSGG} - a_{TbIG}^{bulk}}{a_{TbIG}^{bulk}} \qquad (S.4)$$

Using the lattice parameter of the substrate mentioned above and a_{TbIG}^{bulk} = 1.2435 nm [247] we obtain $e_{x'x'}$ = 9.57 × 10^{-3}. Using Poisson's ratio of ν = 0.29 we obtain (2 - 4ν)/(1-ν) = 1.183. Substituting these quantities in equation (3) gives us ΔV/V = 0.011. Therefore the lattice distortion leads to a change in unit cell volume given by:

$$a_R^3 \sqrt{1 - 3\,cos^2\beta + 2\,cos^3\beta} = (a_{TbIG}^{bulk})^3 \times 1.011 \qquad (S.5)$$

Solving equations (1) and (5) simultaneously we obtain β = 90.67° . Similar to the above procedure and using a_{TmIG}^{bulk} = 1.2323 nm, [247] we obtain β = 91.29° for a TmIG film deposited on a (111) GSGG substrate.

Neglecting the small magnetocrystalline anisotropy contribution and any growth-induced anisotropy, the net anisotropy for an iron garnet film deposited on a (111) oriented garnet substrate is given by [245]:

$$K_{eff} = \frac{-\mu_0}{2} M_s^2 + \frac{9}{4} c_{44}\, \lambda_{111} \left(\frac{\pi}{2} - \beta\right) \qquad (S.6)$$

Here M_s is the saturation magnetization of the film, c_{44} is the shear modulus of the film and λ_{111} is the magnetostriction constant of the film material. For a TbIG film deposited on a (111) GSGG substrate, we take M_s = 16 kA/m [247] (bulk magnetization), c_{44} = 74 GPa [247] (close to the shear modulus of several iron garnets), λ_{111} = 12 × 10^{-6} [247] (bulk value) and β = 90.67° (calculated above). Substituting these values in equation 6 gives K_{eff} = -23.5 kJ/m^3 implying an in-plane easy axis. For a TmIG film deposited on (111) GSGG, M_s = 111 kA/m [247] (assuming bulk magnetization), c_{44} = 74 GPa [247] (close to the shear modulus of several iron garnets), λ_{111} = -5.2 × 10^{-6} [247] (bulk value) and β = 91.29° (calculated above). Substituting these values in equation 6 gives K_{eff} = 11.8 kJ/m^3 implying an out-of-plane easy axis. For a solid solution 'codeposited' $Tb_{0.5}Tm_{0.5}IG$ film we assume a_{codep}^{bulk} to be the mean of the lattice parameters of TbIG and TmIG which gives a_{codep}^{bulk} = 1.2379 nm, and we assume the magnetostriction to be the mean of that of the end members giving us λ_{111}^{codep} = 3.4 × 10^{-6}. Using eq. 6 we obtain K_{eff} = -12.2 kJ/m^3. Thus, a multilayered film will show an in-plane easy axis if it behaves as an average of the end members, and a solid solution film will also show an in-plane easy axis.

Note 8: Calculation of net anisotropy for TbIG and TmIG films on (100) GGG substrate

Let us assume in-plane mutually perpendicular x and y axes and an out-of-plane z axis. Assuming in-plane lattice matching of a TbIG film with a (100) GGG substrate, axial strain along the x direction e_{xx} is given by:

$$e_{xx} = \frac{a_{GGG} - a_{TbIG}^{bulk}}{a_{TbIG}^{bulk}} \qquad (S.7)$$

Here a_{GGG} is lattice parameter of GGG equal to 1.2376 nm according to the supplier (MTI), consistent with the peak position of the substrate (444) peak. a_{TbIG}^{bulk} = 1.2435 nm [247] is the bulk lattice parameter of TbIG. Substituting these quantities in equation (7) above gives us e_{xx} = -4.745 × 10^{-3}. Using a method similar to that of Note 7, we obtain the fractional change in unit cell volume to be -5.61 × 10^{-3}. Thus, we must multiply the original cell volume by 0.9944 to get the cell volume in the distorted condition:

$$a_{GGG}^2\, c = (a_{TbIG}^{bulk})^3 \times 0.9944 \qquad (S.8)$$

Here c is the out-of-plane lattice parameter of a distorted film unit cell and a_{GGG} has been substituted for the in-plane lattice parameter of the film assuming lattice matching with GGG. Solving equation (8) gives c = 1.2484 nm. The strain along the z direction e_{zz} is given by:

$$e_{zz} = \frac{c - a_{TbIG}^{bulk}}{a_{TbIG}^{bulk}} \qquad (S.9)$$

Using equation (9), e_{zz} = 3.94 × 10^{-3}. Similarly using a_{TmIG}^{bulk} = 1.2323 nm and a procedure similar to that above we obtain e_{xx} = 4.3 × 10^{-3} and e_{zz} = -3.49 × 10^{-3} for a TmIG film deposited on a (100) GGG substrate. The net anisotropy of an iron garnet film deposited on a (100) garnet substrate, K_{eff} is given by [246]:

$$K_{eff} = \frac{3}{2}\lambda_{100}(c_{11} - c_{12})(e_{zz} - e_{xx}) - \frac{\mu_0}{2}M_s^2 \qquad (S.10)$$

Here λ_{100} is the magnetostriction constant and c_{11} and c_{12} are elastic constants of the film. Using λ_{100} = -3.3 × 10^{-6} for TbIG [247], λ_{100} = 1.4 × 10^{-6} for TmIG [247], c_{11} = 2.680 × 10^{11} J/m^3 and c_{12} = 1.106 × 10^{11} J/m^3 for both

TbIG and TmIG (close to their values for several iron garnets [247]) and the strains for the TbIG film and TmIG film on (100) GGG substrate calculated above we obtain K_{eff} = -6.9 kJ/m^3 for the TbIG film and K_{eff} = -10.3 kJ/m^3 for the TmIG film, implying in-plane easy axes for both of them. For a multilayer on (100) GGG substrate behaving as an average of the two end members we expect an in-plane easy axis. For a codeposited TbTmIG film using lattice parameter and magnetostriction constant λ_{100} which are the averages of those for TbIG and TmIG, we obtain K_{eff} = -2.5 kJ/m^3, which also implies an in-plane easy axis. Thus, both a multilayered film and a solid solution film deposited on (100) GGG substrate are expected to show an in-plane easy axis.

Chapter 8: Conclusion

In this thesis we present our findings that demonstrate suitability of iron garnets for next generation memory technologies. We demonstrate tunability of a variety of magnetic and spintronic properties including spin mixing conductance at an iron garnet|Pt interface, compensation temperature, saturation magnetization, Gilbert damping and magnetic anisotropy. We begin by growing Sc substituted TbIG (TbScIG) films on (111)GGG substrates by pulsed laser deposition (PLD). All TbScIG films grow with PMA and their compensation temperature decreased with increase in Sc content which is consistent with Sc exclusively occupying octahedral sites. A 4-fold increase in spin mixing conductance of TbScIG|Pt interface was demonstrated with increase of Sc content. We then deposit Bi substituted YIG (BiYIG) films on various garnet substrates. Anisotropy of BiYIG can be tuned using lattice misfit strain by choice of garnet substrate. BiYIG films were shown to have damping values which are orders of magnitude lower than that of rare earth iron garnets. BiYIG films deposited on GSGG show a combination of PMA and ultralow damping. BiYIG film deposited on GSGG under similar conditions has been shown to enable ultrafast domain wall motion in a past study.

In addition to tunability of properties of iron garnets we also demonstrate ability to engineer combination of properties by deposition of garnet bilayers. While BiYIG enables ultrafast domain wall motion due to its low damping, an in-plane field is required for it due to absence of DMI, an exchange interaction which stabilizes homochiral Neel domain walls which can be driven using current without application of an in-plane field. TmIG on the other hand has significant DMI enabling field free current driven domain wall motion. However, domain wall velocity is lower due to its higher damping. We demonstrated growth of an NGG|TmIG|BiYIG heterostructure which has a damping an order of magnitude lower than TmIG and significant DMI, sufficient to stabilize homochiral Neel domain walls in the material. A direction for future research can be demonstration of ultrafast field free domain wall motion in TmIG|BiYIG bilayers. This will pave the way for the development of faster and more power efficient magnetic memories.

Lastly, we deposit iron garnet superlattices and demonstrate the ability of PLD to deposit iron garnet superlattices with sub-unit-cell composition modulation. TbIG/TmIG superlattices were deposited on (111)GGG and layering was found to persist for individual layers with thickness of 0.45 nm. VSM measurements show that TbIG/TmIG multilayers deposited on (111)GGG have an out-of-plane easy axis while codeposited TbTmIG deposited on (111)GGG has an in-plane easy axis. Layering was observed using TEM and atom probe tomography (APT) images. However, development of waviness was observed for multilayers with thickness more than about 20 nm for deposition at oxygen partial pressure of 150 mTorr. Deposition at lower oxygen partial pressure (100 mTorr and 50 mTorr) has been found to result in significantly smoother films indicating multilayers without waviness. A direction for future research can be investigation of effect of PLD parameters like oxygen partial pressure, substrate temperature and laser energy on waviness of multilayers. Another direction for future research can be measurement of DMI in $(TmIG|BiYIG|Pt)_n$ stacks. DMI in TmIG|BiYIG|Pt stack originates from inversion symmetry breaking at interface and spin-orbit-coupling from TmIG and to some extent Pt. Thus, there can be additive contributions to interfacial DMI in a $(TmIG|BiYIG|Pt)_n$ stack.

Finally, we point out a challenge for development of magnetic memory based on iron garnets. Integration of iron garnets in next generation memory technology will require deposition of iron garnets on silicon. Although there has been some work on deposition of iron garnets on silicon for spintronic applications, much of the work in spintronics research and this thesis involves use of expensive garnet substrates like GGG and GSGG. More efforts are required for deposition and characterization of high quality iron garnet films on Si substrate which is the commonly used platform for electronic devices.

References

[1] *Data Centres & Networks*, https://www.iea.org/energy-system/buildings/data-centres-and-data-transmission-networks.

[2] *United States Data Center Energy Usage Report | Energy Technologies Area*, https://eta.lbl.gov/publications/united-states-data-center-energy.

[3] E. Masanet, A. Shehabi, N. Lei, S. Smith, and J. Koomey, *Recalibrating Global Data Center Energy-Use Estimates*, Science **367**, 984 (2020).

[4] D. Apalkov, B. Dieny, and J. M. Slaughter, *Magnetoresistive Random Access Memory*, Proc. IEEE **104**, 1796 (2016).

[5] S. A. Wolf, D. D. Awschalom, R. A. Buhrman, J. M. Daughton, S. von Molnár, M. L. Roukes, A. Y. Chtchelkanova, and D. M. Treger, *Spintronics: A Spin-Based Electronics Vision for the Future*, Science **294**, 1488 (2001).

[6] S. Vélez et al., *High-Speed Domain Wall Racetracks in a Magnetic Insulator*, Nat. Commun. **10**, 1 (2019).

[7] Z. Luo, A. Hrabec, T. P. Dao, G. Sala, S. Finizio, J. Feng, S. Mayr, J. Raabe, P. Gambardella, and L. J. Heyderman, *Current-Driven Magnetic Domain-Wall Logic*, Nature **579**, 214 (2020).

[8] C. O. Avci, A. Quindeau, C.-F. Pai, M. Mann, L. Caretta, A. S. Tang, M. C. Onbasli, C. A. Ross, and G. S. D. Beach, *Current-Induced Switching in a Magnetic Insulator*, Nat. Mater. **16**, 3 (2017).

[9] *Modern Magnetic Materials: Principles and Applications | Wiley*, https://www.wiley.com/en-us/Modern+Magnetic+Materials%3A+Principles+and+Applications-p-9780471155669.

[10] P. Quarterman, C. Sun, J. Garcia-Barriocanal, M. Dc, Y. Lv, S. Manipatruni, D. E. Nikonov, I. A. Young, P. M. Voyles, and J.-P. Wang, *Demonstration of Ru as the 4th Ferromagnetic Element at Room Temperature*, Nat. Commun. **9**, 1 (2018).

[11] *Introduction to Magnetic Materials, 2nd Edition | Wiley*, https://www.wiley.com/en-us/Introduction+to+Magnetic+Materials%2C+2nd+Edition-p-9780471477419.

[12] S. Blundell, *Magnetism in Condensed Matter*, 1st edition (Oxford University Press, Oxford, 2001).

[13] W. Heisenberg, *Mehrkörperproblem und Resonanz in der Quantenmechanik*, Z. Für Phys. **38**, 411 (1926).

[14] W. Pauli, *Über den Zusammenhang des Abschlusses der Elektronengruppen im Atom mit der Komplexstruktur der Spektren*, Z. Für Phys. **31**, 765 (1925).

[15] S. Shen, P. R. Ohodnicki, S. J. Kernion, and M. E. McHenry, *Two-Current Model of the Composition Dependence of Resistivity in Amorphous (Fe100−xCox)89−yZr7B4Cuy Alloys Using a Rigid-Band Assumption*, J. Appl. Phys. **112**, 103705 (2012).

[16] M. A. Ruderman and C. Kittel, *Indirect Exchange Coupling of Nuclear Magnetic Moments by Conduction Electrons*, Phys. Rev. **96**, 99 (1954).

[17] T. Kasuya, *A Theory of Metallic Ferro- and Antiferromagnetism on Zener's Model*, Prog. Theor. Phys. **16**, 45 (1956).

[18] K. Yosida, *Magnetic Properties of Cu-Mn Alloys*, Phys. Rev. **106**, 893 (1957).

[19] J. Kanamori, *Superexchange Interaction and Symmetry Properties of Electron Orbitals*, J. Phys. Chem. Solids **10**, 87 (1959).

[20] R. C. O'Handley, *Modern Magnetic Materials: Principles and Applications* (1999).

[21] *The Nobel Prize in Physics 1970*, https://www.nobelprize.org/prizes/physics/1970/summary/.

[22] P. Wadley et al., *Electrical Switching of an Antiferromagnet*, Science **351**, 587 (2016).

[23] K. Olejník et al., *Terahertz Electrical Writing Speed in an Antiferromagnetic Memory*, Sci. Adv. **4**, eaar3566 (2018).

[24] *Ultrafast and Energy-Efficient Spin–Orbit Torque Switching in Compensated Ferrimagnets | Request PDF*, https://www.researchgate.net/publication/338561806_Ultrafast_and_energy-efficient_spin-orbit_torque_switching_in_compensated_ferrimagnets.
[25] R. Pauthenet, *Magnetic Properties of the Rare Earth Garnets*, J. Appl. Phys. **30**, S290 (2009).
[26] S. Geller and M. A. Gilleo, *Structure and Ferrimagnetism of Yttrium and Rare-Earth–Iron Garnets*, Acta Crystallogr. **10**, 239 (1957).
[27] C. D. Stanciu, A. V. Kimel, F. Hansteen, A. Tsukamoto, A. Itoh, A. Kirilyuk, and Th. Rasing, *Ultrafast Spin Dynamics across Compensation Points in Ferrimagnetic GdFeCo: The Role of Angular Momentum Compensation*, Phys. Rev. B **73**, 220402 (2006).
[28] H. Chang, P. Li, W. Zhang, T. Liu, A. Hoffmann, L. Deng, and M. Wu, *Nanometer-Thick Yttrium Iron Garnet Films with Extremely Low Damping*, IEEE Magn. Lett. **5**, (2014).
[29] T. Fakhrul, B. Khurana, H. T. Nembach, J. M. Shaw, Y. Fan, G. A. Riley, L. Liu, and C. A. Ross, *Substrate-Dependent Anisotropy and Damping in Epitaxial Bismuth Yttrium Iron Garnet Thin Films*, Adv. Mater. Interfaces **10**, 2300217 (2023).
[30] C. N. Wu et al., *High-Quality Thulium Iron Garnet Films with Tunable Perpendicular Magnetic Anisotropy by off-Axis Sputtering – Correlation between Magnetic Properties and Film Strain*, Sci. Rep. **8**, 1 (2018).
[31] K. Narayanapillai, X. Qiu, Y. Wang, J. Kwon, J. Yu, L. M. Loong, W. Legrand, J. Yoon, K. Banerjee, and H. Yang, *Spin-Transfer versus Spin-Orbit Torque MRAM*, in *2016 IEEE International Nanoelectronics Conference (INEC)* (IEEE, Chengdu, China, 2016), pp. 1–2.
[32] N. S. Akulov, *On the Applications of the Law of Ferromagnetic Anisotropy for Calculation of the Properties of Polycrystalline Iron*, Z Phys **66**, 533 (1930).
[33] K. V. Vladimirsky, *On the Magnetostriction of Polycrystals*, in *Compt. Rend.(Doklady) Acad. Sci. URSS*, Vol. 41 (1943), pp. 10–13.
[34] H. B. Callen and N. Goldberg, *Magnetostriction of Polycrystalline Aggregates*, J. Appl. Phys. **36**, 976 (2004).
[35] J. C. Slonczewski, *Origin of Magnetic Anisotropy in Cobalt-Substituted Magnetite*, Phys. Rev. **110**, 1341 (1958).
[36] A. H. Eschenfelder, *Magnetic Bubble Technology* (Springer Science & Business Media, 2012).
[37] E. Rosenberg, Magnetic and Spintronic Properties of Rare-Earth Iron Garnets, Thesis, Massachusetts Institute of Technology, 2021.
[38] S. C. Abrahams and S. Geller, *Refinement of the Structure of a Grossularite Garnet*, Acta Crystallogr. **11**, 437 (1958).
[39] P. W. Anderson, *New Approach to the Theory of Superexchange Interactions*, Phys. Rev. **115**, 2 (1959).
[40] G. F. Dionne, *Magnetic Oxides* (Springer US, Boston, MA, 2009).
[41] L. Néel, *Antiferromagnetism and Ferrimagnetism*, Proc. Phys. Soc. Sect. A **65**, 869 (1952).
[42] E. E. Anderson, *Molecular Field Model and the Magnetization of YIG*, Phys. Rev. **134**, A1581 (1964).
[43] W. P. Wolf and J. H. Van Vleck, *Magnetism of Europium Garnet*, Phys. Rev. **118**, 1490 (1960).
[44] L. Caretta et al., *Fast Current-Driven Domain Walls and Small Skyrmions in a Compensated Ferrimagnet*, Nat. Nanotechnol. **13**, 1154 (2018).
[45] J. Finley and L. Liu, *Spin-Orbit-Torque Efficiency in Compensated Ferrimagnetic Cobalt-Terbium Alloys*, Phys. Rev. Appl. **6**, 054001 (2016).
[46] H. Callen, *On Growth-Induced Anisotropy in Garnet Crystals*, Mater. Res. Bull. **6**, 931 (1971).
[47] *Geller S, Williams H J, Espinosa G P & Sherwood R C. Importance of Intrasublattice Magnetic Interactions and of Substitutional Ion Type in the Behavior of Substituted Yttrium Iron Garnets. Bell Syst. Tech. J.43:565-623, 1964.*, (n.d.).
[48] S. Geller, *Magnetic Behavior of Substituted Ferrimagnetic Garnets*, J. Appl. Phys. **37**, 1408 (2004).

[49] J. Ostoréro and M. Guillot, *Magnetic Properties of Sc-Substituted Erbium Iron Garnet Single Crystals in High Magnetic Field*, J. Appl. Phys. **85**, 5214 (1999).
[50] M. A. Gilleo and S. Geller, *Substitution for Iron in Ferrimagnetic Yttrium-Iron Garnet*, J. Appl. Phys. **29**, 380 (2004).
[51] Y. Yafet and C. Kittel, *Antiferromagnetic Arrangements in Ferrites*, Phys. Rev. **87**, 290 (1952).
[52] P.-G. de Gennes, *Canted Spin Arrangements*, Phys. Rev. Lett. **3**, 209 (1959).
[53] G. F. Dionne, *Molecular Field Coefficients of Substituted Yttrium Iron Garnets*, J. Appl. Phys. **41**, 4874 (2003).
[54] P. Hansen, K. Witter, and W. Tolksdorf, *Magnetic and Magneto-Optic Properties of Lead- and Bismuth-Substituted Yttrium Iron Garnet Films*, Phys. Rev. B **27**, 6608 (1983).
[55] S. Geller, R. M. Bozorth, C. E. Miller, and D. D. Davis, *Crystal Chemical and Magnetic Studies of Garnet Systems: {YCa2}[M4+2](Fe3)O12□{Y3}[Fe2](Fe3)O12, M = Zr or Hf*, J. Phys. Chem. Solids **13**, 28 (1960).
[56] J. R. Cunningham Jr. and E. E. Anderson, *Effect of Indium Substitution in Yttrium Iron Garnet. High Permeability Garnets*, J. Appl. Phys. **32**, S388 (2009).
[57] S. Geller, H. J. Williams, G. P. Espinosa, and R. C. Sherwood, *Ferrimagnetic Garnets Containing Pentavalent Antimony*, J. Appl. Phys. **35**, 542 (2004).
[58] A. Vansteenkiste, J. Leliaert, M. Dvornik, M. Helsen, F. Garcia-Sanchez, and B. Van Waeyenberge, *The Design and Verification of MuMax3*, AIP Adv. **4**, 107133 (2014).
[59] P. M. Haney, H.-W. Lee, K.-J. Lee, A. Manchon, and M. D. Stiles, *Current Induced Torques and Interfacial Spin-Orbit Coupling: Semiclassical Modeling*, Phys. Rev. B **87**, 174411 (2013).
[60] M. D. Stiles and J. Miltat, *Spin-Transfer Torque and Dynamics*, in *Spin Dynamics in Confined Magnetic Structures III*, edited by B. Hillebrands and A. Thiaville (Springer, Berlin, Heidelberg, 2006), pp. 225–308.
[61] Y.-T. Chen, S. Takahashi, H. Nakayama, M. Althammer, S. T. B. Goennenwein, E. Saitoh, and G. E. W. Bauer, *Theory of Spin Hall Magnetoresistance (SMR) and Related Phenomena*, J. Phys. Condens. Matter **28**, 103004 (2016).
[62] L. Liu, C.-F. Pai, Y. Li, H. W. Tseng, D. C. Ralph, and R. A. Buhrman, *Spin-Torque Switching with the Giant Spin Hall Effect of Tantalum*, Science **336**, 555 (2012).
[63] L. Liu, O. J. Lee, T. J. Gudmundsen, D. C. Ralph, and R. A. Buhrman, *Current-Induced Switching of Perpendicularly Magnetized Magnetic Layers Using Spin Torque from the Spin Hall Effect*, Phys. Rev. Lett. **109**, 096602 (2012).
[64] A. Brataas, Yu. V. Nazarov, and G. E. W. Bauer, *Finite-Element Theory of Transport in Ferromagnet--Normal Metal Systems*, Phys. Rev. Lett. **84**, 2481 (2000).
[65] K.-S. Lee, S.-W. Lee, B.-C. Min, and K.-J. Lee, *Threshold Current for Switching of a Perpendicular Magnetic Layer Induced by Spin Hall Effect*, Appl. Phys. Lett. **102**, 112410 (2013).
[66] M. Collet et al., *Generation of Coherent Spin-Wave Modes in Yttrium Iron Garnet Microdiscs by Spin–Orbit Torque*, Nat. Commun. **7**, 1 (2016).
[67] P. Li et al., *Spin–Orbit Torque-Assisted Switching in Magnetic Insulator Thin Films with Perpendicular Magnetic Anisotropy*, Nat. Commun. **7**, 1 (2016).
[68] C. O. Avci, E. Rosenberg, M. Baumgartner, L. Beran, A. Quindeau, P. Gambardella, C. A. Ross, and G. S. D. Beach, *Fast Switching and Signature of Efficient Domain Wall Motion Driven by Spin-Orbit Torques in a Perpendicular Anisotropy Magnetic Insulator/Pt Bilayer*, Appl. Phys. Lett. **111**, 072406 (2017).
[69] Q. Shao et al., *Role of Dimensional Crossover on Spin-Orbit Torque Efficiency in Magnetic Insulator Thin Films*, Nat. Commun. **9**, 3612 (2018).

[70] C. O. Avci, E. Rosenberg, L. Caretta, F. Büttner, M. Mann, C. Marcus, D. Bono, C. A. Ross, and G. S. D. Beach, *Interface-Driven Chiral Magnetism and Current-Driven Domain Walls in Insulating Magnetic Garnets*, Nat. Nanotechnol. **14**, 6 (2019).
[71] L. Caretta, S.-H. Oh, T. Fakhrul, D.-K. Lee, B. H. Lee, S. K. Kim, C. A. Ross, K.-J. Lee, and G. S. D. Beach, *Relativistic Kinematics of a Magnetic Soliton*, Science **370**, 1438 (2020).
[72] I. Dzyaloshinsky, *A Thermodynamic Theory of "Weak" Ferromagnetism of Antiferromagnetics*, J. Phys. Chem. Solids **4**, 241 (1958).
[73] T. Moriya, *Anisotropic Superexchange Interaction and Weak Ferromagnetism*, Phys. Rev. **120**, 91 (1960).
[74] M. Bode, M. Heide, K. von Bergmann, P. Ferriani, S. Heinze, G. Bihlmayer, A. Kubetzka, O. Pietzsch, S. Blügel, and R. Wiesendanger, *Chiral Magnetic Order at Surfaces Driven by Inversion Asymmetry*, Nature **447**, 190 (2007).
[75] S. Mühlbauer, B. Binz, F. Jonietz, C. Pfleiderer, A. Rosch, A. Neubauer, R. Georgii, and P. Böni, *Skyrmion Lattice in a Chiral Magnet*, Science **323**, 915 (2009).
[76] X. Z. Yu, N. Kanazawa, Y. Onose, K. Kimoto, W. Z. Zhang, S. Ishiwata, Y. Matsui, and Y. Tokura, *Near Room-Temperature Formation of a Skyrmion Crystal in Thin-Films of the Helimagnet FeGe*, Nat. Mater. **10**, 106 (2011).
[77] S. Emori, U. Bauer, S.-M. Ahn, E. Martinez, and G. S. D. Beach, *Current-Driven Dynamics of Chiral Ferromagnetic Domain Walls*, Nat. Mater. **12**, 611 (2013).
[78] K.-S. Ryu, L. Thomas, S.-H. Yang, and S. Parkin, *Chiral Spin Torque at Magnetic Domain Walls*, Nat. Nanotechnol. **8**, 527 (2013).
[79] T. Fakhrul, Iron Garnet Thin Films for Integrated Photonics and Spintronics, Massachusetts Institute of Technology, n.d.
[80] A. Fert, V. Cros, and J. Sampaio, *Skyrmions on the Track*, Nat. Nanotechnol. **8**, 152 (2013).
[81] R. A. Waldo, *An Iteration Procedure to Calculate Film Compositions and Thicknesses in Electron-Probe Microanalysis*, Microbeam Anal. 310 (1988).
[82] D. Dijkkamp, T. Venkatesan, X. D. Wu, S. A. Shaheen, N. Jisrawi, Y. H. Min-Lee, W. L. McLean, and M. Croft, *Preparation of Y-Ba-Cu Oxide Superconductor Thin Films Using Pulsed Laser Evaporation from High Tc Bulk Material*, Appl. Phys. Lett. **51**, 619 (1987).
[83] A. S. Tang, Effect of Nonstoichiometry on the Magnetism and Ferroelectricity of Fe- and Co-Substituted Strontium Titanate Thin Films, Thesis, Massachusetts Institute of Technology, 2018.
[84] L. Bi, Magneto-Optical Oxide Thin Films and Integrated Nonreciprocal Photonic Devices, Thesis, Massachusetts Institute of Technology, 2011.
[85] H. T. Nembach, T. J. Silva, J. M. Shaw, M. L. Schneider, M. J. Carey, S. Maat, and J. R. Childress, *Perpendicular Ferromagnetic Resonance Measurements of Damping and Lande G-Factor in Sputtered (Co2Mn)1−xGex Thin Films*, Phys. Rev. B **84**, 054424 (2011).
[86] Y. Ding, T. Klemmer, and T. Crawford, *A Coplanar Waveguide Permeameter for Studying High-Frequency Properties of Soft Magnetic Materials*, J. Appl. Phys. **96**, 2969 (2004).
[87] I. Neudecker, G. Woltersdorf, B. Heinrich, T. Okuno, G. Gubbiotti, and C. H. Back, *Comparison of Frequency, Field, and Time Domain Ferromagnetic Resonance Methods*, J. Magn. Magn. Mater. **307**, 148 (2006).
[88] C. Gonzalez-Fuentes, R. K. Dumas, and C. García, *Systematic Errors in the Determination of the Spectroscopic G-Factor in Broadband Ferromagnetic Resonance Spectroscopy: A Proposed Solution*, J. Appl. Phys. **123**, 023901 (2018).
[89] J. M. Shaw, H. T. Nembach, and T. J. Silva, *Measurement of Orbital Asymmetry and Strain in Co90Fe10/Ni Multilayers and Alloys: Origins of Perpendicular Anisotropy*, Phys. Rev. B **87**, 054416 (2013).

[90] H. T. Nembach, J. M. Shaw, M. Weiler, E. Jué, and T. J. Silva, *Linear Relation between Heisenberg Exchange and Interfacial Dzyaloshinskii–Moriya Interaction in Metal Films*, Nat. Phys. **11**, 10 (2015).
[91] X. Ma, G. Yu, C. Tang, X. Li, C. He, J. Shi, K. L. Wang, and X. Li, *Interfacial Dzyaloshinskii-Moriya Interaction: Effect of $5d$ Band Filling and Correlation with Spin Mixing Conductance*, Phys. Rev. Lett. **120**, 157204 (2018).
[92] B. Hillebrands, *Progress in Multipass Tandem Fabry–Perot Interferometry: I. A Fully Automated, Easy to Use, Self-Aligning Spectrometer with Increased Stability and Flexibility*, Rev. Sci. Instrum. **70**, 1589 (1999).
[93] R. W. Damon and J. R. Eshbach, *Magnetostatic Modes of a Ferromagnet Slab*, J. Phys. Chem. Solids **19**, 308 (1961).
[94] C. Hahn, G. de Loubens, O. Klein, M. Viret, V. V. Naletov, and J. Ben Youssef, *Comparative Measurements of Inverse Spin Hall Effects and Magnetoresistance in YIG/Pt and YIG/Ta*, Phys. Rev. B **87**, 174417 (2013).
[95] Y.-T. Chen, S. Takahashi, H. Nakayama, M. Althammer, S. T. B. Goennenwein, E. Saitoh, and G. E. W. Bauer, *Theory of Spin Hall Magnetoresistance*, Phys. Rev. B **87**, 144411 (2013).
[96] C. Hahn, G. de Loubens, M. Viret, O. Klein, V. V. Naletov, and J. Ben Youssef, *Detection of Microwave Spin Pumping Using the Inverse Spin Hall Effect*, Phys. Rev. Lett. **111**, 217204 (2013).
[97] K. Garello, I. M. Miron, C. O. Avci, F. Freimuth, Y. Mokrousov, S. Blügel, S. Auffret, O. Boulle, G. Gaudin, and P. Gambardella, *Symmetry and Magnitude of Spin–Orbit Torques in Ferromagnetic Heterostructures*, Nat. Nanotechnol. **8**, 8 (2013).
[98] J. J. Bauer, E. R. Rosenberg, S. Kundu, K. A. Mkhoyan, P. Quarterman, A. J. Grutter, B. J. Kirby, J. A. Borchers, and C. A. Ross, *Dysprosium Iron Garnet Thin Films with Perpendicular Magnetic Anisotropy on Silicon*, Adv. Electron. Mater. **6**, 1900820 (2020).
[99] J. J. Bauer, E. R. Rosenberg, and C. A. Ross, *Perpendicular Magnetic Anisotropy and Spin Mixing Conductance in Polycrystalline Europium Iron Garnet Thin Films*, Appl. Phys. Lett. **114**, 052403 (2019).
[100] A. Quindeau et al., *Tm3Fe5O12/Pt Heterostructures with Perpendicular Magnetic Anisotropy for Spintronic Applications*, Adv. Electron. Mater. **3**, 1600376 (2017).
[101] B. F. Miao, S. Y. Huang, D. Qu, and C. L. Chien, *Inverse Spin Hall Effect in a Ferromagnetic Metal*, Phys. Rev. Lett. **111**, 066602 (2013).
[102] B. Khurana, J. J. Bauer, P. Zhang, T. Safi, C.-T. Chou, J. T. Hou, T. Fakhrul, Y. Fan, L. Liu, and C. A. Ross, *Magnetism and Spin Transport in Platinum/Scandium-Substituted Terbium Iron Garnet Heterostructures*, Phys. Rev. Mater. **5**, 084408 (2021).
[103] S. Ding et al., *Interfacial Dzyaloshinskii-Moriya Interaction and Chiral Magnetic Textures in a Ferrimagnetic Insulator*, Phys. Rev. B **100**, 100406 (2019).
[104] O. Gomonay, V. Baltz, A. Brataas, and Y. Tserkovnyak, *Antiferromagnetic Spin Textures and Dynamics*, Nat. Phys. **14**, 3 (2018).
[105] M. Shalaby, F. Vidal, M. Peccianti, R. Morandotti, F. Enderli, T. Feurer, and B. D. Patterson, *Terahertz Macrospin Dynamics in Insulating Ferrimagnets*, Phys. Rev. B **88**, 140301 (2013).
[106] Y. Kajiwara et al., *Transmission of Electrical Signals by Spin-Wave Interconversion in a Magnetic Insulator*, Nature **464**, 7286 (2010).
[107] M. B. Jungfleisch, A. V. Chumak, V. I. Vasyuchka, A. A. Serga, B. Obry, H. Schultheiss, P. A. Beck, A. D. Karenowska, E. Saitoh, and B. Hillebrands, *Temporal Evolution of Inverse Spin Hall Effect Voltage in a Magnetic Insulator-Nonmagnetic Metal Structure*, Appl. Phys. Lett. **99**, 182512 (2011).
[108] C. Hauser, T. Richter, N. Homonnay, C. Eisenschmidt, M. Qaid, H. Deniz, D. Hesse, M. Sawicki, S. G. Ebbinghaus, and G. Schmidt, *Yttrium Iron Garnet Thin Films with Very Low Damping Obtained by Recrystallization of Amorphous Material*, Sci. Rep. **6**, 1 (2016).
[109] Y. Shoji, T. Mizumoto, H. Yokoi, I.-W. Hsieh, and R. M. Osgood Jr., *Magneto-Optical Isolator with Silicon Waveguides Fabricated by Direct Bonding*, Appl. Phys. Lett. **92**, 071117 (2008).

[110] B. J. H. Stadler and T. Mizumoto, *Integrated Magneto-Optical Materials and Isolators: A Review*, IEEE Photonics J. **6**, 1 (2014).
[111] A. V. Chumak, V. I. Vasyuchka, A. A. Serga, and B. Hillebrands, *Magnon Spintronics*, Nat. Phys. **11**, 6 (2015).
[112] J. Fu et al., *Epitaxial Growth of Y3Fe5O12 Thin Films with Perpendicular Magnetic Anisotropy*, Appl. Phys. Lett. **110**, 202403 (2017).
[113] P. Sellappan, C. Tang, J. Shi, and J. E. Garay, *An Integrated Approach to Doped Thin Films with Strain-Tunable Magnetic Anisotropy: Powder Synthesis, Target Preparation and Pulsed Laser Deposition of Bi:YIG*, Mater. Res. Lett. **5**, 41 (2017).
[114] E. Lage, L. Beran, A. U. Quindeau, L. Ohnoutek, M. Kucera, R. Antos, S. R. Sani, G. F. Dionne, M. Veis, and C. A. Ross, *Temperature-Dependent Faraday Rotation and Magnetization Reorientation in Cerium-Substituted Yttrium Iron Garnet Thin Films*, APL Mater. **5**, 036104 (2017).
[115] Q.-H. Yang, H.-W. Zhang, Q.-Y. Wen, Y.-L. Liu, and J. Q. Xiao, *Tuning Magnetic Properties of Yttrium Iron Garnet Film with Oxygen Partial Pressure in Sputtering and Annealing Process*, J. Appl. Phys. **105**, 07A501 (2009).
[116] M. Isasa, A. Bedoya-Pinto, S. Vélez, F. Golmar, F. Sánchez, L. E. Hueso, J. Fontcuberta, and F. Casanova, *Spin Hall Magnetoresistance at Pt/CoFe2O4 Interfaces and Texture Effects*, Appl. Phys. Lett. **105**, 142402 (2014).
[117] P. C. Dorsey, P. Lubitz, D. B. Chrisey, and J. S. Horwitz, *CoFe2O4 Thin Films Grown on (100) MgO Substrates Using Pulsed Laser Deposition*, J. Appl. Phys. **79**, 6338 (1996).
[118] E. Popova, A. F. Franco Galeano, M. Deb, B. Warot-Fonrose, H. Kachkachi, F. Gendron, F. Ott, B. Berini, and N. Keller, *Magnetic Anisotropies in Ultrathin Bismuth Iron Garnet Films*, J. Magn. Magn. Mater. **335**, 139 (2013).
[119] L. Soumah, N. Beaulieu, L. Qassym, C. Carrétéro, E. Jacquet, R. Lebourgeois, J. Ben Youssef, P. Bortolotti, V. Cros, and A. Anane, *Ultra-Low Damping Insulating Magnetic Thin Films Get Perpendicular*, Nat. Commun. **9**, 1 (2018).
[120] E. R. Rosenberg et al., *Magnetism and Spin Transport in Rare-Earth-Rich Epitaxial Terbium and Europium Iron Garnet Films*, Phys. Rev. Mater. **2**, 094405 (2018).
[121] H. Yamahara, M. Mikami, M. Seki, and H. Tabata, *Epitaxial Strain-Induced Magnetic Anisotropy in Sm3Fe5O12 Thin Films Grown by Pulsed Laser Deposition*, J. Magn. Magn. Mater. **323**, 3143 (2011).
[122] M. Kubota, A. Tsukazaki, F. Kagawa, K. Shibuya, Y. Tokunaga, M. Kawasaki, and Y. Tokura, *Stress-Induced Perpendicular Magnetization in Epitaxial Iron Garnet Thin Films*, Appl. Phys. Express **5**, 103002 (2012).
[123] E. Popova, N. Keller, F. Gendron, M. Guyot, M.-C. Brianso, Y. Dumond, and M. Tessier, *Structure and Magnetic Properties of Yttrium–Iron–Garnet Thin Films Prepared by Laser Deposition*, J. Appl. Phys. **90**, 1422 (2001).
[124] M. B. Jungfleisch, V. Lauer, R. Neb, A. V. Chumak, and B. Hillebrands, *Improvement of the Yttrium Iron Garnet/Platinum Interface for Spin Pumping-Based Applications*, Appl. Phys. Lett. **103**, 022411 (2013).
[125] H. Yuasa, K. Tamae, and N. Onizuka, *Spin Mixing Conductance Enhancement by Increasing Magnetic Density*, AIP Adv. **7**, 055928 (2017).
[126] Z. Qiu, K. Ando, K. Uchida, Y. Kajiwara, R. Takahashi, H. Nakayama, T. An, Y. Fujikawa, and E. Saitoh, *Spin Mixing Conductance at a Well-Controlled Platinum/Yttrium Iron Garnet Interface*, Appl. Phys. Lett. **103**, 092404 (2013).
[127] Z. Qiu, D. Hou, K. Uchida, and E. Saitoh, *Influence of Interface Condition on Spin-Seebeck Effects*, J. Phys. Appl. Phys. **48**, 164013 (2015).
[128] C. O. Avci, A. Quindeau, M. Mann, C.-F. Pai, C. A. Ross, and G. S. D. Beach, *Spin Transport in As-Grown and Annealed Thulium Iron Garnet/Platinum Bilayers with Perpendicular Magnetic Anisotropy*, Phys. Rev. B **95**, 115428 (2017).

[129] S. A. Siddiqui, J. Han, J. T. Finley, C. A. Ross, and L. Liu, *Current-Induced Domain Wall Motion in a Compensated Ferrimagnet*, Phys. Rev. Lett. **121**, 057701 (2018).
[130] M. A. Gilleo and S. Geller, *Magnetic and Crystallographic Properties of Substituted Yttrium-Iron Garnet, 3Y2O3·xM2O3·(5−x)Fe2O3*, Phys. Rev. **110**, 73 (1958).
[131] S. Geller, H. J. Williams, R. C. Sherwood, and G. P. Espinosa, *Magnetic and Crystallographic Studies of Substituted Gadolinium Iron Garnets*, J. Appl. Phys. **36**, 88 (2004).
[132] W. Wang, X. Zhao, M. Lahoubi, and J. Ping Liu, *Three-Sublattice Analyses on Magnetic and Magneto-Optical Properties of Scandium Substituted Ytterbium Iron Garnet in High Magnetic Fields*, J. Magn. Magn. Mater. **374**, 333 (2015).
[133] S. Geller and M. A. Gilleo, *The Crystal Structure and Ferrimagnetism of Yttrium-Iron Garnet, Y3Fe2(FeO4)3*, J. Phys. Chem. Solids **3**, 30 (1957).
[134] K. Hirano, T. Fukamachi, M. Yoshizawa, R. Negishi, K. Hirano, and T. Kawamura, *Formation of Interference Fringes in the Bragg–(Bragg)m–Laue Mode*, Acta Crystallogr. A **65**, 253 (2009).
[135] G. van der Laan and A. I. Figueroa, *X-Ray Magnetic Circular Dichroism—A Versatile Tool to Study Magnetism*, Coord. Chem. Rev. **277–278**, 95 (2014).
[136] H. B. Vasili et al., *Direct Observation of Multivalent States and $4f\ensuremath{\rightarrow}3d$ Charge Transfer in Ce-Doped Yttrium Iron Garnet Thin Films*, Phys. Rev. B **96**, 014433 (2017).
[137] T. Fakhrul et al., *High Figure of Merit Magneto-Optical Ce- and Bi-Substituted Terbium Iron Garnet Films Integrated on Si*, Adv. Opt. Mater. **9**, 2100512 (2021).
[138] K.-H. Hellwege and A. M. Hellwege, editors , *Part A: Garnets and Perovskites*, Vol. 12a (Springer-Verlag, Berlin/Heidelberg, 1978).
[139] S. A. Manuilov, S. I. Khartsev, and A. M. Grishin, *Pulsed Laser Deposited Y3Fe5O12 Films: Nature of Magnetic Anisotropy I*, J. Appl. Phys. **106**, 123917 (2009).
[140] S. A. Manuilov and A. M. Grishin, *Pulsed Laser Deposited Y3Fe5O12 Films: Nature of Magnetic Anisotropy II*, J. Appl. Phys. **108**, 013902 (2010).
[141] E. R. Rosenberg, K. Litzius, J. M. Shaw, G. A. Riley, G. S. D. Beach, H. T. Nembach, and C. A. Ross, *Magnetic Properties and Growth-Induced Anisotropy in Yttrium Thulium Iron Garnet Thin Films*, Adv. Electron. Mater. **7**, 2100452 (2021).
[142] B. D. Cullity and S. R. Stock, *Elements of X-Ray Diffraction*, 3rd edition (Pearson, Upper Saddle River, NJ, 2001).
[143] G. F. Dionne, *Molecular-field Coefficients of Rare-earth Iron Garnets*, J. Appl. Phys. **47**, 4220 (2008).
[144] S. Tan, W. Zhang, L. Yang, J. Chen, and Z. Wang, *Intrinsic Defects in Yttrium Iron Garnet: A First-Principles Study*, J. Appl. Phys. **128**, 183904 (2020).
[145] A. S. Ahmed et al., *Spin-Hall Topological Hall Effect in Highly Tunable Pt/Ferrimagnetic-Insulator Bilayers*, Nano Lett. **19**, 5683 (2019).
[146] E. Y. Vedmedenko et al., *The 2020 Magnetism Roadmap*, J. Phys. Appl. Phys. **53**, 453001 (2020).
[147] A. A. Serga, A. V. Chumak, and B. Hillebrands, *YIG Magnonics*, J. Phys. Appl. Phys. **43**, 264002 (2010).
[148] O. Ciubotariu, A. Semisalova, K. Lenz, and M. Albrecht, *Strain-Induced Perpendicular Magnetic Anisotropy and Gilbert Damping of Tm3Fe5O12 Thin Films*, Sci. Rep. **9**, 17474 (2019).
[149] G. Schmidt, C. Hauser, P. Trempler, M. Paleschke, and E. Th. Papaioannou, *Ultra Thin Films of Yttrium Iron Garnet with Very Low Damping: A Review*, Phys. Status Solidi B **257**, 1900644 (2020).
[150] J. Ding et al., *Nanometer-Thick Yttrium Iron Garnet Films with Perpendicular Anisotropy and Low Damping*, Phys. Rev. Appl. **14**, 014017 (2020).
[151] Y. Lin, L. Jin, H. Zhang, Z. Zhong, Q. Yang, Y. Rao, and M. Li, *Bi-YIG Ferrimagnetic Insulator Nanometer Films with Large Perpendicular Magnetic Anisotropy and Narrow Ferromagnetic Resonance Linewidth*, J. Magn. Magn. Mater. **496**, 165886 (2020).
[152] H. Chen, P. De Gasperis, R. Marcelli, M. Pardavi-Horvath, R. McMichael, and P. E. Wigen, *Wide-band Linewidth Measurements in Yttrium Iron Garnet Films*, J. Appl. Phys. **67**, 5530 (1990).

[153] *Magneto-Optical Bi:YIG Films with High Figure of Merit for Nonreciprocal Photonics - Fakhrul - 2019 - Advanced Optical Materials - Wiley Online Library*, https://onlinelibrary.wiley.com/doi/full/10.1002/adom.201900056.
[154] Y. Fan, M. J. Gross, T. Fakhrul, J. Finley, J. T. Hou, S. Ngo, L. Liu, and C. A. Ross, *Coherent Magnon-Induced Domain-Wall Motion in a Magnetic Insulator Channel*, Nat. Nanotechnol. **18**, 1000 (2023).
[155] N. Adachi, V. P. Denysenkov, S. I. Khartsev, A. M. Grishin, and T. Okuda, *Epitaxial Bi3Fe5O12(001) Films Grown by Pulsed Laser Deposition and Reactive Ion Beam Sputtering Techniques*, J. Appl. Phys. **88**, 2734 (2000).
[156] L. Caretta et al., *Interfacial Dzyaloshinskii-Moriya Interaction Arising from Rare-Earth Orbital Magnetism in Insulating Magnetic Oxides*, Nat. Commun. **11**, 1090 (2020).
[157] R. Wolfe, R. C. LeCraw, S. L. Blank, and R. D. Pierce, *Growth-Induced Anisotropy in Bubble Garnet Films Containing Calcium*, AIP Conf. Proc. **34**, 172 (1976).
[158] P. Hansen, C.-P. Klages, J. Schuldt, and K. Witter, *Magnetic and Magneto-Optical Properties of Bismuth-Substituted Lutetium Iron Garnet Films*, Phys. Rev. B **31**, 5858 (1985).
[159] V. J. Fratello, S. E. G. Slusky, C. D. Brandle, and M. P. Norelli, *Growth-induced Anisotropy in Bismuth: Rare-earth Iron Garnets*, J. Appl. Phys. **60**, 2488 (1986).
[160] H. Callen, *GROWTH-INDUCED ANISOTROPY BY PREFERENTIAL SITE ORDERING IN GARNET CRYSTALS*, Appl. Phys. Lett. **18**, 311 (1971).
[161] P. Hansen, C. -P. Klages, and K. Witter, *Magnetic and Magneto-optic Properties of Praseodymium- and Bismuth-substituted Yttrium Iron Garnet Films*, J. Appl. Phys. **60**, 721 (1986).
[162] L. C. Luther, R. C. LeCraw, J. F. Dillon Jr., and R. Wolfe, *An Improved BiYIG Composition for One-micron Bubbles*, J. Appl. Phys. **53**, 2478 (1982).
[163] V. J. Fratello, S. E. G. Slusky, C. D. Brandle, and M. P. Norelli, *Effect of Diamagnetic Substitution on Growth-induced Anisotropy in (YBi)3Fe5O12*, J. Appl. Phys. **60**, 718 (1986).
[164] E. Y. Vedmedenko, A. Kubetzka, K. von Bergmann, O. Pietzsch, M. Bode, J. Kirschner, H. P. Oepen, and R. Wiesendanger, *Domain Wall Orientation in Magnetic Nanowires*, Phys. Rev. Lett. **92**, 077207 (2004).
[165] K.-W. Moon, J. W. Choi, C. Kim, J. Yoon, D.-O. Kim, K. M. Song, B. S. Chun, D. Kim, and C. Hwang, *Triangular and Sawtooth Magnetic Domains in Measuring the Dzyaloshinskii-Moriya Interaction*, Phys. Rev. Appl. **10**, 064014 (2018).
[166] V. J. Fratello, S. J. Licht, C. D. Brandle, H. M. O'Bryan, and F. A. Baiocchi, *Effect of Bismuth Doping on Thermal Expansion and Misfit Dislocations in Epitaxial Iron Garnets*, J. Cryst. Growth **142**, 93 (1994).
[167] K. Machida and Y. Asahara, *GROWTH OF Bi-SUBSTITUTED GARNET THICK EPITAXIAL FILMS FOR OPTICAL ISOLATORS*, 日本応用磁気学会誌 **11**, S1_347 (1987).
[168] D. C. Miller and R. Caruso, *Stress Relief in Magnetic Garnet Films Grown by Liquid Phase Epitaxy*, J. Cryst. Growth **27**, 274 (1974).
[169] J. H. Van Der Merwe, *Crystal Interfaces. Part II. Finite Overgrowths*, J. Appl. Phys. **34**, 123 (1963).
[170] F. Büttner et al., *Thermal Nucleation and High-Resolution Imaging of Submicrometer Magnetic Bubbles in Thin Thulium Iron Garnet Films with Perpendicular Anisotropy*, Phys. Rev. Mater. **4**, 011401 (2020).
[171] S. S. Kalarickal, P. Krivosik, M. Wu, C. E. Patton, M. L. Schneider, P. Kabos, T. J. Silva, and J. P. Nibarger, *Ferromagnetic Resonance Linewidth in Metallic Thin Films: Comparison of Measurement Methods*, J. Appl. Phys. **99**, 093909 (2006).
[172] N. Nakamura, H. Ogi, M. Hirao, T. Fukuhara, K. Shiroki, and N. Imaizumi, *Elastic Constants of Single-Crystal Rare-Earth Bismuth Iron Garnet Films*, Jpn. J. Appl. Phys. **47**, 3851 (2008).
[173] L. Liu, T. Moriyama, D. C. Ralph, and R. A. Buhrman, *Spin-Torque Ferromagnetic Resonance Induced by the Spin Hall Effect*, Phys. Rev. Lett. **106**, 036601 (2011).

[174] A. J. Berger, E. R. J. Edwards, H. T. Nembach, O. Karis, M. Weiler, and T. J. Silva, *Determination of the Spin Hall Effect and the Spin Diffusion Length of Pt from Self-Consistent Fitting of Damping Enhancement and Inverse Spin-Orbit Torque Measurements*, Phys. Rev. B **98**, 024402 (2018).
[175] T. Fakhrul, B. Khurana, B. H. Lee, S. Huang, H. T. Nembach, G. S. D. Beach, and C. A. Ross, *Damping and Interfacial Dzyaloshinskii–Moriya Interaction in Thulium Iron Garnet/Bismuth-Substituted Yttrium Iron Garnet Bilayers*, ACS Appl. Mater. Interfaces **16**, 2489 (2024).
[176] M. Stoica and C. S. Lo, *P-Type Zinc Oxide Spinels: Application to Transparent Conductors and Spintronics*, New J. Phys. **16**, 055011 (2014).
[177] P. Thakur, D. Chahar, S. Taneja, N. Bhalla, and A. Thakur, *A Review on MnZn Ferrites: Synthesis, Characterization and Applications*, Ceram. Int. **46**, 15740 (2020).
[178] H.-A. Zhou, T. Xu, H. Bai, and W. Jiang, *Efficient Spintronics with Fully Compensated Ferrimagnets*, J. Phys. Soc. Jpn. **90**, 081006 (2021).
[179] Y. Yang, T. Liu, L. Bi, and L. Deng, *Recent Advances in Development of Magnetic Garnet Thin Films for Applications in Spintronics and Photonics*, J. Alloys Compd. **860**, 158235 (2021).
[180] S. Geller, H. J. Williams, R. C. Sherwood, J. P. Remeika, and G. P. Espinosa, *Magnetic Study of the Lighter Rare-Earth Ions in the Iron Garnets*, Phys. Rev. **131**, 1080 (1963).
[181] S. Geller, J. P. Remeika, R. C. Sherwood, H. J. Williams, and G. P. Espinosa, *Magnetic Study of the Heavier Rare-Earth Iron Garnets*, Phys. Rev. **137**, A1034 (1965).
[182] R. F. Pearson, *Magnetocrystalline Anisotropy of Rare-Earth Iron Garnets*, J. Appl. Phys. **33**, 1236 (1962).
[183] S. Iida, *Magnetostriction Constants of Rare Earth Iron Garnets*, J. Phys. Soc. Jpn. **22**, 1201 (1967).
[184] D. Linzen, S. Bornmann, P. Görnert, R. Hergt, H. Pfeiffer, W. Schüppel, F. Voigt, and M. Wendt, *Growth-Induced Magnetic Anisotropy of (Sm, Ga)-Substituted YIG Films Grown on 111 Substrates*, Phys. Status Solidi A **43**, 277 (1977).
[185] N. Kumar, N. G. Kim, Y. A. Park, N. Hur, J. H. Jung, K. J. Han, and K. J. Yee, *Epitaxial Growth of Terbium Iron Garnet Thin Films with Out-of-Plane Axis of Magnetization*, Thin Solid Films **516**, 7753 (2008).
[186] L. Zhu, D. C. Ralph, and R. A. Buhrman, *Effective Spin-Mixing Conductance of Heavy-Metal--Ferromagnet Interfaces*, Phys. Rev. Lett. **123**, 057203 (2019).
[187] S. Husain et al., *Field-Free Switching of Perpendicular Magnetization in an Ultrathin Epitaxial Magnetic Insulator*, arXiv:2301.11469.
[188] Z. Xu, Q. Liu, Y. Ji, X. Li, J. Li, J. Wang, and L. Chen, *Strain-Tunable Interfacial Dzyaloshinskii–Moriya Interaction and Spin-Hall Topological Hall Effect in Pt/Tm3Fe5O12 Heterostructures*, ACS Appl. Mater. Interfaces **14**, 16791 (2022).
[189] T. Fakhrul, S. Huang, Y. Song, B. Khurana, G. S. D. Beach, and C. A. Ross, *Influence of Substrate on Interfacial Dzyaloshinskii-Moriya Interaction in Epitaxial Tm3Fe5O12 Films*, Phys. Rev. B **107**, 054421 (2023).
[190] S. Mangin, Y. Henry, D. Ravelosona, J. A. Katine, and E. E. Fullerton, *Reducing the Critical Current for Spin-Transfer Switching of Perpendicularly Magnetized Nanomagnets*, Appl. Phys. Lett. **94**, 012502 (2009).
[191] H. How, R. C. O'Handley, and F. R. Morgenthaler, *Soliton Theory for Realistic Magnetic Domain-Wall Dynamics*, Phys. Rev. B **40**, 4808 (1989).
[192] S. Crossley, A. Quindeau, A. G. Swartz, E. R. Rosenberg, L. Beran, C. O. Avci, Y. Hikita, C. A. Ross, and H. Y. Hwang, *Ferromagnetic Resonance of Perpendicularly Magnetized Tm3Fe5O12/Pt Heterostructures*, Appl. Phys. Lett. **115**, 172402 (2019).
[193] S. Vélez et al., *Current-Driven Dynamics and Ratchet Effect of Skyrmion Bubbles in a Ferrimagnetic Insulator*, Nat. Nanotechnol. **17**, 834 (2022).

[194] S. Kahl and A. M. Grishin, *Enhanced Faraday Rotation in All-Garnet Magneto-Optical Photonic Crystal*, Appl. Phys. Lett. **84**, 1438 (2004).
[195] A. Rastogi and V. N. Moorthy, *Magnetic Properties of Multilayers of Nano Thin Co,Ce-Doped and Undoped Yttrium Iron Garnet Films for Magneto-Optic Applications*, Mater. Sci. Eng. B **95**, 131 (2002).
[196] T. Fakhrul, S. Tazlaru, L. Beran, Y. Zhang, M. Veis, and C. A. Ross, *Magneto-Optical Bi:YIG Films with High Figure of Merit for Nonreciprocal Photonics*, Adv. Opt. Mater. **7**, 1900056 (2019).
[197] A. J. Lee, A. S. Ahmed, B. A. McCullian, S. Guo, M. Zhu, S. Yu, P. M. Woodward, J. Hwang, P. C. Hammel, and F. Yang, *Interfacial Rashba-Effect-Induced Anisotropy in Nonmagnetic-Material--Ferrimagnetic-Insulator Bilayers*, Phys. Rev. Lett. **124**, 257202 (2020).
[198] S. Ding, L. Baldrati, A. Ross, Z. Ren, R. Wu, S. Becker, J. Yang, G. Jakob, A. Brataas, and M. Kläui, *Identifying the Origin of the Nonmonotonic Thickness Dependence of Spin-Orbit Torque and Interfacial Dzyaloshinskii-Moriya Interaction in a Ferrimagnetic Insulator Heterostructure*, Phys. Rev. B **102**, 054425 (2020).
[199] S. Woo et al., *Observation of Room-Temperature Magnetic Skyrmions and Their Current-Driven Dynamics in Ultrathin Metallic Ferromagnets*, Nat. Mater. **15**, 501 (2016).
[200] C. Moreau-Luchaire et al., *Additive Interfacial Chiral Interaction in Multilayers for Stabilization of Small Individual Skyrmions at Room Temperature*, Nat. Nanotechnol. **11**, 444 (2016).
[201] A. Ohtomo and H. Y. Hwang, *A High-Mobility Electron Gas at the LaAlO3/SrTiO3 Heterointerface*, Nature **427**, 423 (2004).
[202] E. Bousquet, M. Dawber, N. Stucki, C. Lichtensteiger, P. Hermet, S. Gariglio, J.-M. Triscone, and P. Ghosez, *Improper Ferroelectricity in Perovskite Oxide Artificial Superlattices*, Nature **452**, 732 (2008).
[203] T. Murata, Y. Kozuka, M. Uchida, and M. Kawasaki, *Magnetic Properties of Spin Frustrated Spinel ZnFe2O4/ZnCr2O4 Superlattices*, J. Appl. Phys. **118**, 193901 (2015).
[204] J. K. Kawasaki, D. Baek, H. Paik, H. P. Nair, L. F. Kourkoutis, D. G. Schlom, and K. M. Shen, *Rutile IrO 2 / TiO 2 Superlattices: A Hyperconnected Analog to the Ruddelsden-Popper Structure*, Phys. Rev. Mater. **2**, 054206 (2018).
[205] J. D. Adam and J. H. Collins, *Microwave Magnetostatic Delay Devices Based on Epitaxial Yttrium Iron Garnet*, Proc. IEEE **64**, 794 (1976).
[206] L. Bi, J. Hu, G. F. Dionne, L. Kimerling, and C. A. Ross, *Monolithic Integration of Chalcogenide Glass/Iron Garnet Waveguides and Resonators for on-Chip Nonreciprocal Photonic Devices*, in *Integrated Optics: Devices, Materials, and Technologies XV*, Vol. 7941 (SPIE, 2011), pp. 28–37.
[207] W. Yan, Y. Yang, W. Yang, J. Qin, L. Deng, and L. Bi, *On-Chip Nonreciprocal Photonic Devices Based on Hybrid Integration of Magneto-Optical Garnet Thin Films on Silicon*, IEEE J. Sel. Top. Quantum Electron. **28**, 1 (2022).
[208] J. Lu, K. Ueda, H. Yagi, T. Yanagitani, Y. Akiyama, and A. A. Kaminskii, *Neodymium Doped Yttrium Aluminum Garnet (Y3Al5O12) Nanocrystalline Ceramics—a New Generation of Solid State Laser and Optical Materials*, J. Alloys Compd. **341**, 220 (2002).
[209] J. Lu, M. Prabhu, J. Xu, K. Ueda, H. Yagi, T. Yanagitani, and A. A. Kaminskii, *Highly Efficient 2% Nd:Yttrium Aluminum Garnet Ceramic Laser*, Appl. Phys. Lett. **77**, 3707 (2000).
[210] E. J. Cussen, *Structure and Ionic Conductivity in Lithium Garnets*, J. Mater. Chem. **20**, 5167 (2010).
[211] R. Pauthenet, *Magnetic Properties of the Rare Earth Garnets*, J. Appl. Phys. **30**, S290 (1959).
[212] S. Catalano, M. Gibert, J. Fowlie, J. Íñiguez, J.-M. Triscone, and J. Kreisel, *Rare-Earth Nickelates RNiO3: Thin Films and Heterostructures*, Rep. Prog. Phys. Phys. Soc. G. B. **81**, 046501 (2018).
[213] Z. Zhou, L. Guo, H. Yang, Q. Liu, and F. Ye, *Hydrothermal Synthesis and Magnetic Properties of Multiferroic Rare-Earth Orthoferrites*, J. Alloys Compd. 21 (2014).
[214] K. P. Belov and A. M. Kadomtseva, *MAGNETOELASTIC PROPERTIES OF RARE-EARTH ORTHOFERRITES*, Sov. Phys. Uspekhi **14**, 154 (1971).

[215] R. Vilarinho, M. C. Weber, M. Guennou, A. C. Miranda, C. Dias, P. Tavares, J. Kreisel, A. Almeida, and J. A. Moreira, *Magnetostructural Coupling in RFeO3 (R = Nd, Tb, Eu and Gd)*, Sci. Rep. **12**, 1 (2022).
[216] E. Haye, F. Capon, S. Barrat, P. Boulet, E. André, C. Carteret, and S. Bruyère, *Properties of Rare-Earth Orthoferrites Perovskite Driven by Steric Hindrance*, J. Alloys Compd. **657**, 631 (2016).
[217] S. Middey, D. Meyers, M. Kareev, E. J. Moon, B. A. Gray, X. Liu, J. W. Freeland, and J. Chakhalian, *Epitaxial Growth of (111)-Oriented LaAlO3/LaNiO3 Ultra-Thin Superlattices*, Appl. Phys. Lett. **101**, 261602 (2012).
[218] D. Hirai, J. Matsuno, and H. Takagi, *Fabrication of (111)-Oriented Ca0.5Sr0.5IrO3/SrTiO3 Superlattices—A Designed Playground for Honeycomb Physics*, APL Mater. **3**, 041508 (2015).
[219] G. Panomsuwan, O. Takai, and N. Saito, *Epitaxial Growth of (111)-Oriented BaTiO3/SrTiO3 Perovskite Superlattices on Pt(111)/Ti/Al2O3(0001) Substrates*, Appl. Phys. Lett. **103**, 112902 (2013).
[220] H. Yahiro, H. Tanaka, Y. Yamamoto, and T. Kawai, *Construction of ZnFe2O4/ZnGa2O4 Spinel-Type Artificial Superlattice by Pulsed Laser Deposition*, Jpn. J. Appl. Phys. **41**, 5153 (2002).
[221] C. Piamonteze, M. Gibert, J. Heidler, J. Dreiser, S. Rusponi, H. Brune, J.-M. Triscone, F. Nolting, and U. Staub, *Interfacial Properties of LaMnO3/LaNiO3 Superlattices Grown along (001) and (111) Orientations*, Phys. Rev. B **92**, 014426 (2015).
[222] L. Yin, W. Mi, and X. Wang, *Prediction of a Metal–Insulator Transition and a Two-Dimensional Electron Gas in Orthoferrite LaTiO3/Tetragonal BiFeO3 Heterostructures*, J. Mater. Chem. C **3**, 11066 (2015).
[223] B. Chen et al., *Spatially Controlled Octahedral Rotations and Metal–Insulator Transitions in Nickelate Superlattices*, Nano Lett. **21**, 1295 (2021).
[224] J. Hwang, J. Son, J. Y. Zhang, A. Janotti, C. G. Van de Walle, and S. Stemmer, *Structural Origins of the Properties of Rare Earth Nickelate Superlattices*, Phys. Rev. B **87**, 060101 (2013).
[225] D. Boldrin et al., *Giant Piezomagnetism in Mn3NiN*, ACS Appl. Mater. Interfaces **10**, 18863 (2018).
[226] P. Makushko et al., *Flexomagnetism and Vertically Graded Néel Temperature of Antiferromagnetic Cr2O3 Thin Films*, Nat. Commun. **13**, 1 (2022).
[227] A. F. Kabychenkov and F. V. Lisovskii, *Flexomagnetic and Flexoantiferromagnetic Effects in Centrosymmetric Antiferromagnetic Materials*, Tech. Phys. **64**, 980 (2019).
[228] M. Nur-E-Alam, M. Vasiliev, V. Kotov, and K. Alameh, *Recent Developments in Magneto-Optic Garnet-Type Thin-Film Materials Synthesis*, Procedia Eng. **76**, 61 (2014).
[229] B. M. Simion, R. Ramesh, V. G. Keramidas, G. Thomas, E. Marinero, and R. L. Pfeffer, *Magnetic Characterization of Epitaxial Y5FeeO12/Bi3Fe5O12 and Y5Fe3O12/Eu1Bi2Fe5 O12 Heterostructures Grown by Pulsed Laser Deposition*, J. Appl. Phys. **76**, 6287 (1994).
[230] M. Y. Chern, C. C. Fang, J. S. Liaw, J. G. Lin, and C. Y. Huang, *Study of Ultrathin Y3Fe5O12/Gd3Ga5O12 Superlattices*, Appl. Phys. Lett. **69**, 854 (1996).
[231] M. Y. Chern, W. S. Lee, and D. R. Liou, *Curie Temperatures of Y3Fe5O12/Gd3Fe5O12 Superlattices*, J. Magn. Magn. Mater. **170**, L243 (1997).
[232] Y. Krockenberger, J. S. Lee, D. Okuyama, H. Nakao, Y. Murakami, M. Kawasaki, and Y. Tokura, *Garnet Superlattice as a Transparent Above-Room-Temperature Polar Magnet*, Phys. Rev. B **83**, 214414 (2011).
[233] C.-H. Lee, K. S. Liang, and M. Y. Chern, *The Structures of Yttrium Iron Garnet/Gadolinium Gallium Garnet Superlattice Thin Films Studied by Synchrotron X-Ray Surface Scattering*, J. Chin. Chem. Soc. **60**, 870 (2013).
[234] K. A. Sloyan, T. C. May-Smith, M. Zervas, R. W. Eason, S. Huband, D. Walker, and P. A. Thomas, *Growth of Crystalline Garnet Mixed Films, Superlattices and Multilayers for Optical Applications via Shuttered Combinatorial Pulsed Laser Deposition*, Opt. Express **18**, 24679 (2010).

[235] D. Yi, H. Amari, P. P. Balakrishnan, C. Klewe, A. T. N'Diaye, P. Shafer, N. Browning, and Y. Suzuki, *Enhanced Interface-Driven Perpendicular Magnetic Anisotropy by Symmetry Control in Oxide Superlattices*, Phys. Rev. Appl. **15**, 024001 (2021).
[236] V. Lazenka, J. Jochum, M. Lorenz, H. Modarresi, H. Gunnlaugsson, M. Grundmann, M. Van Bael, K. Temst, and A. Vantomme, *Interface Induced Out-of-Plane Magnetic Anisotropy in Magnetoelectric BiFeO 3 -BaTiO 3 Superlattices*, Appl. Phys. Lett. **110**, 092902 (2017).
[237] T. Tepper and C. A. Ross, *Pulsed Laser Deposition and Refractive Index Measurement of Fully Substituted Bismuth Iron Garnet Films*, J. Cryst. Growth **255**, 324 (2003).
[238] T. Liu, H. Chang, Y. Sun, M. Kabatek, M. Wu, V. Vlaminck, A. Hoffmann, and L. Deng, *Ferromagnetic Resonance of Sputtered Yttrium Iron Garnet Nanometer Films*, J. Appl. Phys. **115**, (2014).
[239] L. Zhang, D. Zhang, L. Jin, B. Liu, H. Meng, X. Tang, M. Li, S. Liu, Z. Zhong, and H. Zhang, *Fabrication and Broadband Ferromagnetic Resonance Studies of Freestanding Polycrystalline Yttrium Iron Garnet Thin Films*, APL Mater. **9**, 061105 (2021).
[240] C. Kittel, *Ferromagnetic Resonance*, J. Phys. Radium **12**, 291 (1951).
[241] J. E. Hirsch, *Spin Hall Effect*, Phys. Rev. Lett. **83**, 1834 (1999).
[242] Y. Sun, Y.-Y. Song, H. Chang, M. Kabatek, M. Jantz, W. Schneider, M. Wu, H. Schultheiss, and A. Hoffmann, *Growth and Ferromagnetic Resonance Properties of Nanometer-Thick Yttrium Iron Garnet Films*, Appl. Phys. Lett. **101**, 152405 (2012).
[243] V. Sharma, S. Kumari, and B. K. Kuanr, *Rare Earth Doped M-Type Hexaferrites; Ferromagnetic Resonance and Magnetization Dynamics*, AIP Adv. **8**, 056232 (2018).
[244] D. M. Boerger, J. J. Kramer, and L. D. Partain, *Generalized Hall-Effect Measurement Geometries and Limitations of van Der Pauw-Type Hall-Effect Measurements*, J Appl Phys U. S. **52:1**, (1981).
[245] B. Khurana, J. J. Bauer, P. Zhang, T. Safi, C.-T. Chou, J. T. Hou, T. Fakhrul, Y. Fan, L. Liu, and C. A. Ross, *Magnetism and Spin Transport in Platinum/Scandium-Substituted Terbium Iron Garnet Heterostructures*, Phys. Rev. Mater. **5**, 084408 (2021).
[246] E. R. Rosenberg et al., *Magnetism and Spin Transport in Rare-Earth-Rich Epitaxial Terbium and Europium Iron Garnet Films*, Phys. Rev. Mater. **2**, 094405 (2018).
[247] K.-H. Hellwege and A. M. Hellwege, editors , *Magnetic and Other Properties of Oxides and Related Compounds · Part A: Garnets and Perovskites*, Vol. 12a (Springer-Verlag, Berlin/Heidelberg, 1978).